Development of a Body Force Model for Centrifugal Compressors

by

Anjaney Pramod Kottapalli

S.B., Massachusetts Institute of Technology (2011)

Submitted to the Department of Aeronautics and Astronautics
in partial fulfillment of the requirements for the degree of

Master of Science in Aeronautics and Astronautics

at the

MASSACHUSETTS INSTITUTE OF TECHNOLOGY

September 2013

Author .....
Department of Aeronautics and Astronautics
August 22, 2013

Certified by .....
Zoltán S. Spakovszky
Professor of Aeronautics and Astronautics
Thesis Supervisor

Accepted by .....
Eytan H. Modiano
Professor of Aeronautics and Astronautics
Chair, Graduate Program Committee

Development of a Body Force Model for Centrifugal Compressors

by

Anjaney Pramod Kottapalli

Submitted to the Department of Aeronautics and Astronautics
on August 22, 2013, in partial fulfillment of the
requirements for the degree of
Master of Science in Aeronautics and Astronautics

Abstract

This project is focused on modeling the internal flow in centrifugal compressors for the purpose of assessing the onset of rotating stall and surge. The current methods to determine centrifugal compressor stability limits are based on empirical data and often, experiments. Unsteady full wheel simulations have become feasible due to the increase in computation power but the prediction of the stability limit still remains a challenge. The presented methodology is based on the idea of body forces and a blade passage model suitable for centrifugal compressors is derived. Previous work has shown that blade passage models are capable of capturing the response to inlet flow distortions and the onset of instability in axial compressors. In this thesis, a blade passage model is developed for centrifugal compressors with the goal of capturing the three-dimensional through-flow computed by steady RANS simulations. The model consists of three main elements, a normal force model, a viscous parallel force model, and a blade metal blockage model. The work demonstrates the model's capabilities on a radial impeller with prismatic blades where the total-to-static pressure rise coefficient and stage loading coefficient are in agreement with RANS calculations within 6.75% and 5%, respectively. While the model definition is shown to be consistent with other blade passage models for axial compressors, its application to a transonic axial compressor rotor and a high-speed centrifugal compressor stage revealed numerical convergence problems. It is thought that the model derivation and definition are sound and that these issues are due to implementation errors. The methodology and related modeling process are investigated step by step for three-dimensional blade geometries and, where applicable, verified with direct numerical calculation. The model limitations and potential implementation error are discussed at length so as to guide future work required to complete the demonstration of this blade passage model for axial and centrifugal compressors with three-dimensional blade shapes.

Thesis Supervisor: Zoltán S. Spakovszky
Title: Professor of Aeronautics and Astronautics

Acknowledgments

I would like to thank Prof. Zoltán S. Spakovszky, without whom I would have never have had the opportunity to call the GTL "home". Prof. Spakovszky's acceptance of nothing less than the best has driven me to become a better engineer and a better researcher. I look forward to applying the lessons he has taught me, both professional and technical, in my future career.

Special thanks must be given to my fellow ABB Compressor Stability Project member, Jon Everitt, for his camaraderie and support. I would also like to thank Andreas Peters for the many conversations on the finer points of body force modeling. I am also deeply indebted to Max Brand, lab mate, roommate, friend, and the other half of Team Spike, for the many insightful discussions about body forces and turbomachinery in general. Will Sorensen also deserves recognition for providing a fresh perspective on many aspects of the blade passage model.

I could always count on Adam and Steve for entertaining lunch discussions about airplanes and jet engines, and Tim for conversations about quantum mechanics. I would also like to thank my officemates, George, Austin, Chris, Rachel, and Remi for making every day at the GTL enjoyable.

Many thanks go to Ravi for reminding me to laugh and enjoy life every now and then. I am also very grateful to have had Luke as a roommate and appreciate his tolerance of Max's and my many discussions about turbomachinery in our apartment. Sarah also deserves special mention for her never ending supply of food and support during the thesis writing process.

I owe an immeasurable amount of gratitude and appreciation to my parents, Mrs. Vasanta Kottapalli, and Dr. Sesi B.R. Kottapalli. They have been an endless supply of encouragement and advice through my undergraduate and graduate studies and this thesis would not have been possible without their support.

This project was sponsored by ABB Turbo Systems Ltd. I would like to thank Dr. Daniel Rusch, Dr. Rene Hunziker, Dr. Christian Roduner, Dr. Gerd Mundinger, and Arian Röber for their insightful feedback and advice.

Contents

List of Figures

List of Tables

Nomenclature

Flowfield Variables

$\mathbf{u}$	absolute flow velocity vector, [$^{\mathrm{m}}/_{\mathrm{s}}$]
$\mathbf{w}$	relative flow velocity vector, [$^{\mathrm{m}}/_{\mathrm{s}}$]
ρ	static density, [$^{\mathrm{kg}}/_{\mathrm{m}^3}$]
h	specific enthalpy, [$^{\mathrm{J}}/_{\mathrm{kg}}$]
p	static pressure, [Pa]
s	specific entropy, [$^{\mathrm{J}}/_{\mathrm{kg-K}}$]
T	static temperature, [K]

Geometry Variables and Constants

κ	blade metal angle, [rad]
λ	blade lean angle, [rad]
Ω	angular velocity of blade row, [$^{\mathrm{rad}}/_{\mathrm{s}}$]
φ	flowpath angle, [rad]
b	blade metal blockage factor, [-]
r	radial coordinate, [m]
x	axial coordinate, [m]

Blade Passage Model Variables

$f_{\mathrm{n,turn}}$ body force component normal to relative streamline, [$^{\mathrm{m}}/_{\mathrm{s}^2}$]

$f_{\mathrm{p,visc}}$ body force component parallel to relative streamline, [$^{\mathrm{m}}/_{\mathrm{s}^2}$]

$\mathbf{f}$ body force momentum source term vector, [$^{\mathrm{m}}/_{\mathrm{s}^2}$]

D deviation gradient parameter, [-]

K_p viscous parallel force coefficient, [-]

Superscripts

$()^{rel}$ quantity measured in the relative frame

Subscripts

$()_m$ meridional quantity, $\frac{\partial}{\partial \theta} = 0$

$()_t$ stagnation quantity

Chapter 1

Introduction

1.1 Background

Centrifugal compressors have a wide range of uses from land-based industrial applications in mining and manufacturing to aerospace applications such as in turboshaft engines. A major application area currently is turbocharging for land-based or automotive reciprocating engines. Future products demand reduced emission while increasing efficiency. This has led to high pressure ratio centrifugal compressor designs with stagnation pressure ratios above 5.

A centrifugal compressor used for a turbocharger application is shown in Fig. 1-1(a). Of note are the impeller blades, which are backswept with respect to the direction of rotation at the trailing edge to improve compressor stability, and the vaned diffuser blades to improve diffuser pressure recovery. A notional compressor map, presented in Fig. 1-1(b), shows the compressor stagnation pressure ratio for a given shaft speed and volumetric flow rate.

The stable operating range of a centrifugal compressor is limited by the stall/surge line at low mass flows, denoted by the left hand boundary in Fig. 1-1(b). As the required pressure ratio increases, the range of stable operation begins to shrink [17]. To the left of the stall/surge line, the compressor flow field is highly unsteady and unstable, and can lead to structural damage.

The fundamental tradeoffs in the design process are between high pressure ratio,

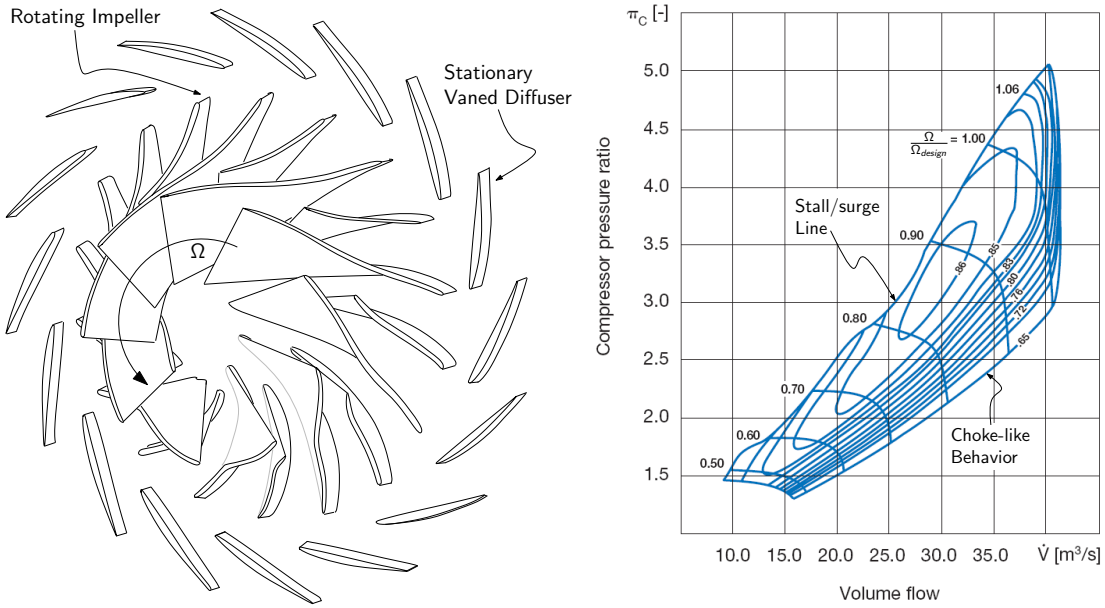

(a) Turbocharger centrifugal compressor (b) Turbocharger compressor map, from [41]

Figure 1-1: Turbocharger centrifugal compressor and compressor map.

high efficiency, and ample operating range. While the time mean performance of a compressor design can be computed using 3D single passage Reynolds-Averaged Navier-Stokes (RANS) simulations, determining the stability limit remains a challenge. As Denton [9] notes, the stability limit of the compressor is challenging to predict due to the unsteady separated flow inherent at these operating conditions. While it is possible to determine the stability limit by conducting unsteady full annulus simulations with a high mesh density, such computations are beyond the practical limits of the currently available computing power for use in the design cycle. At present, designers use empirical methods based on experimental data of similar machines or experimental test programs for each new design to determine the stability limit. A truly predictive, first principles-based, stability prediction method applicable in the design process is yet to be established.

The focus of this thesis is on modeling the three-dimensional flow in centrifugal compressors to be used in assessing the stability limit.

1.2 Compressor Instabilities

1.2.1 Types of Instabilities

There are three types of instabilities that have been observed in centrifugal compressors: surge, rotating stall, and mild surge. Surge (or "deep" surge) is a system wide instability in which the compressor is unable to maintain the pressure rise during steady operation. This leads to large-amplitude oscillations in mass flow and pressure rise of the compression system, and the compressor may experience reverse flow. Greitzer [17] notes that the frequency of the oscillations is on the order of 3-10 Hz and depends on various parameters of the overall compression system including the compressor pressure rise characteristic, the collector volume, and the duct length.

Rotating stall can be thought of as one or more local areas of reversed flow, or "stall cells," that travel around the annulus in the direction of rotation at approximately half the shaft speed. Stall cells can extend for a fraction of or the entire blade span and can range in width from just a few blade passages to nearly the entire circumference of the compressor. The phenomenon of stall cell propagation is depicted in Fig. 1-2 following Emmons et al. [12].

A blade row operating at high incidence experiences a disturbance which causes the flow along one blade to separate, i.e. stalling that particular blade. The flow separation creates aerodynamic blockage in the blade passage (Step 1 in Fig. 1-2) and diverts the upstream flow around the stalled blade (Step 2 in Fig. 1-2). This flow diversion increases the incidence on the blade adjacent to the stalled blade in the direction of the relative tangential velocity, and decreases the incidence on the blade in direction against the relative tangential velocity (Step 3 in Fig. 1-2). The blade with increased incidence will tend to stall while the flow around the blade with decreased incidence will delay the onset of stall. In this manner, the stall cell will propagate in the direction of the relative tangential velocity.

Mild surge occurs when the compressor undergoes a one-dimensional oscillation in flow and experiences rotating stall as the mass flow changes. This behavior contrasts with "deep" surge in that no distinct stall cell is observed during "deep" surge.

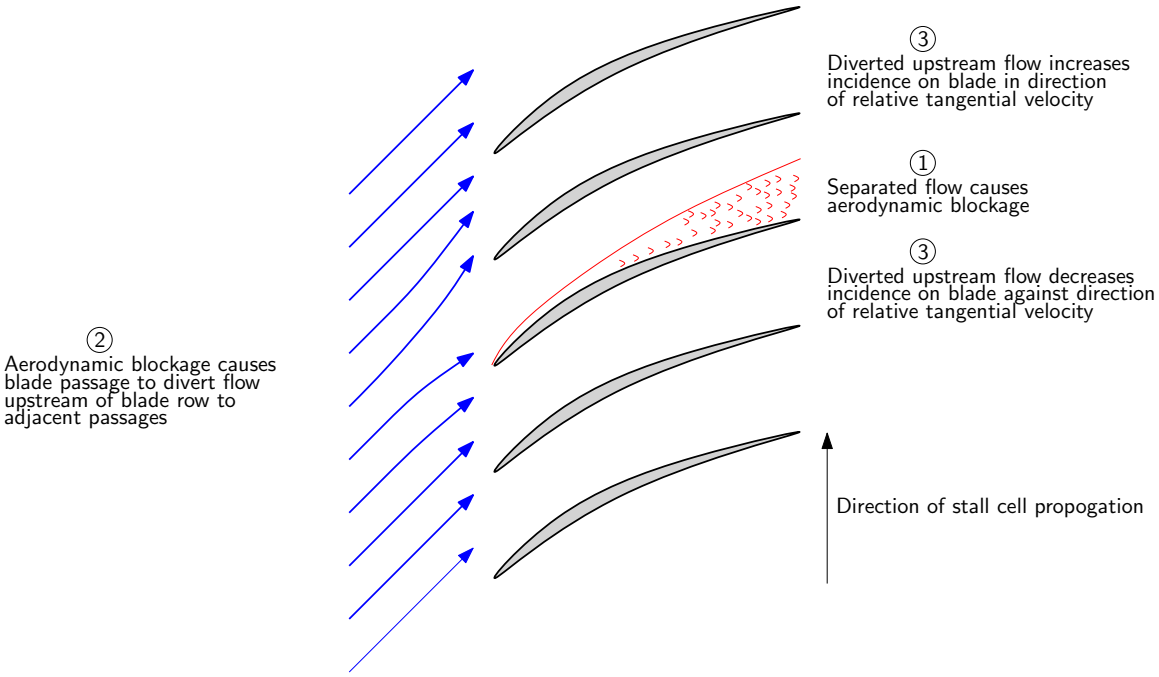

Figure 1-2: Qualitative explanation of stall cell propagation, from Emmons et al. [12].

Emmons et al. [12] showed that rotating stall may precede surge in centrifugal compressors and that mild surge can occur prior to "deep" surge.

1.2.2 Stall Inception

Stall precursors are flow features that occur prior to the onset of rotating stall. There are two paths into instability: modal-type long-wavelength and spike-type short-wavelength stall inception. Modal-type stall inception has been observed in both axial compressors and centrifugal compressors. In contrast, while spike-type stall inception has been observed in axial compressors for some time, Spakovszky and Roduner [39] only recently observed the first spike-type stall precursors in centrifugal compressors.

The difference between modal-type and spike-type stall inception is shown by the pressure traces in Figs. 1-3(a) and 1-3(b). Each figure shows a circumferential array of pressure transducers in the vaneless space of the compressor test by Spakovszky and Roduner. The difference between the operating condition for each figure is that

bleed flow was present at the hub endwall in the vaneless space in Fig. 1-3(a) while no bleed flow was present in Fig. 1-3(b). The presence of the bleed flow reduced the endwall momentum deficit in the vaneless space which destabilized the semi-vaneless space. This changed the vaned diffuser dynamic behavior and led to the growth of modal-type stall precursors.

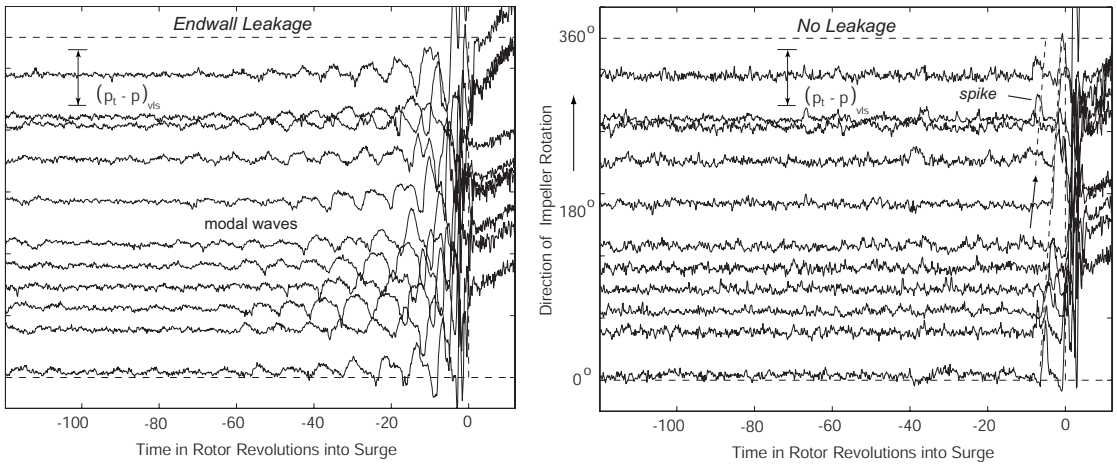

(a) Modal-type stall inception (b) Spike-type stall inception

Figure 1-3: Pressure traces from the vaneless space showing long and short-wavelength stall precursors, from Spakovszky and Roduner [39].

Modal-Type Stall Inception

Modal-type stall inception is characterized by a circumferential perturbation with a wavelength much greater than a blade pitch. These long-wavelength stall precursors are the natural oscillations of the flow field and occur at least 10-20 rotor revolutions before the formation of a mature stall cell.

Moore and Greitzer [28] developed a low-order analytical model for modal-type stall inception in axial compressors which was experimentally confirmed by McDougall et al. [26]. Long-wavelength stall precursors were found to occur and grow when the damping of the background flow conditions becomes negative. Spakovszky [38] extended Moore and Greitzer's model by resolving the dynamics of individual components of the compressor system such as individual blade rows, inter-blade-row gaps,

and intermediate ducts. This extended model was used to predict the stability of the NASA CC3 centrifugal compressor and led to the discovery of backward traveling modal-type stall precursors. These four-lobed backward traveling waves were found to occur due to coupling between upstream pressure disturbances transmitted through the impeller and pressure disturbances reflected from the vaned diffuser due to the shed vorticity from the impeller. It was also found that the energy of the modal waves was strongest in the vaneless space, consistent with the location of the wave coupling noted above.

Spike-Type Stall Precursors

Spike-type stall precursors are characterized by a short wavelength perturbation that is limited to a few blade passages in width and occurs only 5-10 rotor revolutions prior to the emergence of a mature rotating stall cell. The short-wavelength stall precursors are three dimensional in nature and of blade passage scale. This is in contrast to modal-type stall precursors which are periodic in the circumferential direction.

While previous work suggested that the tip clearance flow was necessary for the formation of short-wavelength stall precursors [42], spike-type stall inception has been observed in applications with no tip gap. Specifically, Spakovszky and Roduner [39] observed spikes in the vaned diffuser of a high pressure ratio centrifugal compressor and hypothesized that blade tip leakage flow is not necessary for the formations of spikes. Based on this hypothesis, Brand and Kottapalli [3] demonstrated the occurrence of spikes in a low pressure ratio axial compressor with shrouded blade tips inhibiting blade tip leakage flow. Further work by Hill [20] and Everitt and Spakovszky [13] used unsteady forced response simulations of an isolated diffuser to show that spike-type stall inception in the vaneless space is caused by flow separation at the diffuser leading edge. The leading edge shed vorticity is convected back into the vaneless space by radially reversed flow near the shroud endwall. The convected vorticity triggers neighboring blades to shed their leading edge vorticity, causing spike-type stall inception and leading to rotating stall. The idea that short-wavelength stall precursors are due to the shed vorticity of individual blades is further supported by

Pullan et al. [33] who showed that for simulations of a 2D cascade, a 3D blade row with no tip gap, and a 3D blade row with nonzero tip gap, spike-type stall inception is the result of the shed vorticity from the blade leading edge. Simulations of a 3D blade row with nonzero tip clearance were also verified against experimental data. The shed vorticity forms a vortex tube between the blade suction side and the shroud casing. The vortex tube "end"[1] near the blade suction side moves downstream with the mean flow while the vortex tube "end" next to the shroud casing moves circumferentially towards the the pressure side of the neighboring blade, triggering another separation which continues the instability. Blade tip leakage flow is not necessary to cause spike-type stall inception but can increase the blade incidence at the tip through blockage.

1.2.3 Criteria for Instability Onset

While there has been much work on formulating criteria for compression system level instabilities and the stall inception process in axial compressors, centrifugal compressors still lack a generalized theory or criterion. The criteria developed for system level instabilities and axial compressors are reviewed, followed by a discussion of the current progress towards a criterion in centrifugal compressors.

Criterion for Compression System Instabilities

Greitzer [15] formulated a criterion for which type of instability would occur based on compression system level parameters. This criterion was developed by linearizing the behavior of the different components of the compression system. A second order differential equation that governs the eigenvalues of the pressure and velocity perturbations of the compression system was derived and solved analytically. It was found that the type of instability encountered at the stability limit, surge or rotating stall depends on the following parameter,

$$B = \frac{\Omega r_m}{2a}\sqrt{\frac{V}{AL}}\,, \tag{1.1}$$

[1]The vortex tube cannot end on solid stationary surfaces. The vortex lines forming the vortex tube become tangential to the casing surface as noted by Pullan et al. [33].

where Ω is the rotor shaft speed, r_m is the mean radius of the compressor, a is the speed of sound, V is the collector volume, A is the cross sectional area of the ducting, and L is the length of the duct. Expansion of the B-parameter in Eq. 1.1 based on the Helmholtz frequency of the compression system, $\omega = a\sqrt{\frac{A}{VL}}$, gives,

$$B = \frac{\rho\Omega^2 r_m^2/2}{\rho\Omega r_m \omega L}\,. \tag{1.2}$$

This shows that B represents the ratio of two forces: pressure forces in the duct[2] and inertial forces due to flow oscillations. At values of B greater than $\approx$1.0, the pressure forces are dominant and system level surge occurs. When B is small, the inertial forces dominate and rotating stall occurs. Experimental work [16] confirmed that compression systems with a value of B above $\approx$0.8 experienced surge while compression systems with lower values of B experienced rotating stall.

The dependency of dynamic instability on B is associated with the slope of the compressor characteristic. A perturbation energy analysis [17] shows that the negatively sloped portion of the characteristic has a positive damping effect on mass flow perturbations while the positively sloped side of the characteristic exhibits negative damping and leads to instabilities.

Criterion for Axial Compressor Stall Inception

Camp and Day [4] noted that an axial compressor stage will undergo modal-type stall inception prior to the onset of rotating stall when the slope of the total-to-static pressure rise coefficient, ψ_{ts}, with respect to flow coefficient, ϕ, is near zero or slightly positive. This observation is consistent with the perturbation analysis presented by Stenning [40], which predicts the onset of rotating stall will occur when $\frac{\partial \psi_{ts}}{\partial \phi}$ is zero, and the characterization of modal stall precursors as the dynamic response of the flow field by Moore and Greitzer [28].

However, Camp and Day [4] also observed that the compressor stage experiences spike-type stall inception when critical incidence of a blade row is exceeded prior to

[2]The pressure forces are proportional to $\rho\Omega^2 r_m^2$

the peak of $\psi_{ts}(\phi)$. This observation is consistent with the computational work of Pullan et al. [33] describing the origins of spike-type stall inception as the blade shedding leading edge vorticity due to a large incidence.

Based on the above experimental observations and analysis, the suggested criterion for axial compressor instability onset is that modal-type stall inception will occur when $\frac{\partial \psi_{ts}}{\partial \phi}$ is near zero, which corresponds to neutral stability with zero damping, and that spike-type stall inception will occur when the blade experiences critical incidence, causing leading edge vorticity to be shed[3].

Discussion of Criteria for Centrifugal Compressor Stability

Greitzer [17] introduced a stability slope parameter based on the pressure ratios across components through the centrifugal compressor as,

$$\left(\frac{1}{PR_{ov}}\right)\frac{\partial PR_{ov}}{\partial \phi} = \sum\left(\frac{1}{PR_i}\frac{\partial PR_i}{\partial \phi}\right), \tag{1.3}$$

where $\frac{\partial PR_{ov}}{\partial \phi}$ is the overall compressor stability parameter, ϕ is the flow coefficient, and PR_i is the total-to-static pressure ratio for the impeller and the static-to-static pressure ratio for the vaneless space, semi-vaneless space, and diffuser channel. Similar to the stability analysis of the overall compression system, the sign of $\left(\frac{1}{PR_{ov}}\right)\frac{\partial PR_{ov}}{\partial \dot{m}}$ dictates the stability of the compressor; the compressor is stable if $\left(\frac{1}{PR_{ov}}\right)\frac{\partial PR_{ov}}{\partial \dot{m}}$ is negative and unstable if positive. The (de)stabilizing effect of the subcomponents is similarly governed by the sign of $\frac{\partial PR_i}{\partial \phi}$.

Hunziker and Gyarmathy [21] used the slopes of static pressure coefficient characteristics, rather than the slopes of the static pressure ratio characteristics as above, to identify the diffuser channel as a generally destabilizing subcomponent and noted that the change in the sign of the slope of the semi-vaneless space static pressure rise coefficient governed the path to centrifugal compressor instability. The static-to-static

[3]It is possible for both types of stall precursors to occur at the same time. Which type of stall inception triggers rotating stall depends on the compressor design and operating point.

pressure rise coefficient is defined by,

$$Dp_i = \frac{\Delta p_i}{\frac{1}{2}\rho_0 \left(\Omega r_2\right)^2}\,, \tag{1.4}$$

where Δp_i is the static pressure rise through the component i, ρ_0 is the inlet density, Ω is the impeller shaft speed, and r_2 is the impeller exit radius. The static pressure rise coefficient can be rewritten as a function of PR_i as,

$$Dp_i = \frac{p_{u,i}}{\frac{1}{2}\rho_0 \left(\Omega r_2\right)^2}\left(PR_i - 1\right)\,, \tag{1.5}$$

where $p_{u,i}$ is the static pressure upstream of component i. Inspection of Eq. 1.5 indicates that the sign of $\frac{\partial Dp_i}{\partial \phi}$ is generally the same sign as $\frac{\partial PR_i}{\partial \phi}$, indicating that both metrics capture the same individual subcomponent behavior. In line with this criterion, the work by Spakovszky and Roduner [39] also showed these stall precursors occurred when the slope of the semi-vaneless space was decreased to zero when hub endwall flow was extracted.

1.2.4 Models for Compressor Stability

Cumpsty [6] notes that, "[a]t present the most reliable method of estimating the stall or surge point is to use information from tests of similar machines". Empirical correlations are based on previous experimental test programs and provide little insight into the flow features that cause instability.

Some designers use the lowest mass flow at which steady CFD simulations converge as the stability limit [9]. This approach generally estimates the onset of instability at higher mass flows and lower pressure ratios than found experimentally due to limitations in turbulence modeling. While using empirical data or 3D RANS CFD is not feasible within the design process due to time constraints or predictive capability, respectively, a number of low order and low computational cost models for compressor stability have been developed. These models provide insight into the flow features that cause instability. A subset of these models is presented in Tab. 1.1, from [30].

Table 1.1: Subset of compressor stability models, from Paduano [30].

Dimension	Model	Compressible/ Multistage	Nonlinear/ Distortion, Spikes
1D	Multistage Surge ([15])	✓	1D effects
2D	Moore-Greitzer Based ([28] and [37])	Multistage [37]	✓, no spikes
3D	Body Force Models ([14])	✓	✓

The one dimensional model developed by Greitzer [15], uses the linearized behavior of the components of the compression system to determine if the compression system will enter surge or rotating stall. This model treats the compressor as a semi-actuator disk characterized by its pressure rise coefficient characteristic.

The Moore-Greitzer [28] based models use a linearized form of the unsteady governing equations to derive a system of partial differential equations that determine the growth of flow perturbations in the axial and circumferential directions in a compression system. The unsteady pressure difference across the compressor is computed "by modeling the blade passage as a parallel duct at a mean stagger angle" [24] and introducing first-order time lag components to account for losses. The behavior of components, such as ducts and throttles, are computed by linearizing the two dimensional governing equations.

Spakovszky [37] extended the Moore-Greitzer framework to include the effects of radial impellers and diffusers and introduced modular transmission matrices. These extensions allowed for the modeling of centrifugal compressors and multistage machines, respectively, without having to rewrite the system of equations each time a new component is added. The extended model is still two-dimensional since the growth of perturbations is computed in either the axial and circumferential directions or the radial and circumferential directions.

While the analytical models described above are suitable for capturing surge and modal-type stall inception, the two dimensional nature of the models cannot capture three dimensional spike-type stall inception. Gong [14] addressed this need by using a body force field that models the response of the flow field to perturbations in the

axial, radial, and circumferential directions. This model was capable of qualitatively showing the compressor response to inlet flow distortions and modal-type and spike-type stall inception.

1.3 Thesis Goals and Objectives

Building on previous work on body force modeling of axial compressors, the main objective of this thesis is to develop a blade passage model suitable for estimating the three-dimensional through-flow in centrifugal compressors. If successful, the established model paves the way for assessing the compressor dynamic behavior and instability limit. The goal is to demonstrate the model's capability to estimate the key flow features and performance of various turbomachinery geometries, ranging from axial compressor blade rows to centrifugal compressor impellers and vaned diffusers.

1.4 Thesis Outline

The modeling of a compressor blade with body force fields and methods of assessing stability using body force-based methods are presented in Chap. 2. Chapter 3 discusses the desired attributes, derivation, and implementation of the developed blade passage body force model. Chapter 4 details the extraction of a body force field from single passage RANS simulations of an axial compressor rotor and validation of the extraction process on the same rotor is given in Chap. 5. Chapter 6 presents validation of the blade passage model derived in Chap. 3 on a prismatic radial impeller. Chapter 7 discusses the challenges associated with implementing the blade passage body force model for compressors with three dimensional blade geometries and Chap. 8 summarizes the current work and provides suggestions for future work.

Chapter 2

Body Force-Based Methods to Assess Compressor Stability

The framework of body force-based methods for stability assessment consists of reconstructing the axisymmetric mean flow field using a body force field and then modeling the response of the body force field to flow field perturbations. This chapter examines modeling compressor blade rows with body force fields and discusses two body force-based methods that have been used for stability analysis in the past.

2.1 Modeling a Blade Row with Body Force Fields

A body force representation of a compressor blade row reconstructs the axisymmetric influence of the blades on the flow field through source terms in the governing equations. The pressure forces, $pd\mathbf{A}$, and viscous stresses, $\underline{\underline{\tau}} \cdot d\mathbf{A}$, on one blade are averaged in the tangential direction over one blade passage to yield the body force field, $\mathbf{f}$. The body force field $\mathbf{f}$ is applied in the swept volume of the blade row, as shown in Fig. 2-1.

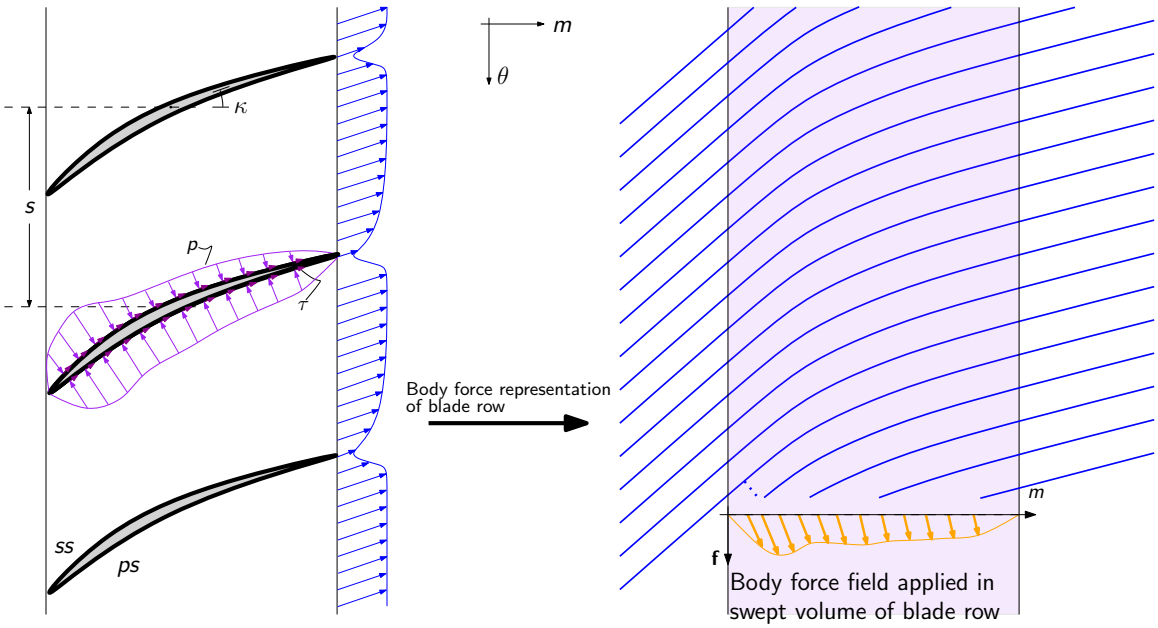

Figure 2-1: Body force field representation of blade row.

2.1.1 Aerodynamics of Axisymmetric Flow Fields with Body Forces

The entropy rise in an axisymmetric flow field with body forces is related to the body force component parallel to the relative streamline [25]. A simplified analysis is presented here to provide background for further discussion. The analysis begins with the steady axisymmetric form of the inviscid momentum equations with body forces,

$$\mathbf{u} \cdot \nabla_m \mathbf{u} = -\frac{1}{\rho} \nabla_m p + \mathbf{f} \ , \tag{2.1}$$

where ∇_m represents the meridional gradient of a quantity, $\mathbf{u}$ is the absolute velocity vector, ρ is density, and $\mathbf{f}$ is the body force source term vector.

The Gibbs Equation, $Tds = dh - \frac{1}{\rho} dp$, is substituted for the meridional gradient of static pressure to yield a relation between absolute velocity, enthalpy, and entropy,

$$\mathbf{u} \cdot \nabla_m \mathbf{u} = T \nabla_m s - \nabla_m h + \mathbf{f} \ , \tag{2.2}$$

Taking the dot product of absolute velocity and Eq. 2.2 provides an expression for the changes in stagnation enthalpy in an axisymmetric flow field with body force field,

$$\mathbf{u} \cdot \nabla_m \left(\frac{u^2}{2} \right) = T\mathbf{u} \cdot \nabla_m s - \mathbf{u} \cdot \nabla_m h + \mathbf{u} \cdot \mathbf{f} \tag{2.3}$$

$$\mathbf{u} \cdot \nabla_m h_t = T\mathbf{u} \cdot \nabla_m s + \mathbf{u} \cdot \mathbf{f} \,. \tag{2.4}$$

Equation 2.4 states that a particle convecting at a velocity $\mathbf{u}$ can perceive a change in stagnation enthalpy due to entropy changes and/or mechanical work input. The mechanical work term is expanded to account for flow fields where the modeled blade row is rotating at a rate Ω,

$$\mathbf{u} = \mathbf{w} + \Omega \times \mathbf{r} \tag{2.5}$$

$$\mathbf{u} \cdot \mathbf{f} = \mathbf{w} \cdot \mathbf{f} + \Omega r f_\theta \,. \tag{2.6}$$

The second term in Eq. 2.6 is related to changes in stagnation enthalpy by combining the tangential component of Eq. 2.1,

$$u_m \frac{\partial}{\partial m} \left(r u_\theta \right) = r f_\theta \ , \tag{2.7}$$

and the Euler turbine equation,

$$dh_t = \Omega d \left(r u_\theta \right) \ , \tag{2.8}$$

to give,

$$u_m \frac{\partial h_t}{\partial m} = \mathbf{u} \cdot \nabla_m \mathbf{h_t} = \Omega r f_\theta \,. \tag{2.9}$$

Finally, substitution of Eqs. 2.6 and 2.9 into Eq. 2.4 yields,

$$T\mathbf{u} \cdot \nabla_m s = -\mathbf{w} \cdot \mathbf{f} \,. \tag{2.10}$$

Any entropy generation in the axisymmetric flow field is due to body forces parallel to the relative streamline. The source of entropy generation in an adiabatic flow field is viscous dissipation within the blade and end wall boundary layers and due to mixing and secondary flow. The body force parallel to the relative streamline models the drag due to the boundary layers along surfaces and mixing in secondary flows in a pitchwise averaged sense. The component of the body force normal to the relative streamline is then representative of the pressure difference across the blade and is related to the lift/blade loading.

The assumption of an axisymmetric flow field implies that the compressor is comprised of "an infinite number of infinitely thin blade passages" [25]. As the body force field can respond to the local flow field, these fictitious blade passages are allowed to change in response to the flow field and might be viewed as "rubber passages."

In this thesis, the body force normal to the relative streamline is referred to as the normal force, $f_{\mathrm{n,turn}}$, and the body force parallel to the relative streamline is referred to as the viscous parallel force, $f_{\mathrm{p,visc}}$.

2.2 Body Force Field Representations

There are two main steps in the modeling of the compressor flow field via body force fields. The first step is to extract the body force field that reconstructs the axisymmetric mean flow field. The second step is to define the relationship that dictates how changes in the local body force field are related to changes in the local flow field. This step determines how the body force representation of the blade row will respond to perturbations. Table 2.1 shows the different procedures used for each step for two body force-based methods, both of which are discussed below.

The first method, a simplified blade passage model derived for axial compressors by Gong [14], uses a body force field extracted from forces on each individual blade, smeared out over a blade passage. The relationship between the body force field and the local flow field is derived through analytical expressions for blade loading, flow tangency, and blade airfoil drag.

Table 2.1: Comparison of procedures for body force field representations.

Method\Procedure → ↓	Body Force Extraction	Force Field-Flow Field Relationship
Simplified Blade Passage Model (Gong [14])	Blade Passage Forces	Analytical Expressions
Control Volume Analysis Method (Benneke [1])	Control Volume Analysis	Look Up Table

The second method, a control volume analysis method for centrifugal compressors developed by Benneke [1], uses a body force field extracted from a control volume analysis for each blade row. This is repeated for different operating conditions and the relationship between the body force field and the local flow field is governed by a look up table where the body force field components are functions of local flow field parameters.

The body force fields extracted using either procedure capture the same information and can be interchanged as inputs for the force field-flow field relationship definition.

2.2.1 Simplified Blade Passage Model for Axial Compressors

Gong [14] developed a simplified blade passage model for axial compressors to calculate the response of the flow field to inlet flow distortions and perturbations. A brief overview of the model derivation is provided here.

The simplified blade passage model decomposes the body force field into the normal force and viscous parallel force [25]. Gong [14] used deviation and loss data at the rotor exit to define the overall body force field. This method was also used by Plas [32] and Defoe and Spakovszky [8] to specify the body force field used to compute the performance of an embedded fan and the acoustics of an embedded fan, respectively.

The following interpretation of Gong's [14] simplified blade passage model is based on extensive discussions at the Gas Turbine Laboratory. The normal force on the fluid is modeled as the sum of two components, the normal force due to blade loading and

the normal force required to ensure the flow is tangent to the compressor blade,

$$f_{\text{n,turn}} = f_{\text{n,blade loading}} + f_{\text{n,flow tangency}} \ , \tag{2.11}$$

while the viscous parallel force model is similar to the drag relationship for an airfoil.

Blade Loading Model. The blade loading is computed by modeling a local section of the blade row as a staggered straight channel, shown in Fig. 2-2(a)[1]. η is the coordinate along the blade passage while ξ is the coordinate normal to the blade passage. The $(\eta - \xi)$ axes are rotated from the $(x - \theta)$ axes by the local blade metal angle, κ. Since the blade passage is modeled as a straight channel, the pressure gradient normal to the channel is negligible, $\frac{\partial p}{\partial \xi} = 0$. The force of the fluid on the blade due to blade loading is $f_{\text{on blade}}$, while the force on the fluid due to blade loading is,

$$f_{\text{n,blade loading}} = -f_{\text{on blade}} = \frac{p_{ps} - p_{ss}}{\rho h} \ , \tag{2.12}$$

where p_{ps} and p_{ss} are the static pressures on the pressure and suction sides of the blade respectively, and h is the cross channel blade pitch. Assuming a straight staggered channel with a pressure gradient in the direction of the channel, the static pressure difference across the blade is calculated by examining Fig. 2-2(a):

$$\begin{aligned} p_{ps} = p_3 &= p_{ss} + \frac{\partial p}{\partial \eta}\Delta\eta \\ p_{ps} - p_{ss} &= -\frac{\partial p}{\partial \eta} h \tan\kappa \ , \end{aligned} \tag{2.13}$$

where p_3 is the static pressure equal in value to p_{ps} since $\frac{\partial p}{\partial \xi} = 0$. $\Delta\eta$ is the distance in the blade passage direction between the locations for p_{ss} and p_3 such that $p_3 = p_{ps}$.

[1]The notation has been modified from Gong [14] to maintain consistency with the current notation.

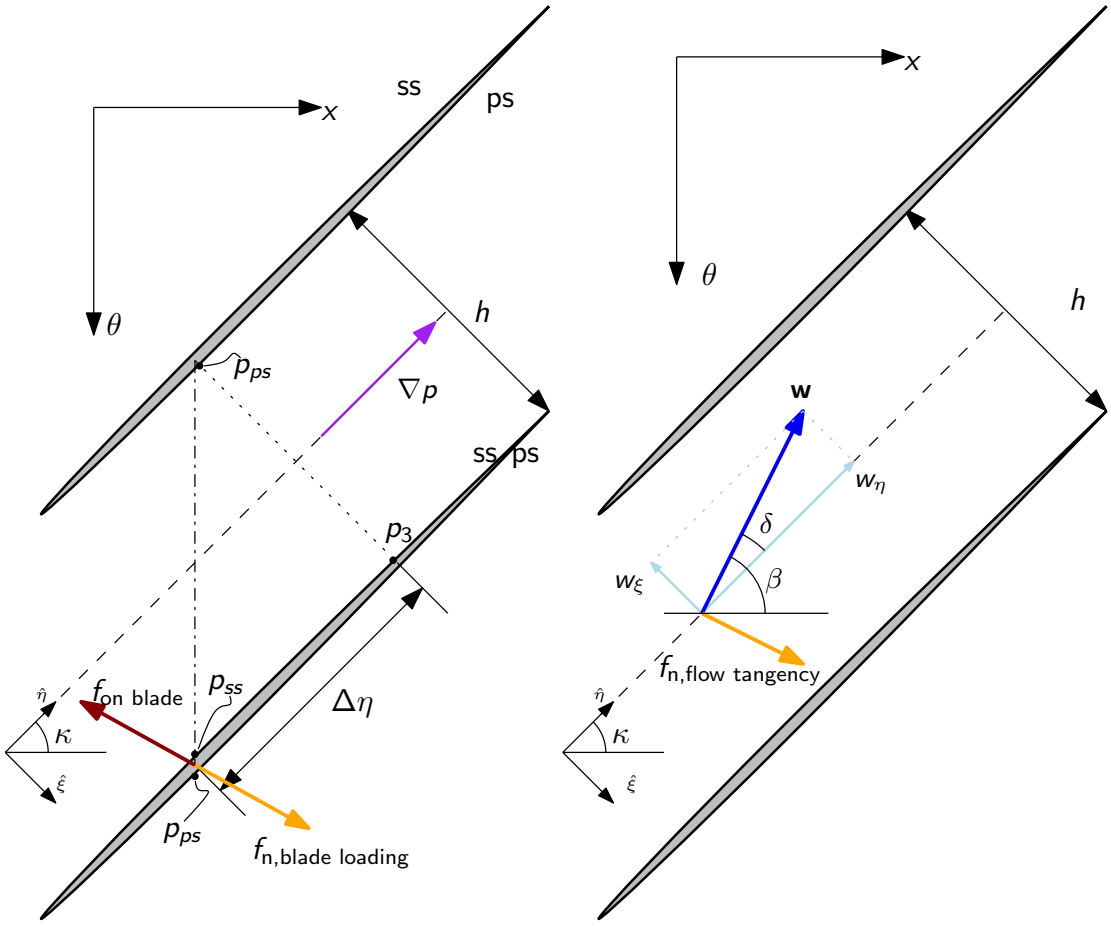

(a) Blade loading model

(b) Flow tangency model

Figure 2-2: Components of simplified blade passage model, from Gong [14].

Solving for the blade loading component of the normal force yields,

$$f_{\text{n,blade loading}} = -\frac{\partial p}{\partial \eta} \tan \kappa \,. \tag{2.14}$$

The normal force due to the blade loading must be expressed in variables that are available in an axisymmetric flow field for a consistent implementation. Gong [14] addresses this requirement by assuming that $\frac{\partial p}{\partial \eta} = \frac{\partial p}{\partial x} \cos \kappa$ which yields,

$$f_{\text{n,blade loading}} = -\frac{\partial p}{\partial x} \sin \kappa \,. \tag{2.15}$$

Flow Tangency Model. The second component of Gong's normal force model computes the normal force required to enforce flow tangency along the blade. The following analysis is based on the interpretation by Peters [31]. This concept is similar to the flow turning models implemented by Drela [11] and Chima [5]. Again, Gong assumes the blade passage can be locally modeled by a straight staggered channel, shown in Fig. 2-2(b).

The relative flow angle, β, may differ from κ by a local deviation, δ, and the relative velocity, w is decomposed into components along the blade passage, w_η, and normal to the blade passage, w_ξ. Flow tangency occurs when $w_\xi = 0$. The force required to maintain flow tangency is modeled as,

$$f_{\text{n,flow tangency}} = -K_n \frac{w_\eta w_\xi}{h} \,, \tag{2.16}$$

where K_n is an empirical constant that can be defined through experiment or computation and h is the local blade pitch, used to introduce a local length scale to obtain the appropriate units[2]. Any deviation from the blade metal angle yields a non-zero w_ξ and therefore $f_{\text{n,flow tangency}}$ turns the flow towards the blade direction so as to achieve flow tangency. The dependency on local deviation is shown by making the

[2]The blade chord is the appropriate length scale but the blade pitch is " 'preferred' ... since h can be defined locally." [14]

substitutions $w_\xi = w \sin\delta$ and $w_\eta = w \cos\delta$ as,

$$f_{\text{n,flow tangency}} = -K_n \frac{w^2}{2h} \sin 2\delta \ , \tag{2.17}$$

where δ is the local deviation angle, $\delta = \beta - \kappa$. For example, if $\delta > 0$, then $w_\xi > 0$ and the relative flow is angled more in the direction of rotation than the blade metal angle. The appropriate restoring normal force would be away from rotation in order to lower δ, as is computed by Eq. 2.17. Combining the two components of the normal force model gives,

$$f_{\text{n,turn}} = -K_n \frac{w^2}{2h} \sin 2\delta - \frac{1}{\rho} \frac{\partial p}{\partial x} \sin\kappa \tag{2.18}$$

$$= -K_n \frac{w_\eta w_\xi}{h} - \frac{1}{\rho} \frac{\partial p}{\partial x} \sin\kappa \, . \tag{2.19}$$

Viscous Parallel Force Model. The viscous parallel force is representative of the drag force along solid surfaces. Consider the equation for the drag force of an airfoil,

$$D = \frac{1}{2} \rho V^2 S C_D \ , \tag{2.20}$$

where V is the velocity relative to the airfoil, S is the reference area, and C_D is the drag coefficient. The drag force scales with the relative dynamic head and the derived model for the viscous parallel force becomes,

$$f_{\text{p,visc}} = K_p \frac{w^2}{h} \ , \tag{2.21}$$

where K_p is an empirical constant analogous to C_D and h is the local blade pitch, used to obtain the proper units.

Gong's [14] blade passage model (above) captured the response of an axial compressor to inlet flow distortions and modal-type and spike-type stall inception. Plas [32] used the same blade passage model to characterize the power savings coefficient trends of an axial fan embedded in an S-duct encountering boundary layer ingestion. The calculation was in agreement with results from a 1D control volume analysis. It

was also shown that boundary layer ingestion could provide fuel burn decreases of up to 3.8 percent.

More recently, Defoe and Spakovszky [8] used a modified version of this blade passage model to compute the effect of nonuniform flow on the generation and propagation of multiple-pure-tone noise. The body force blade passage model allowed the pressure rise and viscous losses in the fan to be modeled using Euler simulations to allow the study of noise propagation since viscous dissipation in single passage RANS simulations would mask the investigated acoustic propagation. The effect of leading edge shocks was added by introducing a discrete body force component, periodic in one blade pitch, that rotated at the same rate as the rotor [7]. Defoe and Spakovszky found that an embedded fan subject to nonuniform flow increased the noise source strength by 38 dB due to the ingested streamwise vorticity. The far field noise overall sound pressure level only increased by 3.1 dBA due to a redistribution of acoustic energy into frequencies below 11 times shaft frequency.

Peters [31] used a higher resolution version of the blade passage model to design short nacelles inlets for a low pressure ratio fan. Rather than using deviation and loss data from the midspan and tip to determine an overall K_n and K_p, the normal force and viscous parallel force at each grid point in the mesh were used to compute distributions of K_n and K_p. The higher resolution version of the simplified blade passage model was combined with a spline-based three-dimensional inlet and nacelle design tool. Peters used this approach to design a short-inlet nacelle that yielded a 0.3% increase in propulsive efficiency over an advanced long-inlet configuration.

Inconsistencies and Limitations

Streamline Curvature. The primary limitation of the simplified blade passage model is that the model does not capture the curvature of the blade passage or the relative streamline. The model derivation is based on the assumption that the blade passage is modeled by a straight channel and the cross channel pressure gradient is zero.

A notional blade passage is presented in Figs. 2-3(a) and 2-3(b) to highlight this

limitation. In the discrete blade passage shown in Fig. 2-3(a), the curving of the relative streamline through the blade passage indicates that there is a normal force on the streamline due to the presence of the blade. This also holds at the axial location indicated by the dashed line where $\kappa = 0$ and $\delta = 0$. However, the body force representation of the blade passage, shown in Fig. 2-3(b) per Eq. 2.18, yields a zero normal force on the relative streamline. This is inconsistent with the the nonzero normal force manifested in relative streamline curvature.

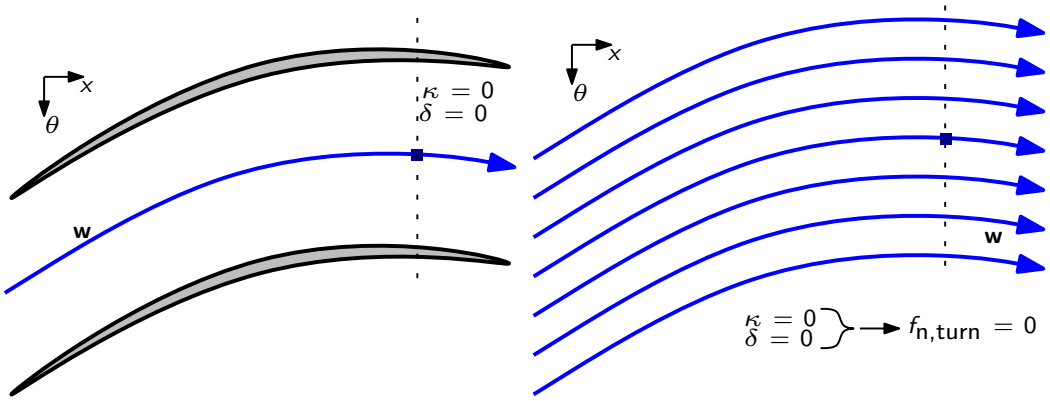

(a) Discrete blade passage (b) Body force representation

Figure 2-3: Example blade passage showing inconsistency in Eq. 2.18.

Blade Loading. Another inconsistency is the calculation of the blade loading component. Gong calculates the pressure gradient in the direction of a discrete blade passage as,

$$\frac{\partial p}{\partial \eta} = \frac{\partial p}{\partial x} \cos \kappa \,. \tag{2.22}$$

This is only valid if there is no component of the pressure gradient in the tangential direction in a discrete blade passage. It is thought that the assumption of an axisymmetric flowfield is applied incorrectly to Eq. 2.14 to obtain Eq. 2.22. A corrected

derivation is presented here. The pressure gradient in a discrete blade passage is,

$$\frac{\partial p}{\partial \eta} = \frac{\partial p}{\partial x}\cos\kappa + \frac{\partial p}{r\partial\theta}\sin\kappa \ , \tag{2.23}$$

where the blade loading on a discrete blade is the result of both the axial and tangential pressure gradients. Expressing the pressure gradient in the direction of the blade passage as a function of solely the axial pressure gradient yields,

$$\frac{\partial p}{\partial x} = \frac{\partial p}{\partial \eta}\cos\kappa \rightarrow \frac{\partial p}{\partial \eta} = \frac{\partial p}{\partial x}\sec\kappa \, . \tag{2.24}$$

With the appropriate expression for $\frac{\partial p}{\partial \eta}$ obtained, the blade loading component of the blade passage model should be,

$$f_{\text{n,blade loading}} = -\frac{1}{\rho}\frac{\partial p}{\partial x}\sin\kappa\sec^2\kappa \, . \tag{2.25}$$

Singularity in $f_{\text{n,flow tangency}}$. An additional limitation arises when computing K_n from the flow tangency component of the normal force model [31]. When $f_{\text{n,turn}}$ is extracted directly from the flow field, K_n is computed by,

$$K_n = -\left(f_{\text{n,turn}} - f_{\text{n,blade loading}}\right)\frac{2h}{w_\eta w_\xi} \, . \tag{2.26}$$

To first order w_ξ is small and can lead to spurious singularities due to the dependency of K_n on $\frac{1}{w_\xi}$. This has led to the introduction of an offset constant, C, such that the simplified blade passage model is,

$$f_{\text{n,turn}} = -K_n\frac{w_\eta\left(w_\xi + C\right)}{h} + f_{\text{n,blade loading}} \, . \tag{2.27}$$

The offset constant is of the order of w_η and avoids singular behavior. The introduction of this offset changes the response of the body force field to flow field perturbations. Considering $w_\xi/w_\eta \ll 1$, the flow tangency component of the blade passage model scales as w_η as opposed to w^2.

2.2.2 Control Volume Analysis Method for Centrifugal Compressors

Benneke [1] developed a control volume analysis method where the magnitudes of the force components are extracted through a control volume analysis. The obtained body force field responds to changes in the flow field through a look up table based on local flow field quantities. This approach was able to qualitatively capture both modal-type and spike-type stall precursors in a highly loaded centrifugal compressor with a vaned diffuser. However, the look-up table based approach revealed some challenges in quantitatively assessing and predicting the onset of instability.

Extraction of Body Force Field Through Control Volume Analysis

A series of single passage RANS simulations was first conducted to map out the speedline for the centrifugal compressor. For each operating point a control volume analysis is conducted at each axial and radial location in the single passage grid to derive the body force field [23]. An example of the constructed control volume is provided in Fig. 2-4.

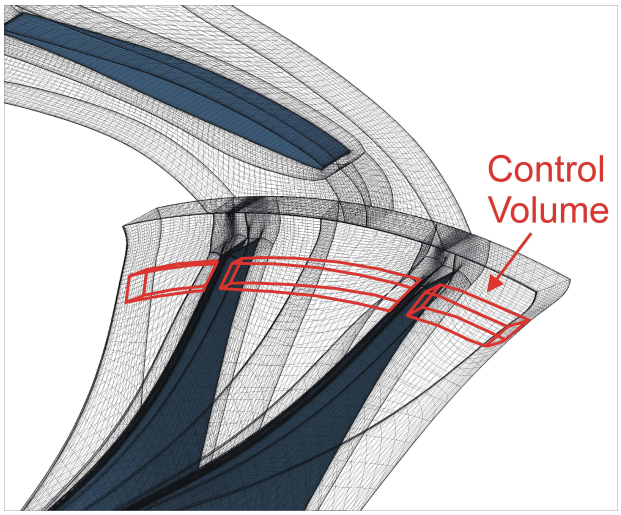

Figure 2-4: Control volume to extract body force field, from Benneke [1].

The body force components were computed from,

$$\mathbf{f} = \frac{\iint_S (\rho \mathbf{u} \cdot d\mathbf{S})\,\mathbf{u} + \iint_S p d\mathbf{S}}{\iiint_V \rho dV} \ , \tag{2.28}$$

where S is the surface of the control volume, $\mathbf{S}$ is the outward pointing normal vector to S, and V is the volume of the control volume. Equation 2.28 is derived from the control volume form of the momentum equation.

Compilation of Look Up Table for Force-Flow Field Dependency

Once the force field at each operating point was extracted, a look up table of the axial, radial, and tangential body force components, as a function of relative Mach number, M_{rel}, and relative flow angle, β, was created. The look up table maps how the body force field responds to changes in local flow field quantities.

Two sets of independent variables were examined: the first set used two independent variables, M_{rel} and β, the second set only used one independent variable, meridional Mach number, M_m, and is a simplification of the first method since $M_m = M_{rel} \cos \beta$. While two independent variables can capture the force field-flow field relationship with higher fidelity, the range of the independent variables extracted from 3D single passage RANS was insufficient to provide adequate estimation. An example of this challenge is shown in Figs. 2-5(a) and 2-5(b) which shows the normalized tangential body force extracted from a grid point near the impeller exit and near the splitter leading edge respectively. The black crosses are the actual data points extracted from the single passage RANS simulation and the color contour is the extrapolated value. For the extracted data near the impeller exit, the relative flow angle varies by 5 degrees while the relative Mach number varies by 0.5. The range of flow conditions is much smaller for the grid point near the splitter leading edge where the relative Mach number varies by 0.5 but the relative flow angle varies by only 1 degree. This difference in relative flow angle range can be explained due to slip causing large variations in relative flow angle at the impeller trailing edge and

flow tangency within the main impeller blade passage imposing a small range of flow angles near the splitter leading edge.

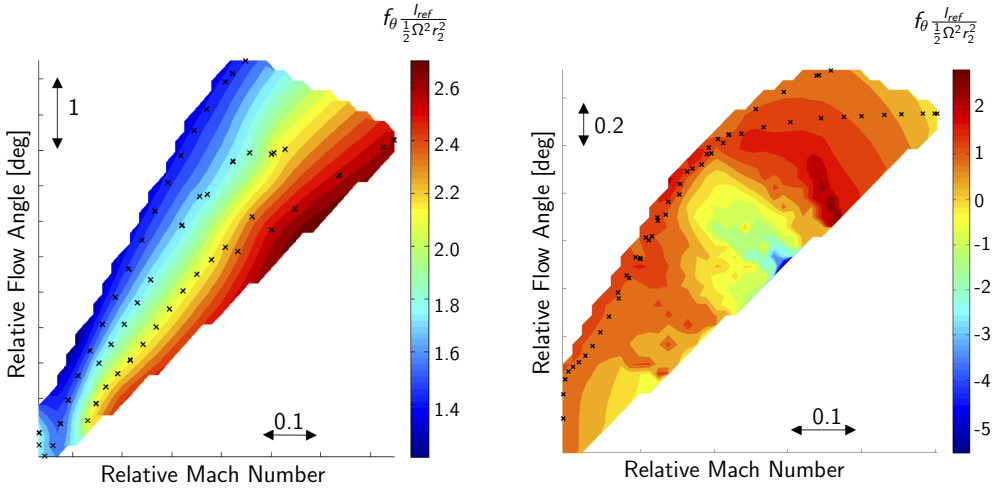

(a) $f_\theta\left(M_{rel}, \beta\right)$ near impeller exit (b) $f_\theta\left(M_{rel}, \beta\right)$ near splitter leading edge

Figure 2-5: Extracted tangential body force component for three speedlines, from Benneke [1].

Using the control volume analysis method with the meridional Mach number as the independent variable, Benneke found that body force simulations agreed with experiment in that the diffuser becomes unstable at operating points on the positively sloped side of the diffuser static pressure rise characteristic. The character of the backward traveling modal waves observed was also in agreement with a previously developed low-order analytical model and with experimental results [39]. The dynamic behavior of the compressor was then modified to simulate a different speedline by scaling the force components. The altered compressor was shown to exhibit forward traveling spike-type stall precursors when subjected to a perturbation. Examples of the backward traveling modal wave and the forward traveling spike are shown in Figs. 2-6(a) and 2-6(b) respectively.

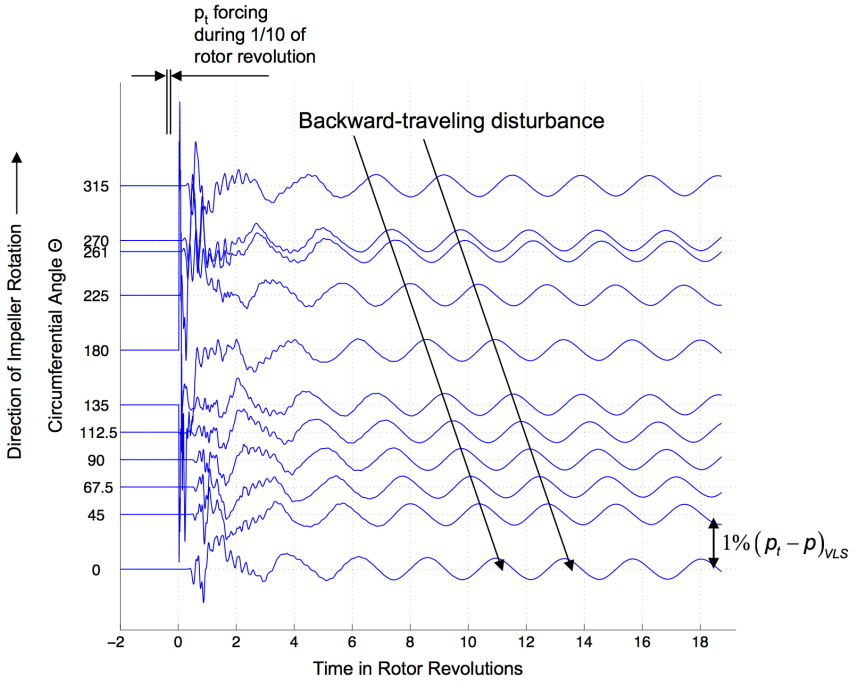

(a) Backward traveling modal stall precursors observed at 75% corrected design speed

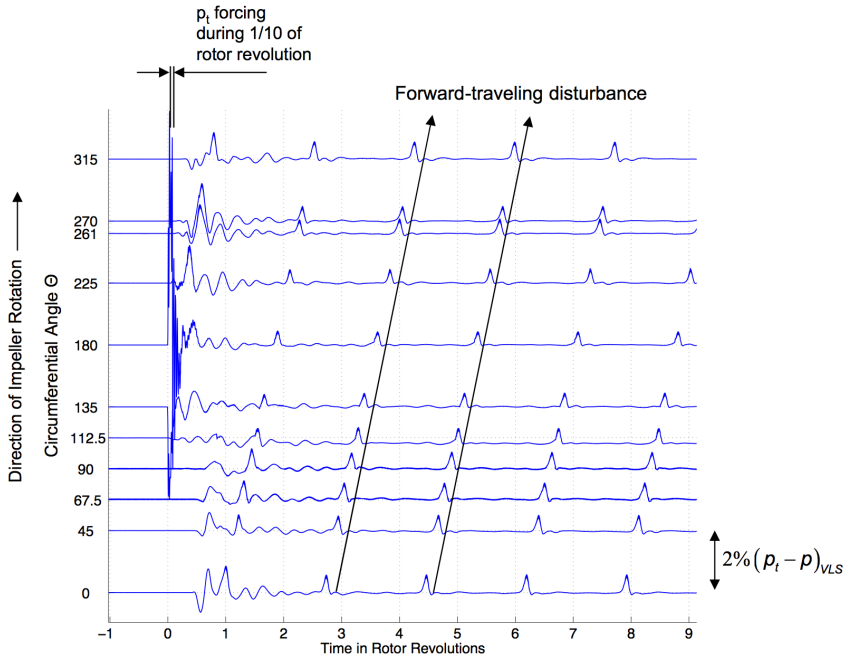

(b) Forward traveling spike-type stall precursors observed at 70% corrected design speed for altered compressor

Figure 2-6: Unsteady pressure traces in the vaneless space, from Benneke [1].

Challenges with the Look Up Table Method

Although the control volume analysis method was able to qualitatively exhibit spike-type and modal-type stall precursors, it was not able to predict the mass flow at which the instabilities occurred. Benneke [1] suggested this was due to a need for grid refinement and a more elaborate method to estimate body forces outside of the range used to develop the table. Röber [35] built on Benneke's [1] work and showed that grid refinement did not increase the accuracy of the predicted stall point.

Look Up Table Extrapolation. Simulating low flow unsteady operating points required extrapolation from the look up table which introduced artificial cut offs in the body force field. During the unsteady simulations, it was found that meridional Mach number would encounter values that were outside the meridional Mach number range used to develop the look up table, shown in Fig. 2-7(a). This issue was addressed by capping the meridional Mach number used to query the look up table which in turn capped the magnitude of applied body force component, as shown in Fig. 2-7(b).

Multivalue Situations. Use of one independent variable for the look up table led to situations where for the same meridional Mach number, two different values of the body force components are possible, as shown in Fig. 2-8(a). These multivalued situations occur when a region of flow separation creates aerodynamic blockage at low flow coefficients. The streamline shift around the blocked area, shown in Fig. 2-8(b), increases the value of M_m to one which may have been experienced at the same grid point at a higher flow coefficient.

The streamline shift leads to situations where there are two values of the body force field, one from each operating point, for the same meridional Mach number. This multivalue situation was addressed by introducing the Mach number at the compressor inlet as a secondary independent variable. However, expansion of the dimensionality of the look up table for each grid point increases memory usage, slowing down the computation.

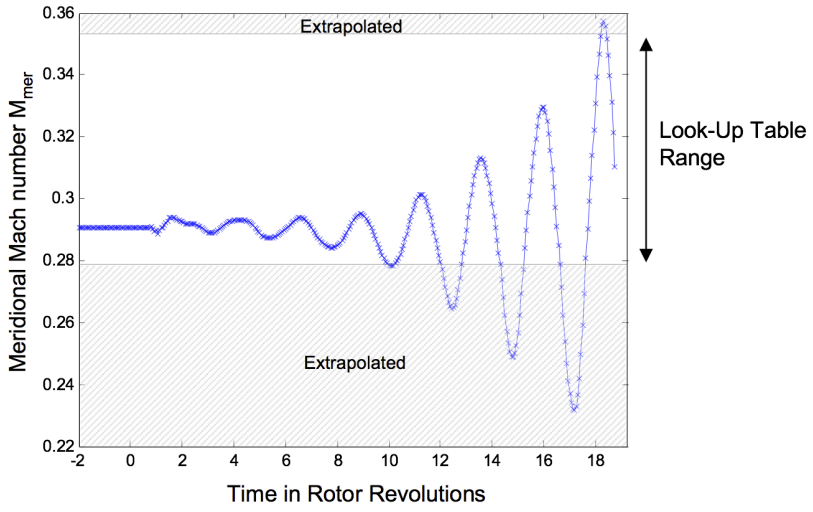

(a) Time trace of meridional Mach number

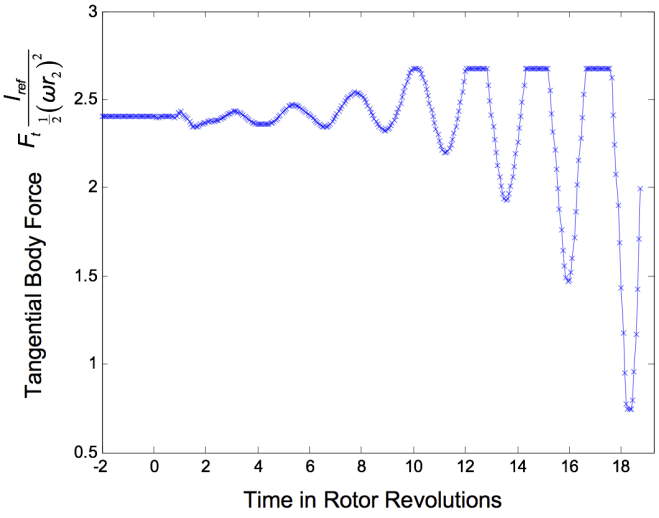

(b) Time trace of applied tangential body force

Figure 2-7: Extrapolation of flow quantities and body force components in diffuser passage, from Benneke [1].

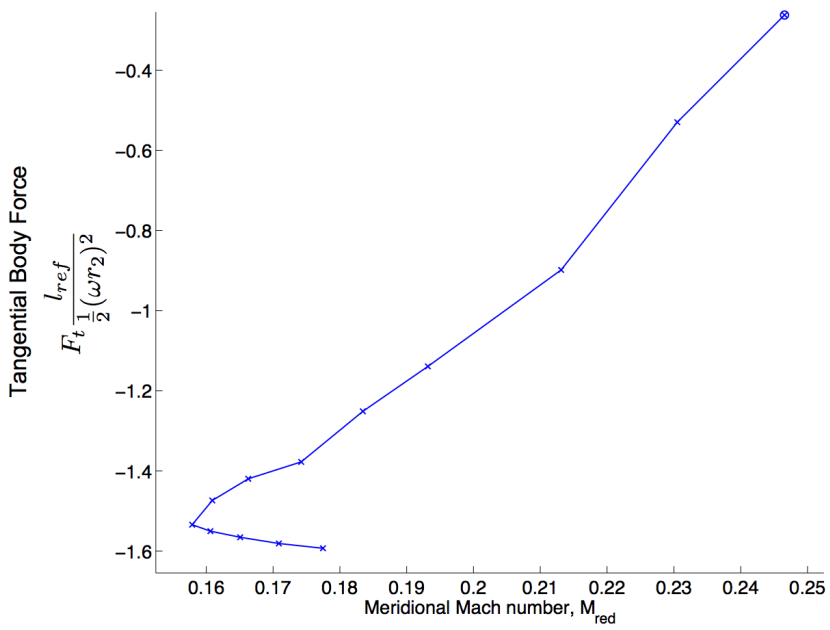

(a) $f_\theta\left(M_m\right)$ for grid point near shroud and diffuser leading edge

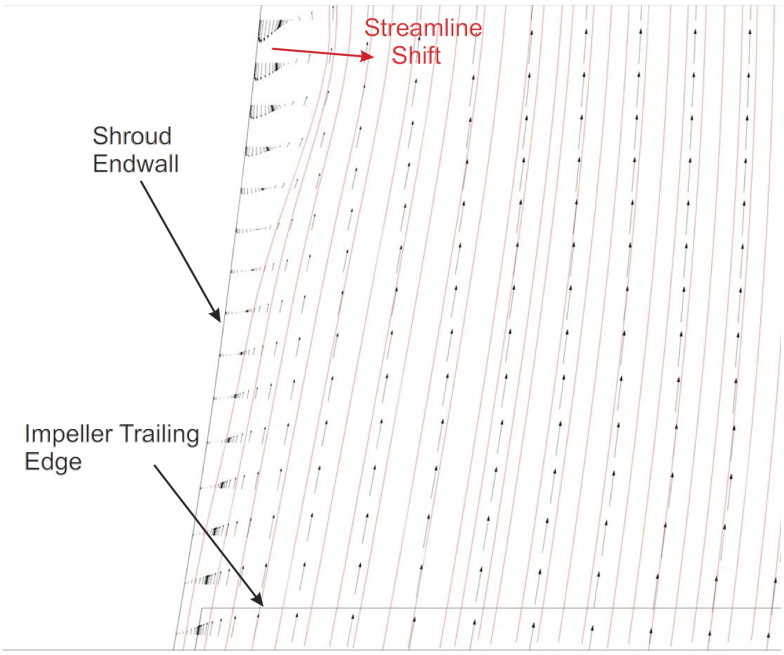

(b) Streamline shift due to separation bubble

Figure 2-8: Double value for grid point caused by streamline shift due to separation bubble, from Benneke [1].

Chapter 3

A Blade Passage Model for Centrifugal Compressors

3.1 Desired Attributes of New Body Force Model

Based on the advantages and challenges associated with the blade passage model for axial compressors and the control volume analysis method for centrifugal compressors, a new blade passage model for centrifugal compressors is derived. The developed model: (1) defines an analytical relationship between the local flow field and body force field, (2) bookkeeps fictitious forces in the rotating frame, and (3) presents the physical interpretation of the analytical relationships. Another attribute is that the model implementation is compatible with commercial CFD packages.

The developed model derives the normal and viscous parallel force as a function of the relative flow field,

$$\mathbf{f} = \mathbf{f}(\mathbf{w}) \ , \tag{3.1}$$

where, for each possible set of relative flow field quantities, $\mathbf{w}$, a unique body force vector, $\mathbf{f}$, is computed. The model is derived directly from first principles and captures the appropriate scaling of the body forces with respect to the local flow field. Finally, extrapolation challenges are addressed by the analytical nature of the model.

The blade passage model for axial compressors explicitly assumed that there was no radial shift of streamlines. This assumption is not appropriate for centrifugal compressor applications in which the centrifugal and Coriolis forces are of the same order of magnitude as the pressure and inertial forces. When the gas path angle, φ, shown in Fig. 3-1, is zero, the gas path and through-flow are axial and the centrifugal

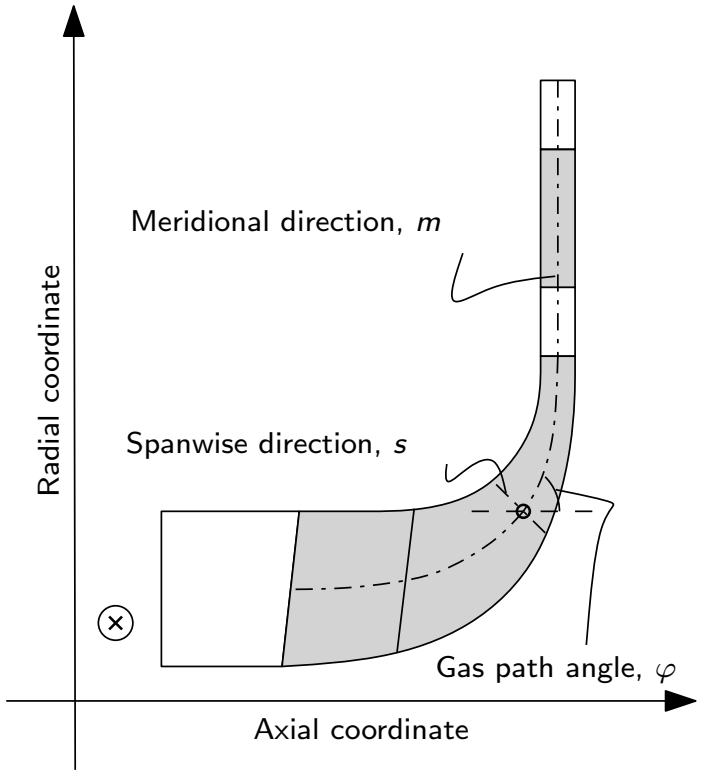

Figure 3-1: Meridional view of compressor gas path.

forces are radial, with no component in the meridional direction. The Coriolis forces are zero. In the case of $\varphi = 90°$, the gas path and through-flow are radial and both the centrifugal and Coriolis forces act in the meridional direction. Typical values of φ encountered in axial and centrifugal compressors can range between 15° and 90°.

Compatibility with existing design tools is addressed by formulating the body force field source terms in a manner consistent with the source term implementation in computational solvers. Most commercial solvers use the conservation form of the

Navier-Stokes equations,

$$\frac{\partial}{\partial t}\int_V \mathbf{U}dV + \int_{\mathbf{S}} \mathbf{F}\cdot\mathbf{S} - \int_{\mathbf{S}} \mathbf{G}\cdot\mathbf{S} = \int_V \mathbf{S}_T dV \ , \tag{3.2}$$

where V is the volume of the computational cell, $\mathbf{S}$ is the outward pointing normal vector of the surface of the computational cell, $\mathbf{U}$ is the state vector, $\mathbf{F}\cdot\mathbf{S}$ represents the momentum flux and pressure forces, $\mathbf{G}\cdot\mathbf{S}$ represents the viscous and heat transfer terms, and $\mathbf{S}_T$ are source terms. There are five components to Eq. 3.2, mass, three momentum components, and energy.

The body force field is implemented through the source term vector, $\mathbf{S}_T$, on the right hand side of the governing equations. Benneke's [1] implementation used an in-house Euler code with access to the left hand side of Eq. 3.2. This allowed for accounting of blade metal blockage on the left hand side. The model developed here derives expressions for the blade metal blockage which are implemented on the right hand side of Eq. 3.2.

3.1.1 Implementation Methodology for Blade Passage Model

Using the desired attributes from above, a methodology for implementing the blade passage model, based on single passage RANS simulations is developed and illustrated in Fig. 3-2. The process begins with a series of 3D single passage RANS simulations of a given compressor geometry. The body force field necessary to reconstruct the pitchwise averaged flow field is extracted from the single passage RANS simulations and used to define the first principles-based inputs to the blade passage model. Once these inputs have been defined, they can be used in a body force simulation and an unsteady perturbation analysis may be used to assess compressor stability. It is worth noting that the inputs to the blade passage model are not limited to being defined by the presented body force field extraction method. The inputs can be defined through another method of extracting the body force field or from experiments. Single passage RANS are used in the current methodology because the simulations do not require experimental or empirical data and are computationally inexpensive.

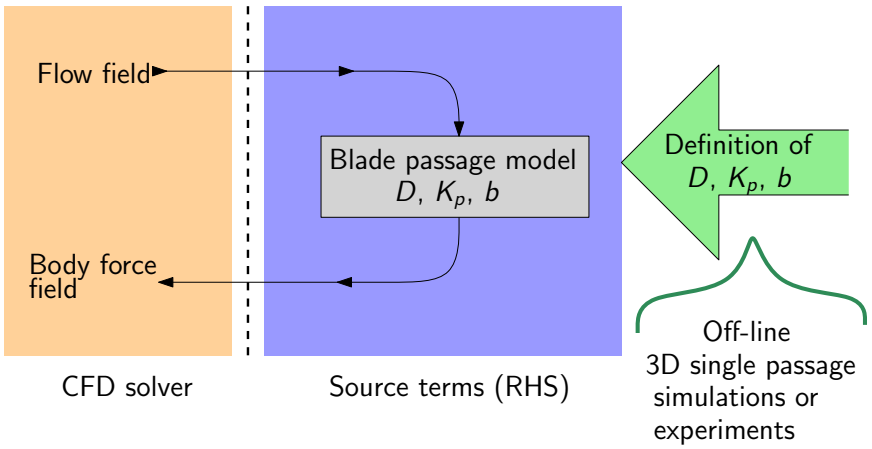

Figure 3-2: Body force blade passage model implementation methodology.

3.2 Derivation of Blade Passage Model

Based on the above desired attributes, a blade passage model is derived for centrifugal compressors. The model yields source terms for the right hand side of the mass, momentum, and energy conservation equations.

$$\frac{\partial \rho}{\partial t} + \nabla_m \cdot (\rho \mathbf{u}) = S_{\text{mass}} \tag{3.3}$$

$$\frac{\partial}{\partial t}(\rho \mathbf{u}) + \nabla_m \cdot \left[\left(\rho \mathbf{u} + p \underline{\underline{I}} \right) \right] = \mathbf{S}_{\text{mom}} \tag{3.4}$$

$$\frac{\partial}{\partial t}(\rho e_t) + \nabla_m \cdot (\rho h_t \mathbf{u}) = S_{\text{energy}} \ . \tag{3.5}$$

$\underline{\underline{I}}$ is an identity matrix, and e_t is the absolute stagnation internal energy such that, $h_t = e_t + {}^{p}/_{\rho}$. The model consists of three components, the normal force model, the viscous parallel force model, and the blade metal blockage model. The normal force model is based on the force balance for a relative streamline. The viscous parallel force model is based on the relation between the drag power and wake entropy flux of an airfoil. The blade metal blockage model derivation is based on the pitchwise averaged governing equations that account for blade metal thickness and is the only model that provides a source term for the continuity equation, Eq. 3.3.

The geometry definitions used to define the normal and parallel directions with respect to the relative streamline are developed in App. A.

3.2.1 Normal Force Model

The normal force model is based on the balance of pressure forces, Coriolis forces, and centrifugal forces in the direction normal to the relative streamline. The derivation begins with the momentum equation for the pitchwise averaged relative streamline,

$$\mathbf{w} \cdot \nabla_m \mathbf{w} = -\frac{1}{\rho} \nabla_m p - 2\mathbf{\Omega} \times \mathbf{w} - \mathbf{\Omega} \times (\mathbf{\Omega} \times \mathbf{r}) + \mathbf{f} \ , \tag{3.6}$$

where $\mathbf{w}$ is the relative velocity vector and $\mathbf{\Omega}$ is the blade row rotation vector. The term on the left hand side of Eq. 3.6 is the relative streamline acceleration while the terms on the right hand side are the pressure, Coriolis, centrifugal, and body forces, respectively. Figure 3-3 depicts the forces acting on a fluid particle moving along a pitchwise averaged relative streamline. Taking the component normal to the relative

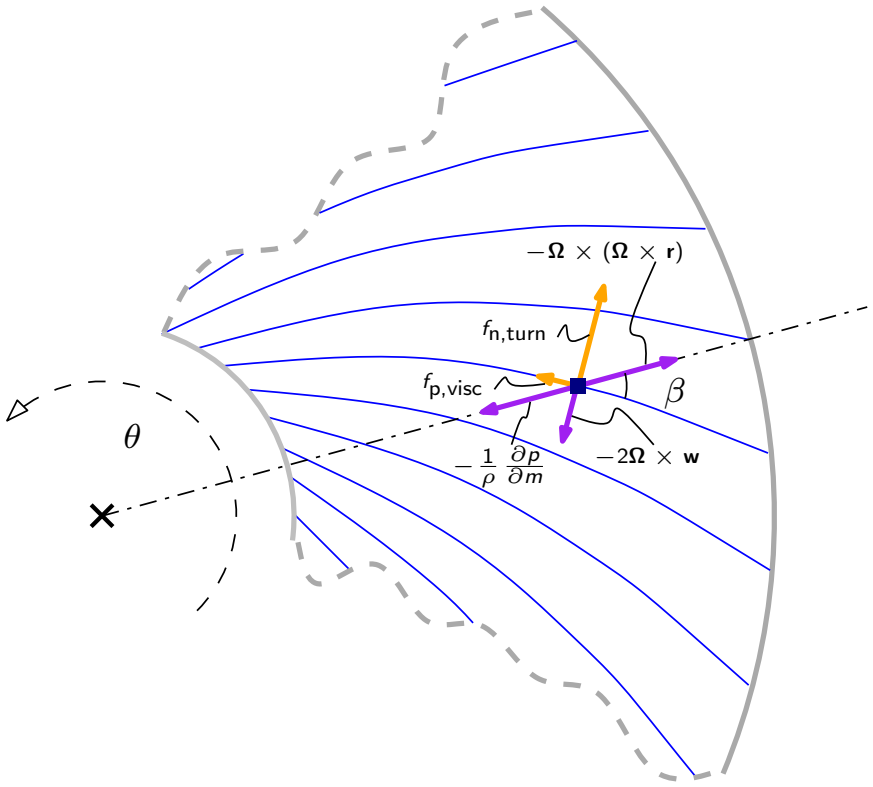

Figure 3-3: Force balance along a relative streamline.

streamline provides[1],

$$w^2\left(\frac{\partial\beta}{\partial\ell}-\sin\lambda\frac{\partial\varphi}{\partial m}\cos\beta+\frac{\sin\beta\cos^2\lambda\sin\varphi}{r}\right)=-\frac{1}{\rho}\frac{\partial p}{\partial n}$$
$$-2\Omega w\cos\lambda\sin\varphi-\Omega^2 r\left(\cos\beta\sin\lambda\cos\varphi+\sin\beta\sin\varphi\right)+f_{\text{n,turn}}\ , \tag{3.7}$$

where w is the relative velocity magnitude, β is the relative flow angle with respect to the meridional direction in the plane normal to the modeled blade, λ is the blade lean angle from the spanwise direction, φ is the gas path angle, m is the meridional direction, and $f_{\text{n,turn}}$ is the normal force. Rearranging the equation to solve for the body force provides an expression for the body force as a function of local flow quantities in the relative frame,

$$f_{\text{n,turn}}=w^2\left(\frac{\partial\beta}{\partial\ell}-\sin\lambda\frac{\partial\varphi}{\partial m}\cos\beta+\frac{\sin\beta\cos^2\lambda\sin\varphi}{r}\right)+\frac{1}{\rho}\frac{\partial p}{\partial n}$$
$$+2\Omega w\cos\lambda\sin\varphi+\Omega^2 r\left(\cos\beta\sin\lambda\cos\varphi+\sin\beta\sin\varphi\right)\ . \tag{3.8}$$

The normal force on a fluid particle is modeled as the difference between the curvature of a given pitchwise averaged relative streamline and the pressure, Coriolis, and centrifugal forces. The first term on the right hand side represents the turning of the relative streamline. The third and fourth terms on the right hand side are the Coriolis and centrifugal forces, respectively, which arise from formulating the model in a non-inertial, rotating frame.

Definition of Deviation Gradient Parameter. The only empirical input for the normal force model is the deviation gradient parameter, D, which is the nondimensionalized streamwise gradient of local flow deviation defined as,

$$D=r_2\frac{\partial\delta}{\partial\ell}\ . \tag{3.9}$$

[1]The coordinate system and geometry definitions for Eq. 3.7 are defined in App. A.

Consider the local deviation, δ, defined as,

$$\delta = \beta - \kappa \ , \tag{3.10}$$

where κ is the blade metal angle. The streamwise gradient of the relative flow angle, $\frac{\partial \beta}{\partial \ell}$ can be expanded,

$$\frac{\partial \beta}{\partial \ell} = \frac{\partial \kappa}{\partial \ell} + \frac{\partial \delta}{\partial \ell} = \frac{\partial \kappa}{\partial m} \cos\beta + \frac{D}{r_2} \ , \tag{3.11}$$

where the expansion of $\frac{\partial \kappa}{\partial \ell} = \frac{\partial \kappa}{\partial m} \cos\beta$ splits up the streamwise gradient of the blade metal angle into a geometric component, $\frac{\partial \kappa}{\partial m}$, and a flow field component, $\cos\beta$. Combining Eq. 3.8 and Eq. 3.9 yields,

$$\begin{aligned} f_{\text{n,turn}} =& w^2 \left(\frac{\partial \kappa}{\partial m} \cos\beta - \sin\lambda \frac{\partial \varphi}{\partial m} \cos\beta + \frac{\sin\beta \cos^2\lambda \sin\varphi}{r} \right) + \frac{1}{\rho} \frac{\partial p}{\partial n} \\ &+ 2\Omega w \cos\lambda \sin\varphi + \Omega^2 r \left(\cos\beta \sin\lambda \cos\varphi + \sin\beta \sin\varphi \right) + w^2 \frac{D}{r_2} \ . \end{aligned} \tag{3.12}$$

In the above equation, $f_{\text{n,turn}}$ is computed from the blade geometry, local flow field quantities, and the deviation gradient parameter D. The geometry terms are $\frac{\partial \kappa}{\partial m}$, λ, $\frac{\partial \varphi}{\partial m}$, and φ. The flow field quantities are w, β, ρ, and $\frac{\partial p}{\partial n}$.

The deviation gradient parameter is a measure of the effect of boundary layer growth on streamline curvature. Although the normal force is the inviscid component of the body force field, and not responsible for entropy generation, D captures the effect of boundary layer displacement on the turning of the relative streamline. The D parameter is the only empirical input to the model and can be obtained from CFD calculations or experiments.

Recasting the Normal Force Model

Preliminary calculations using the normal force model identified a positive feedback loop between the normal force model and the resulting flow field which leads to numerical instabilities. Figure 3-4 shows the normal force extracted directly from

single passage CFD simulations for a radial impeller with prismatic blades and the normal force computed by Eq. 3.12 at various iterations in the simulation.

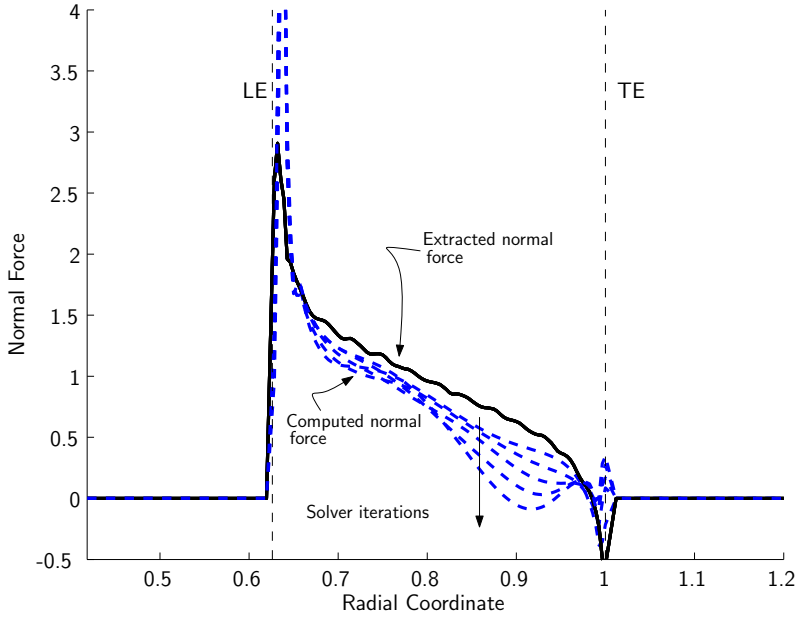

Figure 3-4: Body force model simulation showing numerical instability.

The observed static instability, schematically shown in Fig. 3-5, begins with a slight under prediction in the normal force model. Based on the influence coefficient analysis in App. B a reduction in $f_{\mathrm{n,turn}}$ results in a reduction in $\frac{1}{\rho}\frac{\partial p}{\partial m}$, and based on Eq. 3.12, a reduction in $\frac{1}{\rho}\frac{\partial p}{\partial m}$ yields a lower $f_{\mathrm{n,turn}}$ which leads to divergence. The same behavior occurs for a slight over prediction in the normal force model.

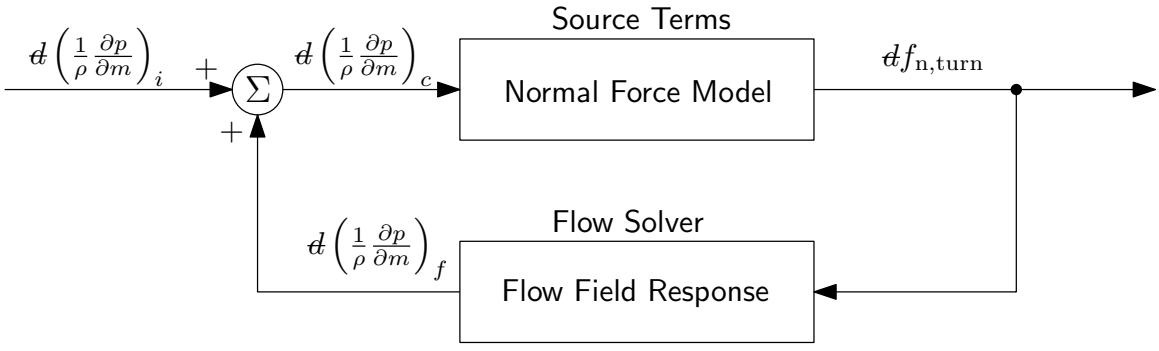

Figure 3-5: Schematic of numerical instability in normal force model.

The issue is that the normal force model depends on both the resulting velocity

field and pressure gradient, which in turn are coupled through the flow solver. The instability can be avoided by expressing the normal force through the velocity field only. A compressible flow influence coefficient analysis is carried out to derive an expression for the static pressure gradient dependent on only velocity components. The pressure gradient normal to the relative streamline, taken from App. B is,

$$\begin{aligned}\frac{1}{\rho}\frac{\partial p}{\partial n} =& \frac{u^2}{r}\left[\frac{-\cos\varphi\sin\lambda\cos\beta-\sin\varphi\sin\beta}{1-M_m^2}\right]+f_{\text{n,turn}}\left[\frac{\sin^2\beta\left(1+\sin^2\lambda\left(\gamma-1\right)M_m^2\right)}{1-M_m^2}\right]\\ &+f_{\text{p,visc}}\left[\frac{-\cos\beta\sin\beta\left(1+\left(\gamma-1\right)M_{rel}^2\left(1-\sin^2\lambda\sin^2\beta\right)\right)}{1-M_m^2}\right]. \end{aligned} \tag{3.13}$$

Substituting the above equation into Eq. 3.12 yields an expression for $f_{\text{n,turn}}$ in terms of velocities and body forces,

$$\begin{aligned}f_{\text{n,turn}} =& w^2\left(\frac{\partial\kappa}{\partial m}\cos\beta-\sin\lambda\frac{\partial\varphi}{\partial m}\cos\beta+\frac{\sin\beta\cos^2\lambda\sin\varphi}{r}\right)\\ &+\frac{u^2}{r}\left[\frac{-\cos\varphi\sin\lambda\cos\beta-\sin\varphi\sin\beta}{1-M_m^2}\right]+f_{\text{n,turn}}\left[\frac{\sin^2\beta\left(1+\sin^2\lambda\left(\gamma-1\right)M_m^2\right)}{1-M_m^2}\right]\\ &+f_{\text{p,visc}}\left[\frac{-\cos\beta\sin\beta\left(1+\left(\gamma-1\right)M_{rel}^2\left(1-\sin^2\lambda\sin^2\beta\right)\right)}{1-M_m^2}\right]\\ &+2\Omega w\cos\lambda\sin\varphi+\Omega^2 r\left(\cos\beta\sin\lambda\cos\varphi+\sin\beta\sin\varphi\right)+w^2\frac{D}{r_2}. \end{aligned} \tag{3.14}$$

The above equation is rearranged to provide an expression for the normal force as a function of only velocities and $f_{\text{p,visc}}$,

$$\begin{aligned}f_{\text{n,turn}} =& \left[\frac{1}{1-\frac{\sin^2\beta\left(1+\sin^2\lambda(\gamma-1)M_m^2\right)}{1-M_m^2}}\right]\left\{w^2\left[\frac{\partial\kappa}{\partial m}\cos\beta-\sin\lambda\frac{\partial\varphi}{\partial m}\cos\beta+\frac{\sin\beta\cos^2\lambda\sin\varphi}{r}\right]\right.\\ &+2\Omega w\left[\cos\lambda\sin\varphi\right]+\Omega^2 r\left[\cos\beta\sin\lambda\cos\varphi+\sin\beta\sin\varphi\right]+\frac{u^2}{r}\left[\frac{-\cos\varphi\sin\lambda\cos\beta-\sin\varphi\sin\beta}{1-M_m^2}\right]\\ &\left.+f_{\text{p,visc}}\left[\frac{-\cos\beta\sin\beta\left(1+\left(\gamma-1\right)M_{rel}^2\left(1-\sin^2\lambda\sin^2\beta\right)\right)}{1-M_m^2}\right]+w^2\frac{D}{r_2}\right\}. \end{aligned} \tag{3.15}$$

The stabilizing effect of recasting the normal force model to depend only on the velocity and the viscous parallel force can be seen as follows. A slight increase in

$f_{\text{n,turn}}$ tends to decrease w and leads to a reduced $f_{\text{n,turn}}$, as computed by Eq. 3.15, which opposes the initial perturbation.

3.2.2 Viscous Parallel Force Model

The viscous parallel force model is derived by examining the lost work due to viscous dissipation in the boundary layer of an airfoil as shown in Fig. 3-6 [18].

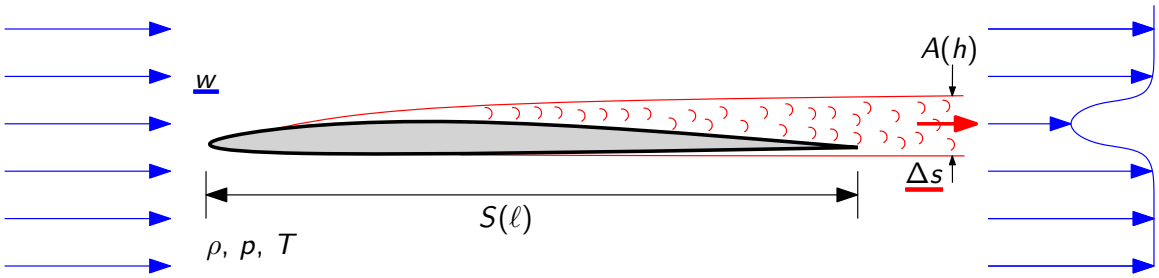

Figure 3-6: Relationship between drag power and wake entropy flux of an airfoil.

The airfoil drag power due to the entropy flux in the wake yields,

$$\text{Drag Power} = T\Delta s \rho A w = \frac{1}{2}\rho w^3 S C_D \ , \tag{3.16}$$

where T is the local static temperature, Δs is the specific entropy change in the boundary layer, ρ is the local density, w is the relative velocity, A is the area of the wake perpendicular to the freestream, S is the surface area of the airfoil, and C_D is the drag coefficient. Rearranging to solve for the entropy rise gives,

$$T\Delta s = w^2 \frac{S}{A} C_D = w^2 \frac{\ell}{h} C_D \ , \tag{3.17}$$

where the area ratio S/A can be simplified to $S/A = \ell/h$, where ℓ is the chord and h is the wake area per unit span. For an infinitesimal chord element, $d\ell$, Eq. 3.17 becomes,

$$T\frac{ds}{d\ell} = C_D \frac{w^2}{h} \ . \tag{3.18}$$

When averaging the entropy generation in a blade passage in the tangential direction, h becomes the blade pitch, $\frac{2\pi r_2}{N_B}$, where r_2 is the impeller exit radius and N_B is the number of blades. This leads to the viscous parallel force model,

$$f_{\mathrm{p,visc}} = K_p \frac{w^2}{r_2} \ , \tag{3.19}$$

where K_p is the viscous parallel force coefficient, similar to an airfoil drag coefficient.

3.2.3 Blade Metal Blockage Model

The effect of the blade metal blockage on flow displacement is not bookkept by the normal force or viscous parallel force models and must be accounted for by a separate model. The blade metal blockage model depends on the blade metal blockage parameter b which is defined here on a two dimensional basis as the circumferential blade gap normalized by the blade pitch, shown in Fig. 3-7.

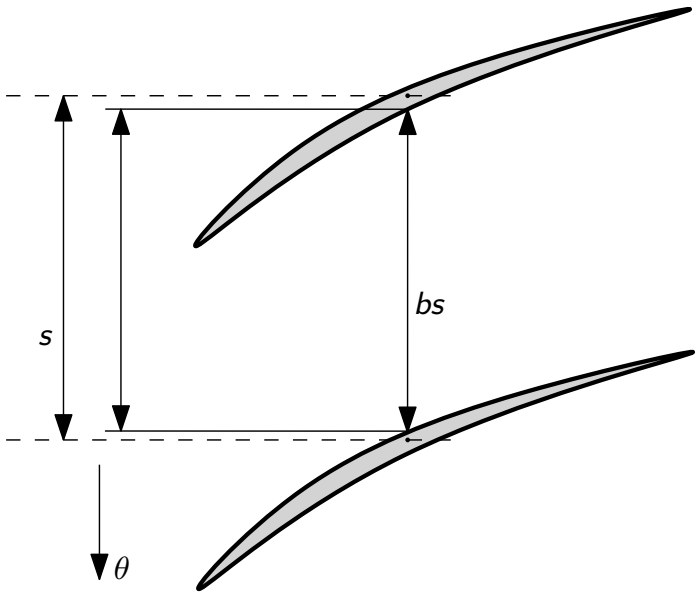

Figure 3-7: Definition of blade metal blockage parameter, b.

The parameter, b, can be computed from the blade geometry by,

$$b = 1 - \frac{N_B t(x,r)}{2\pi r} = \frac{N_B \left(\theta_{ss} - \theta_{ps}\right)}{2\pi} \ , \tag{3.20}$$

where t is the blade thickness measured in the circumferential direction, and θ_{ss} and θ_{ps} are the circumferential coordinates of the suction side and pressure side of the blade.

The model is derived by examining the pitchwise averaged governing equations,

$$\frac{\partial}{\partial t}\left(b\rho\right) + \nabla_m \cdot \left(b\rho\mathbf{u}\right) = 0 \tag{3.21}$$

$$\frac{\partial}{\partial t}\left(b\rho\mathbf{u}\right) + \nabla_m \cdot \left[\left(b\rho\mathbf{u} + p\underline{\underline{I}}\right)\right] = p\nabla_m b + \rho b\mathbf{f} \tag{3.22}$$

$$\frac{\partial}{\partial t}\left(b\rho e_t\right) + \nabla_m \cdot \left(b\rho h_t\mathbf{u}\right) = \rho b\Omega r f_\theta \ . \tag{3.23}$$

Equation 3.21 shows that the mass flow through the effective flow area is conserved. Equation 3.22 highlights the body force field, $\mathbf{f}$, as responsible for changes in momentum, again, through the area reduced by the blockage. An in-depth explanation of the $p\nabla_m b$ term is given in [22]. Finally, Eq. 3.23 shows that for an adiabatic axisymmetric flow field, the only change in stagnation enthalpy comes from a torque applied at a given rotational speed, essentially a restatement of the Euler turbine equation.

Equations 3.21-3.23 are manipulated so that all terms with b are moved to the right hand side of the equations, consistent with the secondary attribute described in Sec. 3.1. The chain rule is applied to the partial derivatives and terms are moved to the right hand side to give

$$\frac{\partial \rho}{\partial t} + \nabla_m \cdot \left(\rho\mathbf{u}\right) = \underbrace{-\frac{1}{b}\left(\rho\mathbf{u} \cdot \nabla_m b\right)} \tag{3.24}$$

$$\frac{\partial}{\partial t}\left(\rho\mathbf{u}\right) + \nabla_m \cdot \left[\left(\rho\mathbf{u} + p\underline{\underline{I}}\right)\right] = \rho\mathbf{f} \underbrace{-\frac{1}{b}\left(\rho\mathbf{u}\mathbf{u} \cdot \nabla_m b\right)} \tag{3.25}$$

$$\frac{\partial}{\partial t}\left(\rho e_t\right) + \nabla_m \cdot \left(\rho h_t\mathbf{u}\right) = \rho\Omega r f_\theta \underbrace{-\frac{1}{b}\left(\rho h_t\mathbf{u} \cdot \nabla_m b\right)} \ , \tag{3.26}$$

where the indicated terms comprise the blade metal blockage model. The common term between the blade metal blockage source terms is $-\frac{1}{b}\left(\rho\mathbf{u} \cdot \nabla_m b\right) A$ where $A = 1$ for the continuity equation, $A = \mathbf{u}$ for the momentum equation, and $A = h_t$ for the energy equation. This common term represents the amount of A that needs to

added into the flow field to maintain the same mass-averaged value for A in the axisymmetric flow field as in the flow field with discrete blades. When the blade thickness is increasing, $\nabla_m b$ is negative, and $-\frac{1}{b}(\rho \mathbf{u} \cdot \nabla_m b)$ is positive, representing addition of A into the flow field, and vice versa for decreasing blade thickness. Note that the common term in the blade metal blockage model is similar to the external flow slender body theory source term [10] of $V_\infty \frac{\partial t}{\partial x}$ where V_∞ is the freestream velocity and $\frac{\partial t}{\partial x}$ is the body thickness gradient in the direction of the freestream.

While the normal force and viscous parallel force models yield source terms in the momentum and energy equations, they do not affect the continuity equation.

3.3 Body Force Field Implementation in Commercial CFD Packages

The body force blade passage model implementation was carried out in two commercial CFD packages, FINE/Turbo and FINE/Open with OpenLabs, both developed by Numeca International. Implementation of the body force source terms in FINE/Turbo was carried out in a non-standard version so as to implement source terms. The OpenLabs environment in FINE/Open readily allows implementing source terms.

The differences between the CFD packages are in the ability to implement the blade metal blockage model and in the fidelity of implementing a given model input distribution. Implementation of the blade passage model requires storing distributions of data, e.g., distributions of φ, D, or b, all as functions of space, in order to compute the blade passage body forces.

Preliminary simulations with FINE/Turbo revealed a limitation with the implementation of the blade metal blockage model. It was found that the source term implementation in FINE/Turbo does not bookkeep the energy source term due to blade metal blockage appropriately, leading to spurious, non-physical results. This meant that the blade metal blockage model could not reliably be implemented in FINE/Turbo.

However, FINE/Turbo is a structured solver that allows distributions to be stored directly to individual grid nodes. This feature is in contrast to the unstructured nature of the FINE/Open-OpenLabs environment which required storing distributions by polynomial fits as a function of space. A summary of how each solver handles the energy equation source term for blade metal blockage and the fidelity of storing distributions is presented in Tab. 3.1.

Table 3.1: Fidelity of implementations in FINE CFD solvers.

CFD Solver\Attribute → ↓	Bookkeeping of Energy Source Term	Fidelity of Stored of Distributions
FINE/Turbo	✗	✓
FINE/Open	✓	✗

Ultimately, a CFD solver that allows distributions to be linked directly to the grid nodes and properly bookkeeps the energy source term for blade metal blockage is desired but was unavailable for the current work.

All single passage simulations were performed using FINE/Turbo. The validation of the body force field extraction on an axial compressor rotor, blade metal blockage model, and full blade passage model on a radial impeller used FINE/Open-OpenLabs because of its ability to model blade metal blockage. The diagnostics for the normal force model discussed in Chap. 7 used the FINE/Turbo source term implementation to leverage the fidelity of stored distributions.

Chapter 4

Extraction of Body Force Field from Single Passage CFD Simulations

For the current work, the empirical inputs to the blade passage model, b, D, and K_p, are defined through single passage CFD simulations. While b can be determined directly from geometry, D and K_p are computed by extracting the body force field required to reconstruct the axisymmetric mean flow field and using rearranged forms of Eqs. 3.15 and 3.19.

The methods to extract the body force field are validated on NASA Rotor 37, an axial compressor rotor described in Tab. 4.1. Further information on Rotor 37 can be found in [34].

Table 4.1: Rotor 37 data.

Number of blades, N_B	36
Inlet hub-to-tip radius ratio, r_{hub}/r_{tip}	0.7
Blade aspect ratio	1.19
Design total pressure ratio, PR	2.11
Design polytropic efficiency, η_p	0.889

The body force field extraction methodology is depicted in Fig. 4-1.

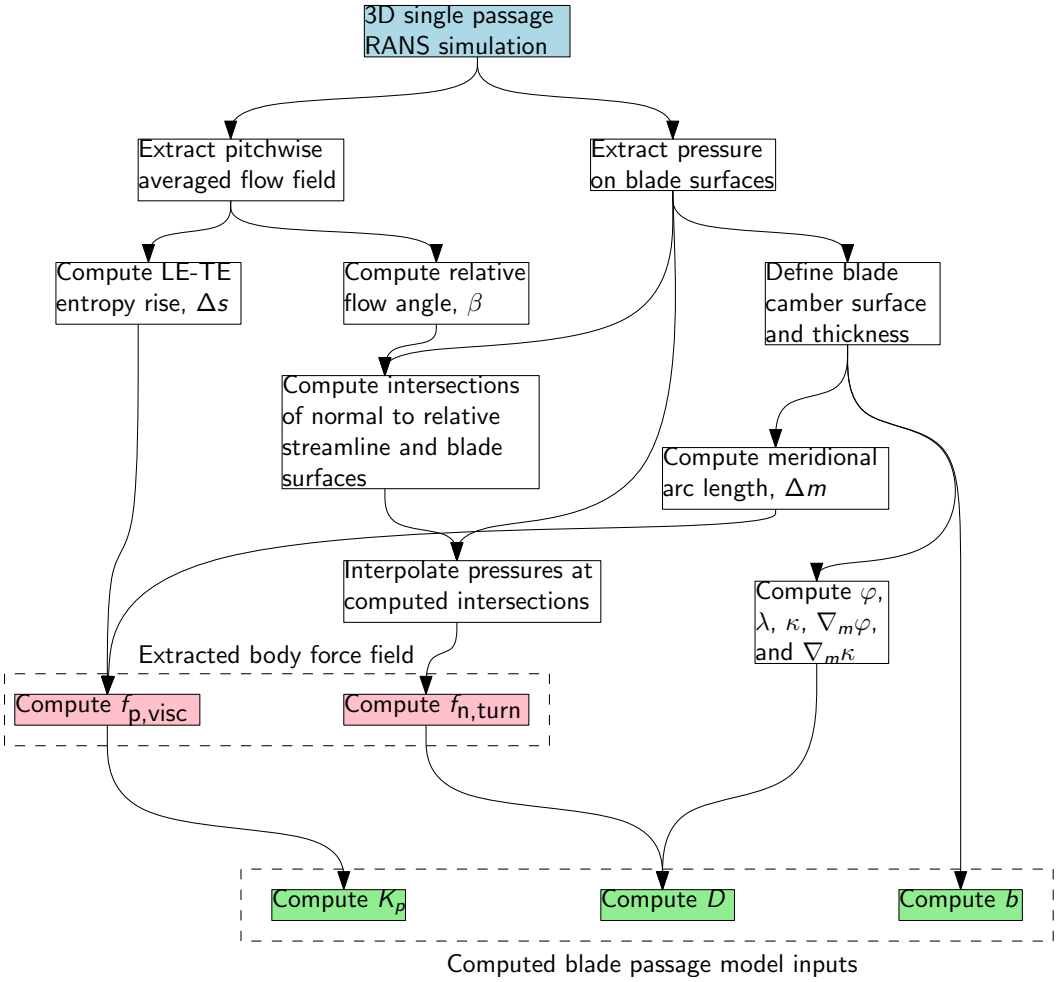

Figure 4-1: Extraction of body force field and computation of blade passage model inputs based on single passage RANS simulations.

4.1 Computational Setup of Single Passage RANS Simulations - Rotor 37

As noted in Sec. 3.3, the single passage simulation for all single passage calculations, including Rotor 37, were computed using the FINE/Turbo CFD package. FINE/Turbo is a comprehensive CFD package suited for turbomachinery applications and includes tools for generating structured multi block grids (Autogrid), solving viscous three dimensional compressible flow (EURANUS), and post-processing the results (CFView). A detailed description of FINE/Turbo can be found in [29].

Autogrid was used to generate a multi grid-compatible mesh for Rotor 37. The coarsest level of the mesh is shown in Fig. 4-2 for clarity. The grid for only one blade passage was generated to lower the computational cost and periodic boundary conditions were applied to model the repeating blade row. The number of grid nodes in the generated mesh was approximately 840,000. The EURANUS flow solver

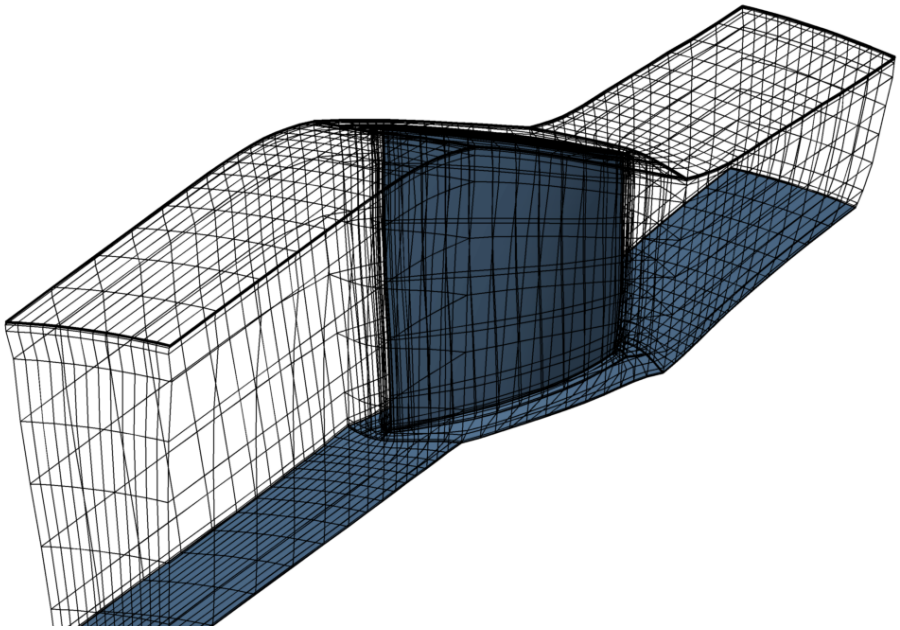

Figure 4-2: Coarse mesh of Rotor 37 shown for clarity. Actual mesh used for single passage RANS simulations is four times as dense in each direction.

in FINE/Turbo is capable of running on multiple processors and uses a multi grid

technique to accelerate solution convergence. The multi grid scheme cycles through solving the flow on coarse grids to reduce low frequency errors and interpolating the coarse solution to the fine grid to refine the solution. Both CFView and internally developed MATLAB and Python scripts were used to analyze and extract data from the flow solution.

The single passage RANS simulations used the Spalart-Almaras turbulence model to achieve closure of the governing equations. No mixing planes or sliding interfaces were required since only one blade is simulated.

The simulations were carried out using a specified total pressure and total temperature boundary condition at the inlet and a static pressure boundary condition with radial equilibrium at the exit. It has been noted that the exit static pressure boundary condition can lead to convergence problems when simulating operating points at low flow coefficients. However only one operating condition near design was investigated for the body force field extraction procedure and validation.

4.2 Definition of Blade Geometry

A meridional (axial and radial) description of the blade row is required since the body force field is applied in the swept volume of the blade row. The geometry of the compressor blade is extracted from single passage simulations by using the meridional blade camber surface defined by Smith and Merryweather [36] as the locus of points half the circumferential distance between the pressure and suction sides of the blade. The tangential distribution of the camber surface for a given (x, r) location is computed by,

$$\theta_{cs} = \frac{\theta_{ps} + \theta_{ss}}{2} \ , \tag{4.1}$$

where $\theta_{()}$ is the angular location of the given surface, i.e. ps is the pressure surface, ss is the suction surface, and cs is the camber surface. An example of blade camber surface with respect to the pressure and suction sides is depicted in Fig. 4-3 which

shows the tip region of the Rotor 37 blade. Figure 4-4 shows the meridional projection of the camber surface grid on which the body force field distribution is computed.

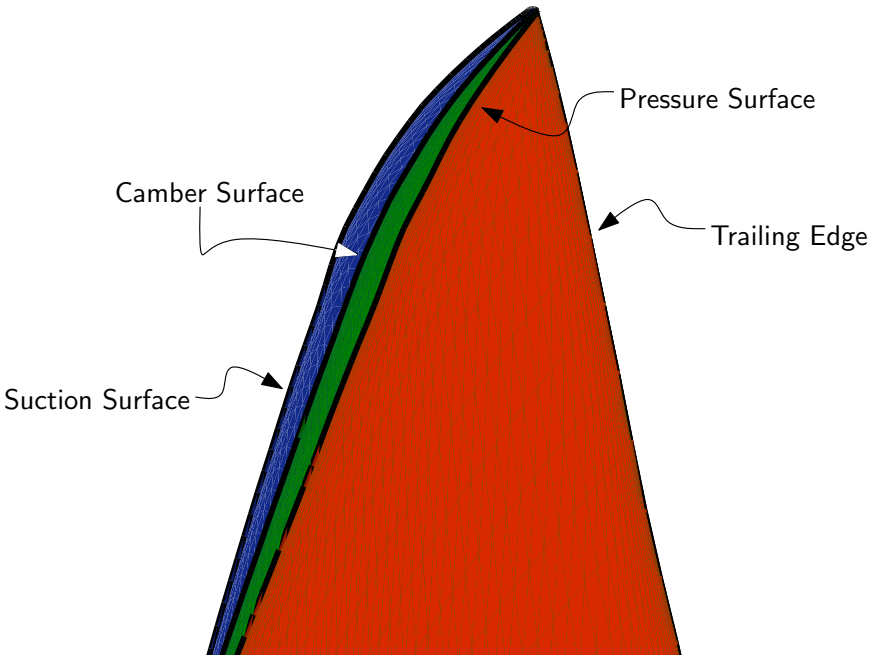

Figure 4-3: Definition of blade camber surface from [36].

The determination of the camber surface allows for the definition of the gas path angle, φ, the blade lean angle, λ, the blade metal angle, κ, while the blade thickness yields the blade metal blockage parameter, b, all as functions of x and r. The axisymmetric distributions of φ, λ, κ, and b, are presented in Figs. 4-5, 4-6, 4-7, and 4-8, respectively. The axes of these figures are the axial and radial dimensions normalized by the tip radius, r_2.

Figure 4-5 reflects the converging hub and shroud lines as positive and negative values of φ, respectively. The blade lean distribution, shown in Fig. 4-6 is on the order of a few degrees which indicates that the blade surfaces are mostly in the radial direction. The blade metal angle distribution in Fig. 4-7 shows the blade turning away from rotation as span increases in order to align with the relative flow. Figure 4-8 illustrates the increasing blade thickness towards mid chord and the decreasing blade thickness near the leading and trailing edges.

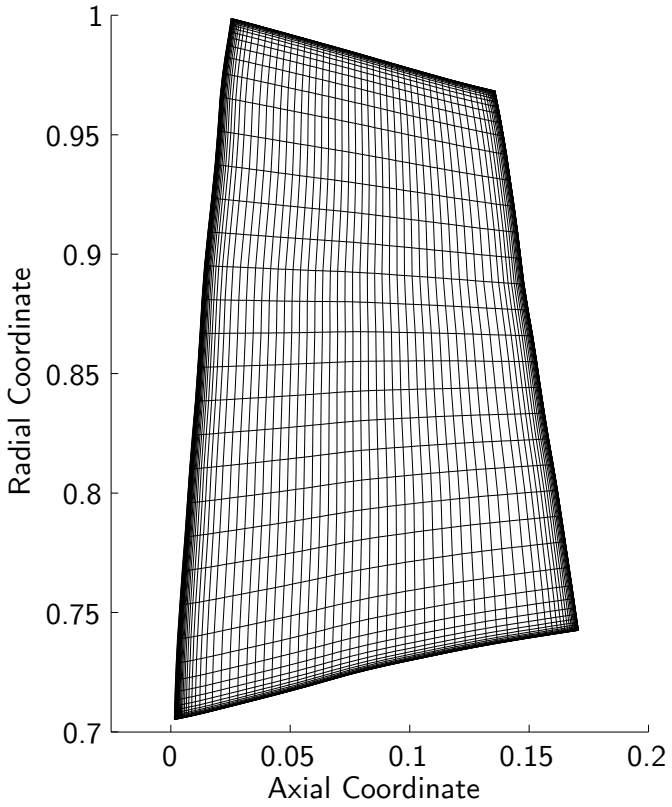

Figure 4-4: Rotor 37 meridional grid. Axes are non-dimensionalized by tip radius, r_2.

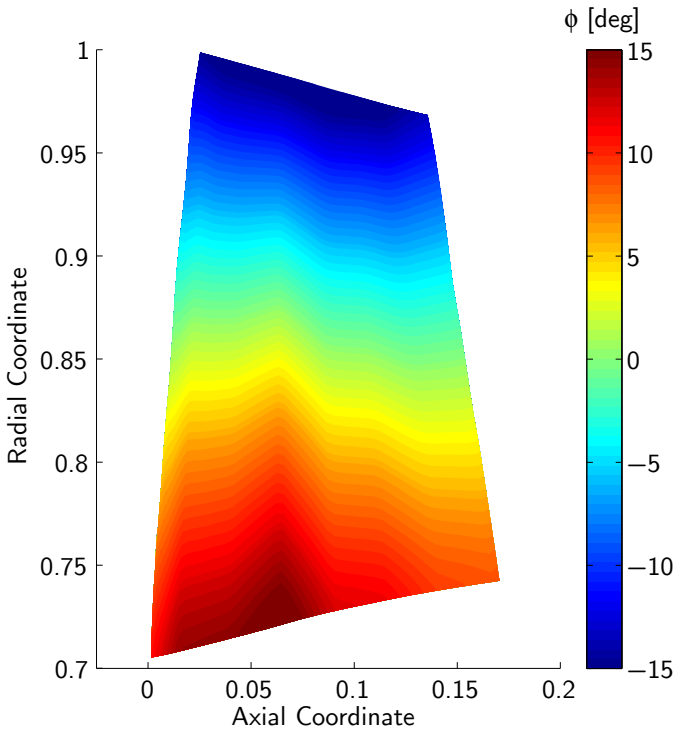

Figure 4-5: Rotor 37 gas path angle.

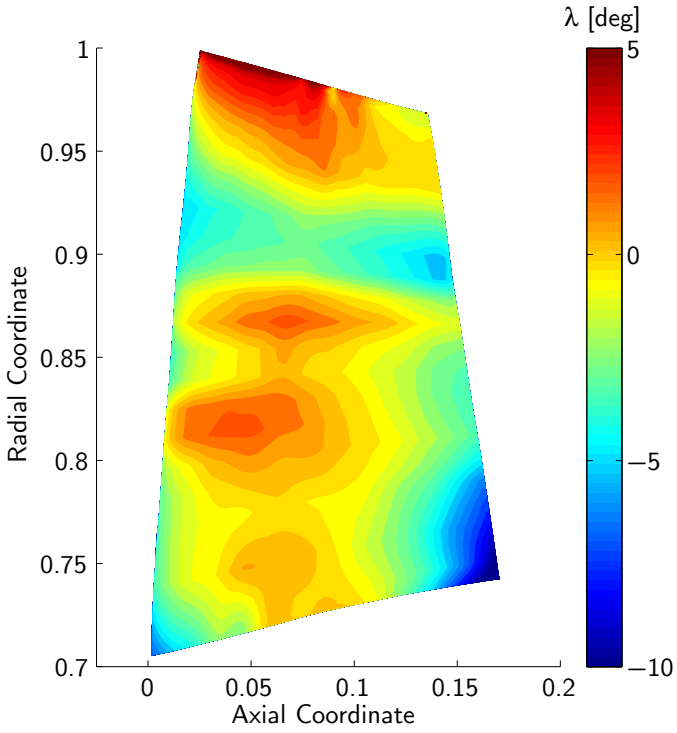

Figure 4-6: Rotor 37 blade lean angle.

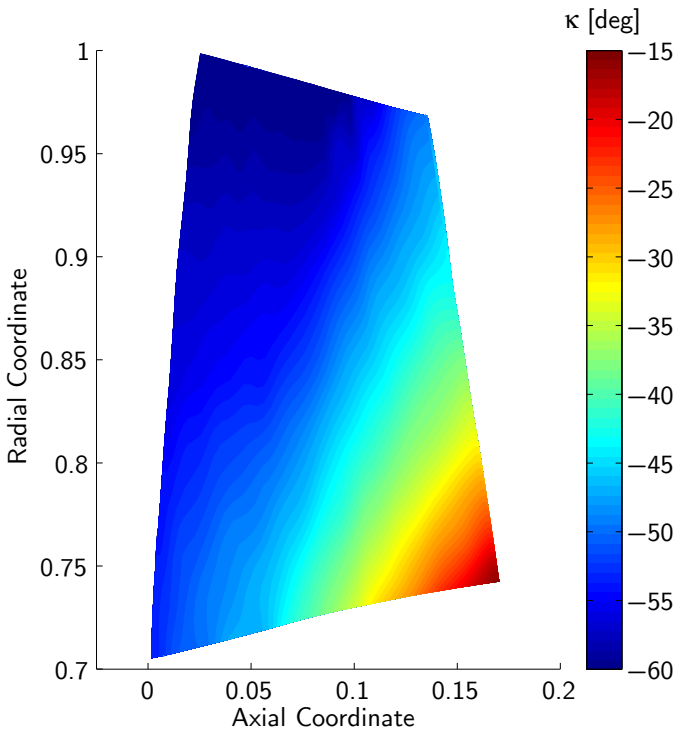

Figure 4-7: Rotor 37 blade metal angle.

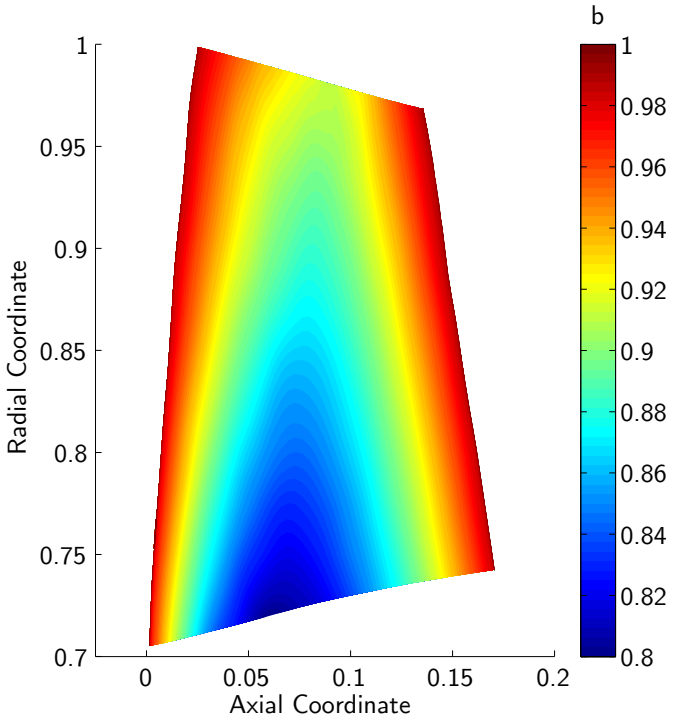

Figure 4-8: Rotor 37 blade metal blockage.

4.3 Extraction of Normal Force

The extraction of the normal force from a single passage RANS simulation is based on the blade loading shown in Fig. 4-9 and is computed by,

$$f_{\mathrm{n,turn}} = \frac{\Delta p_{\perp\beta}}{\rho s b \cos\beta} \ , \tag{4.2}$$

where $\Delta p_{\perp\beta} = p_{ps} - p_{ss}$ is the pressure difference across the blade in the direction normal to the relative streamline, ρ is the local pitchwise averaged density, s is the local blade pitch, b is a blade metal blockage parameter, and β is the relative flow angle of the pitchwise averaged flow field. With this definition, the normal force is computed as the blade loading distribution per unit mass within a blade passage. Calculation of the normal force requires determining the intersection between the

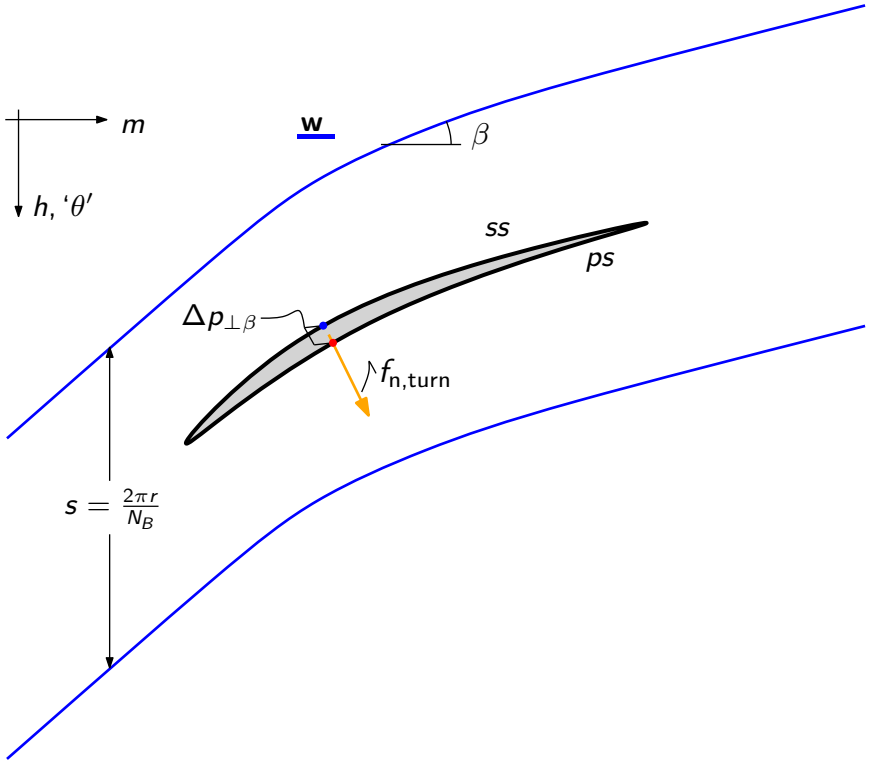

Figure 4-9: Extraction of normal force.

normal to the relative streamline and the pressure and suction side of the blades. The intersection is computed using the ray-triangle intersection method of Möller

and Trumbore [27], an example of which is shown in Fig. 4-10. The black arrow is the normal to the relative streamline while the red and blue stars are the computed intersection points on the pressure side and suction side respectively. The static pressures at these locations are used to compute the normal force.

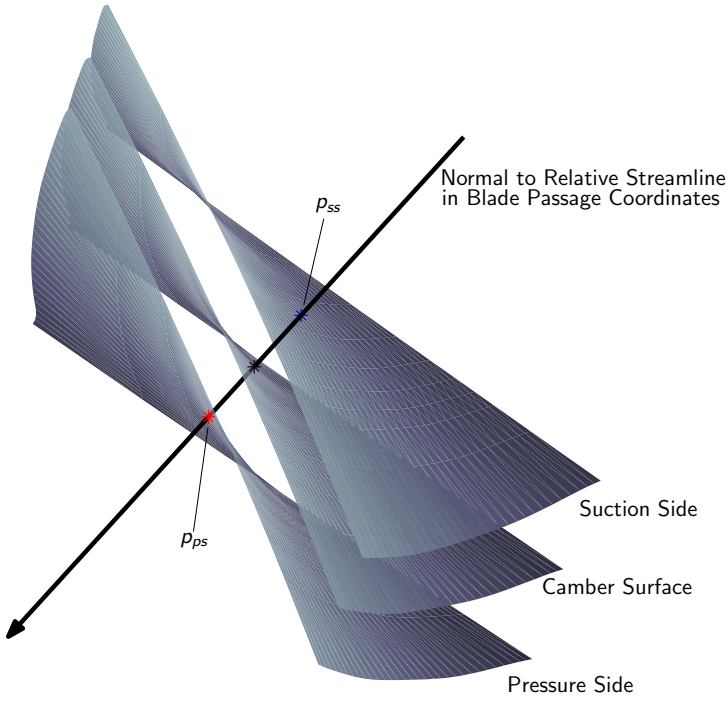

Figure 4-10: Intersection between normal to the relative streamline and blade pressure and suction surfaces.

The extracted normal force distribution from a Rotor 37 single passage RANS simulation near peak efficiency is shown in Fig. 4-11 with meridional distributions at the indicated spanwise locations shown in Fig. 4-12. The normal force (and viscous parallel force) values are normalized by centrifugal acceleration at the tip, $\Omega^2 r_2$.

The normal force distribution in Figs. 4-11 and 4-12 show sharp changes in the force near the airfoil leading edge and near 40% chord which is associated with the shock in the blade passage. For example, the pressure coefficient distribution at midspan depicted in Fig. 4-13 shows a sudden increase in suction side C_p due to the shock. This flow feature is responsible for the step shape of the normal force distribution at 40% chord.

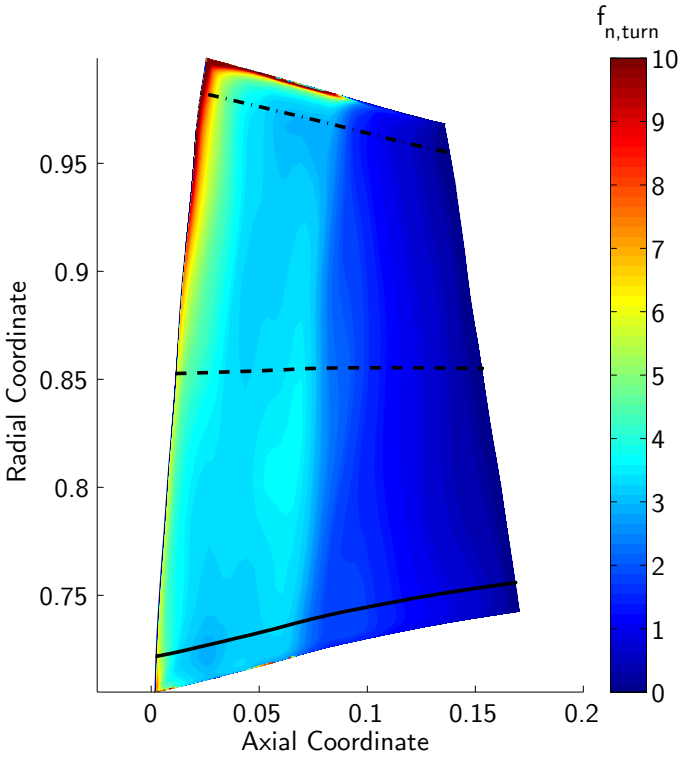

Figure 4-11: Normal force extracted from single passage RANS simulation. Lines indicate cuts for Fig. 4-12.

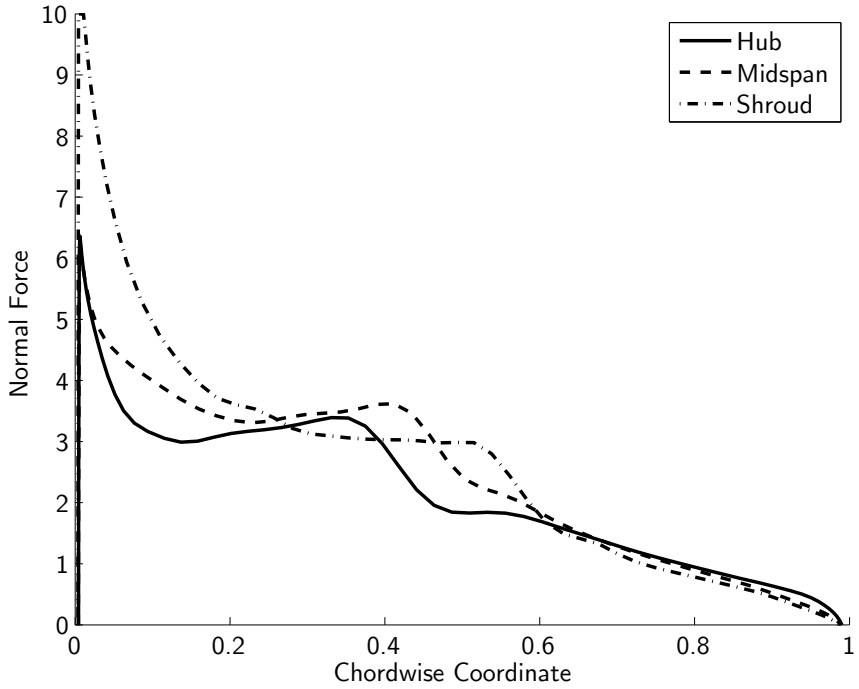

Figure 4-12: Meridional distributions of normal force extracted from single passage RANS simulations.

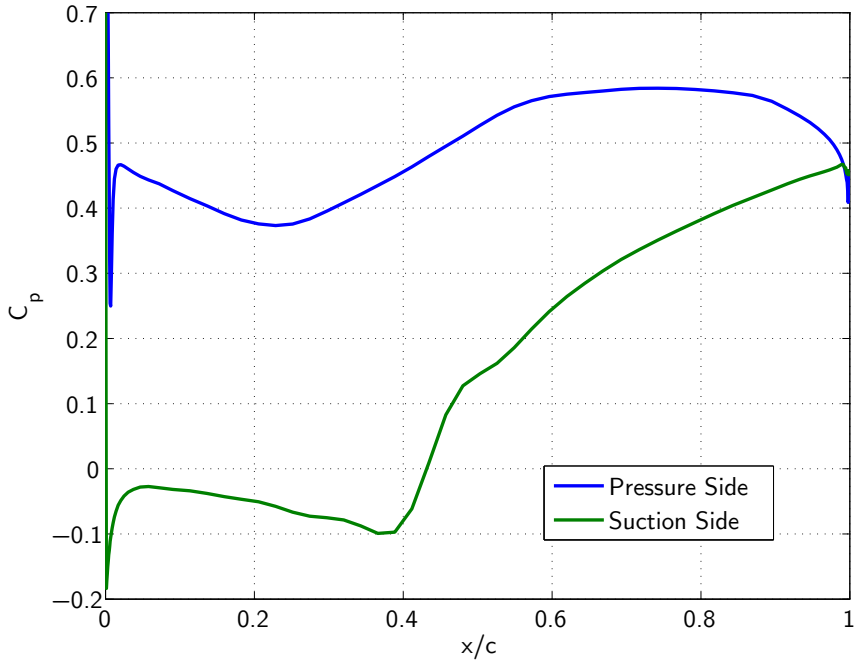

Figure 4-13: Pressure coefficient at midspan.

4.4 Extraction of Viscous Parallel Force

The viscous parallel force is determined form the entropy generated in the blade passage. Marble [25] defines the viscous parallel force ias,

$$f_{\mathrm{p,visc}} = T\frac{\partial s}{\partial \ell} = T\frac{\partial s}{\partial m}\cos\beta \tag{4.3}$$

where T is the local static temperature, $\frac{\partial s}{\partial m}$ is the meridional gradient of specific entropy, and β is the relative flow angle.

Using the gradient of entropy generation along gridlines available from the RANS simulation can result in negative $f_{\mathrm{p,visc}}$ values due to a mismatch between the meridional projection of three dimensional streamlines and the pitchwise averaged streamline. Figure 4-14 shows the relative streamlines starting from regions in the inner radius near solid surfaces and in the blade passage. The relative streamlines are colored by the local specific entropy. The streamlines with high entropy start near solid surfaces and experience large radial shifts in comparison to streamlines in the center of the blade passage. The large radial shifts occur because of secondary flow effects.

Figure 4-15 illustrates the mismatch between the meridional gridlines, the pitchwise averaged streamlines, and the radial shift of three-dimensional streamlines due to secondary flow effects. The pitchwise averaged streamlines do not capture the radial shift of the relative streamline near solid surfaces which can lead to spurious values of the extracted viscous parallel force when using the entropy gradient along the pitchwise averaged streamline.

In order to avoid negative force values, which implies $\frac{\partial s}{\partial \ell} < 0$ and violates the second law of thermodynamics, the viscous parallel force is extracted by taking the bulk entropy generation from the leading edge to the trailing edge,

$$f_{\mathrm{p,visc}} = T\frac{\Delta s}{\Delta m}\cos\beta\ , \tag{4.4}$$

where $\Delta s = s_{TE} - s_{LE}$, Δm is the meridional arc length from the leading edge to trailing edge, and β is the local relative flow angle. This approach was used to generate

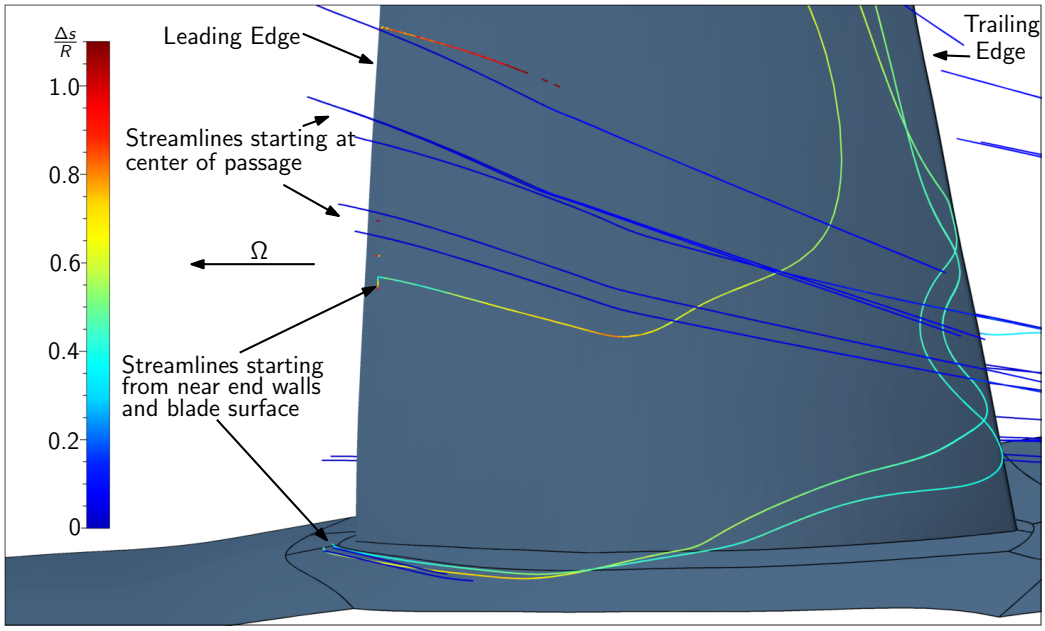

Figure 4-14: Relative streamlines colored by local $\Delta s/R$. Discontinuities in streamlines near trailing edge are a plotting artifact due to periodic boundaries in single passage simulation.

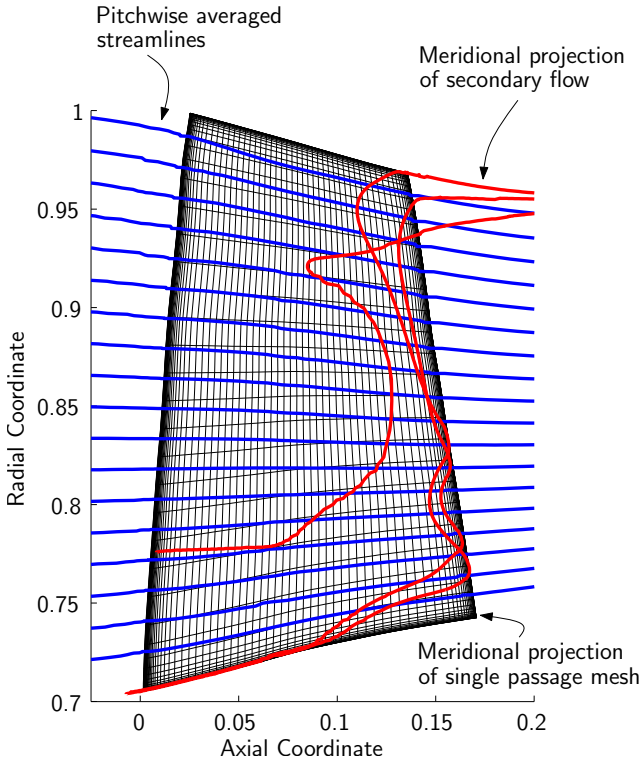

Figure 4-15: Meridional projections of secondary flow and single passage RANS mesh compared to pitchwise averaged streamlines.

the $f_{\mathrm{p,visc}}$ distribution in Fig. 4-16 with a spanwise viscous parallel force profile at the indicated meridional location shown in Fig. 4-17. The $f_{\mathrm{p,visc}}$ distributions show the increase in viscous parallel force due to the mixing out of the tip leakage vortex and end wall boundary losses near the hub.

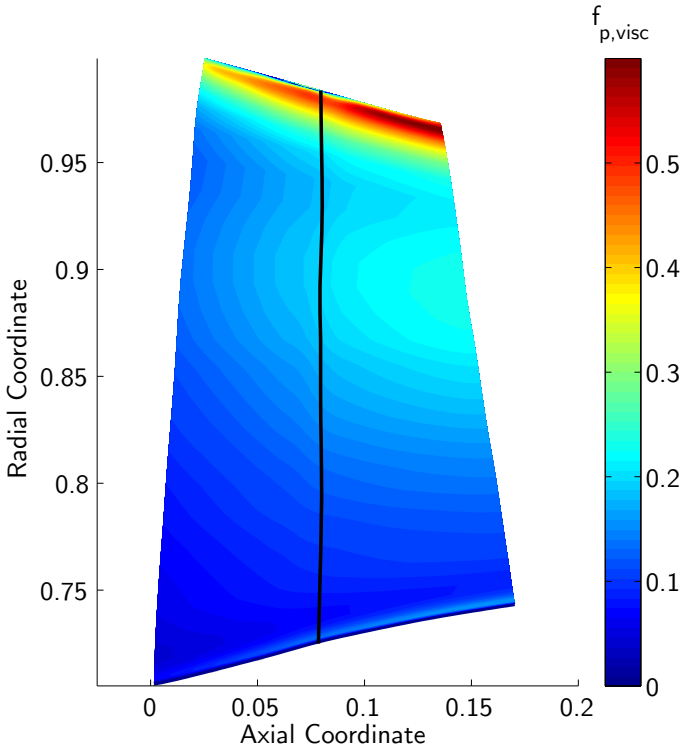

Figure 4-16: Viscous parallel force extracted from single passage RANS simulation. Line indicates cut for Fig. 4-17.

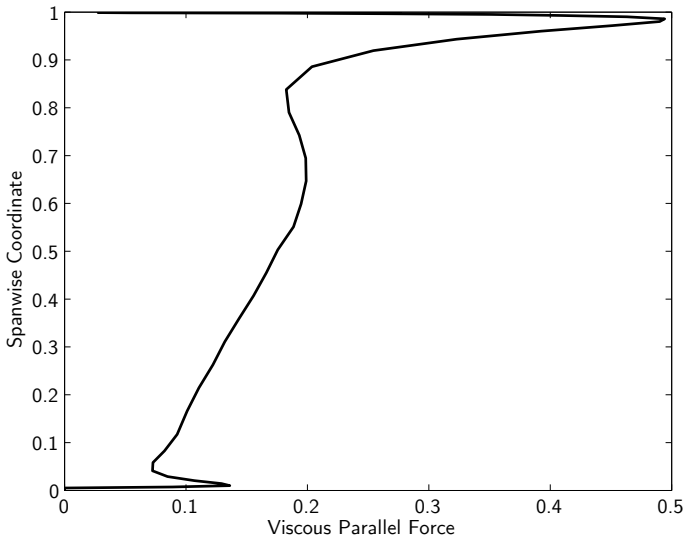

Figure 4-17: Spanwise distribution of viscous parallel force extracted from single passage RANS simulations.

Chapter 5

Validation of Body Force Field Extraction Procedure

5.1 Computational Setup of Body Force Field Simulation - Rotor 37

As noted in Sec. 3.3, the validation of the body force field extraction procedure on Rotor 37 is performed using FINE/Open-OpenLabs. FINE/Open uses a unstructured solver and source terms can be specified through the OpenLabs environment. The mesh for the body force simulation is generated using the Interactive Grid Generation (IGG) tool, also developed by Numeca International. IGG was used to generate a structured grid block for the inlet, outlet, and swept volume of the blade row. Since there is no discrete blade, the generated mesh is less complex and coarser. The meridional view of the mesh generated for the Rotor 37 test case is shown in Fig. 5-1. The IGG mesh was imported into HEXPRESS and converted into an unstructured mesh compatible with the FINE/Open solver. The body force mesh is uniform to avoid numerical dissipation. The mesh can be refined in areas that require higher precision based on the extracted force field distributions, but the mesh shown above was found to be adequate for the validation of the body force field extraction procedure.

A 10 degree sector of the full wheel annulus was generated with a grid node count of

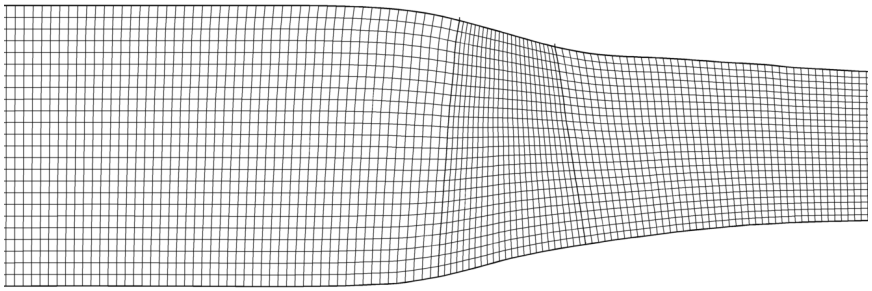

Figure 5-1: Body force simulation mesh for Rotor 37.

approximately 52,000, in contrast to the node count for the single passage RANS mesh of nearly 840,000. Noting that periodic boundary conditions are used, the meridional grid has approximately 3,000 grid points. This order of magnitude reduction in node count translated into an order of magnitude reduction in computational run time from nearly 30 minutes to achieve convergence with the single passage RANS simulation to only 2 minutes for the body force simulation.

The body force simulation used the same inlet conditions as the single passage RANS simulation but used an exit mass flow boundary condition and Euler slip walls. The exit mass flow boundary condition was used to ensure the operating condition was matched to the single passage RANS simulations from which the body force field was extracted. Euler slip walls were used to avoid double bookkeeping the entropy rise on the end walls since the viscous parallel force extraction methodology includes the end wall entropy rise.

5.2 Validation of Normal Force and Viscous Parallel Force Implementation

The extraction of the blade geometry and forces from the single passage RANS simulations and the generation of the source term file are verified by prescribing the blade metal blockage, the normal force, and viscous parallel distributions for the Rotor 37.

5.2.1 Two Dimensional Polynomial Fitting of Force Field Distributions

Due to limitations in the OpenLabs environment noted in Sec. 3.3, two dimensional polynomials, as functions of x and r, of the normal force, viscous parallel force, and blade metal blockage were used to prescribe the distributions. The polynomial coefficients were computed through a least squares fitting process. The fit for a variable A is computed by,

$$A \approx A^* = \sum_{m=0}^{M} \sum_{n=0}^{N} a_{mn} x^m r^n \ , \tag{5.1}$$

where A^* is the fit for the original distribution A, M and N are the maximum orders of the polynomials in x and r respectively. Quantification of the error between the two dimensional fits and extracted data is computed by,

$$\text{Error} = \frac{A^* - A}{A} \ . \tag{5.2}$$

An error value of 0.5 corresponds to a 50% error relative to the extracted value[1].

Normal Force

Figures 5-2 and 5-3 show the fitted distribution for the normal force based on the distribution in Fig. 4-11 and the relative error computed by Eq. 5.2, respectively. A fifth-order polynomial in the chordwise direction and a linear fit in the spanwise

[1]This definition of relative error is used throughout this thesis.

direction were used to represent $f_{\text{n,turn}}$. The orders of the polynomial fits were chosen by inspection to minimize the error distribution.

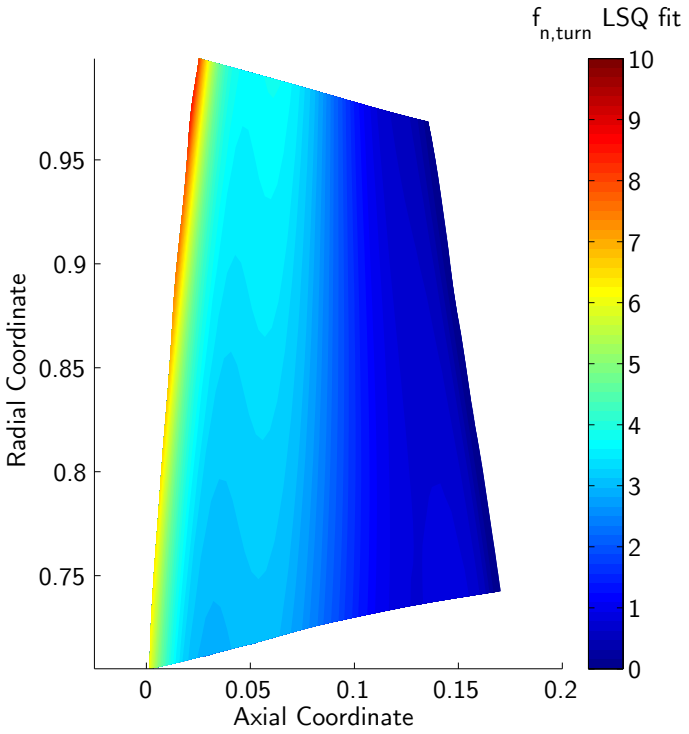

Figure 5-2: LSQ fit of normal force distribution of axial test case.

The appearance of a region of large relative error in the normal force fitting procedure at the trailing edge near the hub is due to the near zero value of the normal force in that region. This is examined in greater detail in Fig. 5-4 which shows the original and fitted $f_{\text{n,turn}}$ meridional distributions and the relative error along the line in Fig. 5-3.

Viscous Parallel Force

Figures 5-5 and 5-6 show the fitted distribution and relative error for the viscous parallel force distribution in Fig. 4-16 respectively. Using a similar process as for fitting $f_{\text{n,turn}}$, a fourth-order polynomial in the chordwise direction and a ninth-order polynomial in the spanwise direction were used. The high polynomial order in the spanwise direction is a result of the sharp increase in the force at the shroud due to

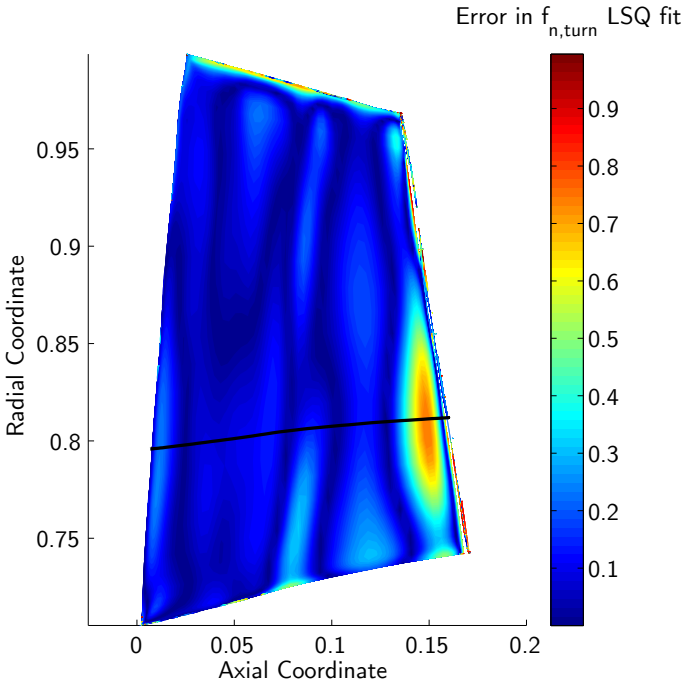

Figure 5-3: Relative error of LSQ fit of normal force distribution. Region of large error due to low value of $f_{\mathrm{n,turn}}$. Line indicates cut for Fig. 5-4.

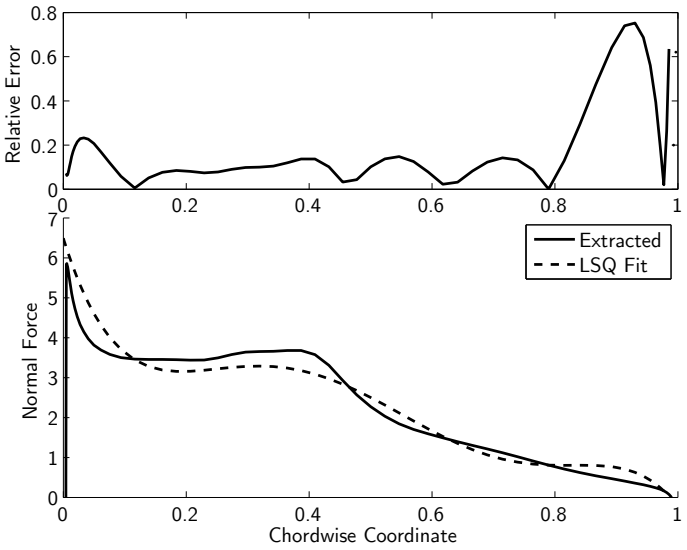

Figure 5-4: Error in LSQ fit of normal force is large when extracted value is small.

mixing of the tip leakage vortex.

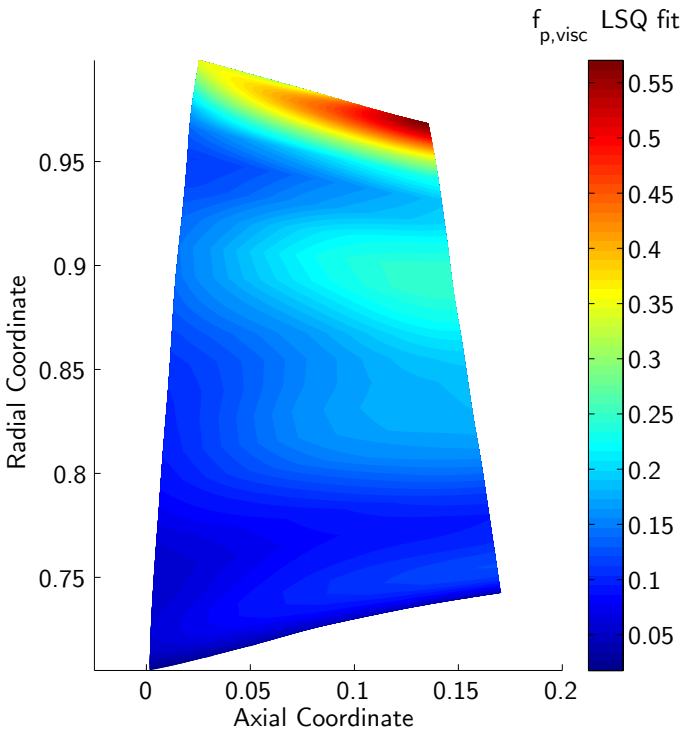

Figure 5-5: LSQ fit of $f_{\mathrm{p,visc}}$ distribution of axial test case.

The large relative error in the reconstruction of $f_{\mathrm{p,visc}}$ near the hub is due to the small value of $f_{\mathrm{p,visc}}$ in that region. Figure 5-7 shows the spanwise distribution of the extracted and fit the viscous parallel force along the line in Fig. 5-6. The large relative error near the hub is due to the small value of $f_{\mathrm{p,visc}}$ and the ripples in the reconstruction are due to the high order order for the spanwise polynomial. Alternative methods of curve fitting should be investigated in order to capture sharp increases in distributions without introducing spurious and non-physical fitting artifacts.

Blade Metal Blockage

The reconstruction and relative error based on the b distribution depicted in Fig. 4-8 is shown in Figs. 5-8 and 5-9 respectively. The polynomial fit for b uses a third-order fit in both the chordwise and the spanwise directions and is in good agreement with relative errors of the order of $\pm 2\%$.

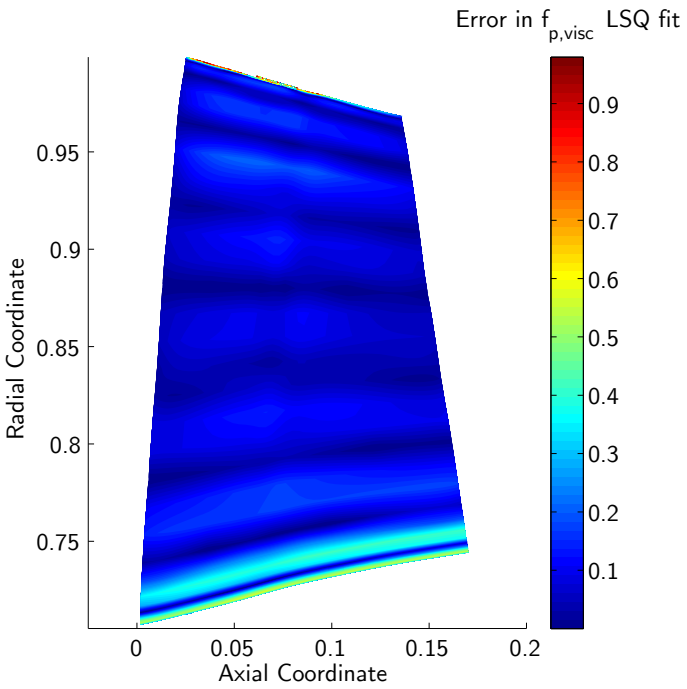

Figure 5-6: Normalized error of LSQ fit of $f_{\mathrm{p,visc}}$ distribution. Region of large error due to low value of $f_{\mathrm{p,visc}}$. Line indicates cut for Fig. 5-7.

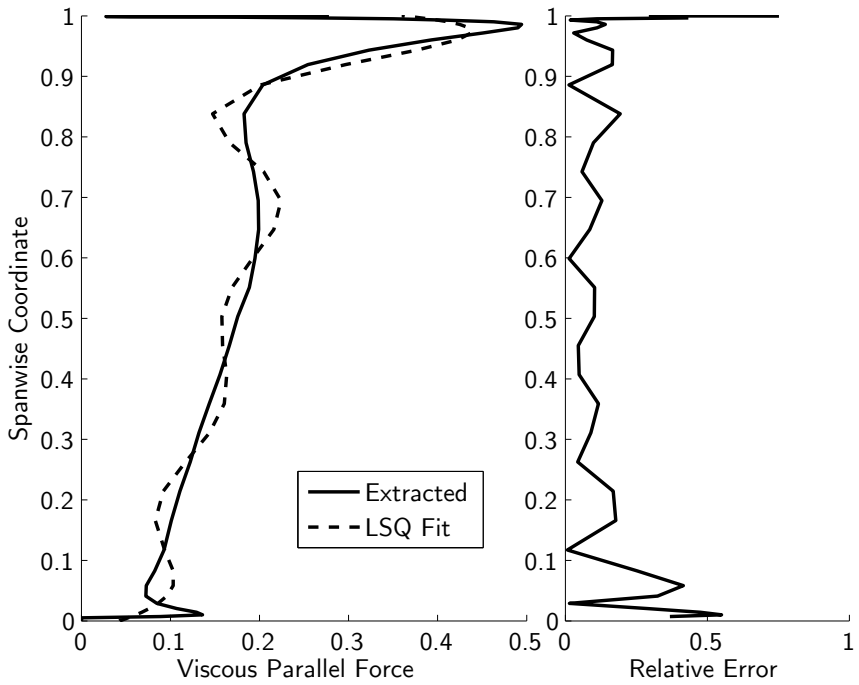

Figure 5-7: Error in LSQ fit of viscous parallel force can be large when extracted value is small. Ripples in LSQ fit due to polynomial nature of fit.

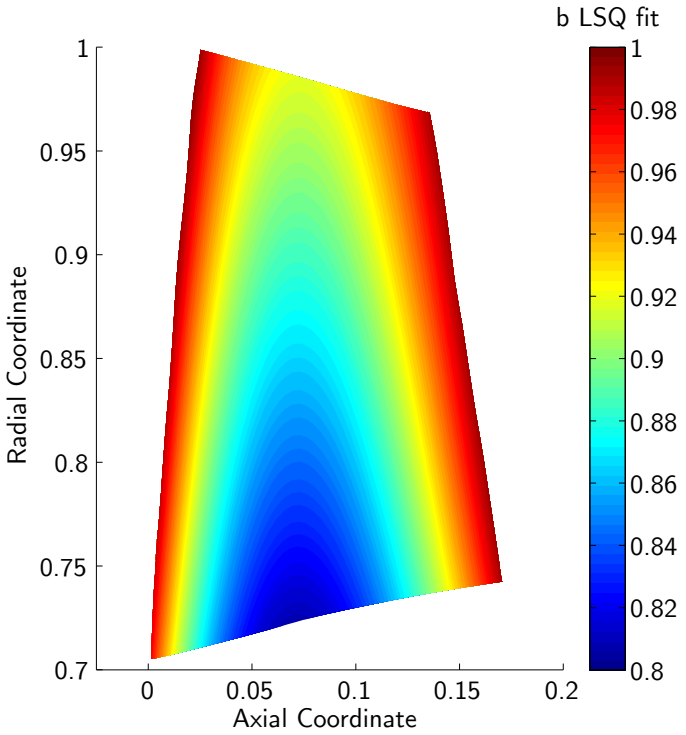

Figure 5-8: Fitting of Rotor 37 blade metal blockage parameter.

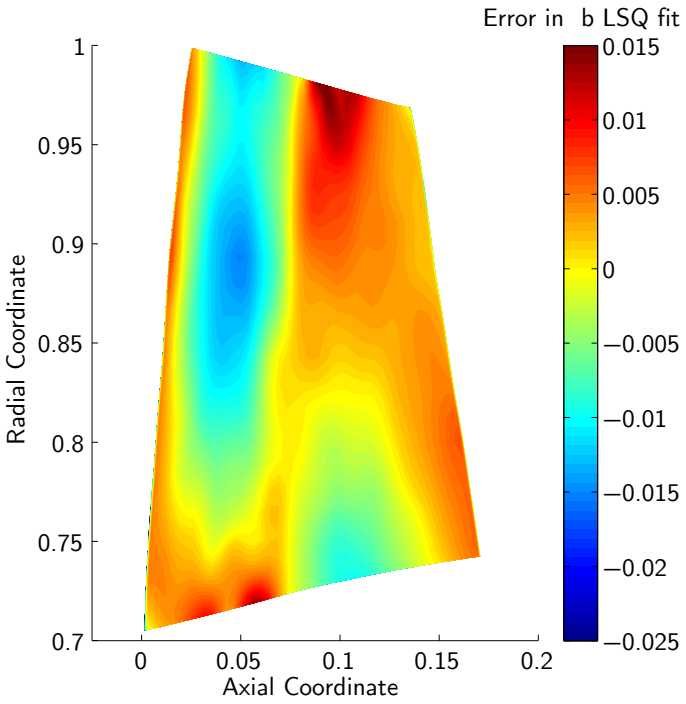

Figure 5-9: Relative error in fitting of blade metal blockage parameter.

5.2.2 Flow Field from a Simulation with a Prescribed Body Force Field

The distributions in Figs. 5-2, 5-5, and 5-8 are prescribed for an axisymmetric body force simulation. The midspan relative Mach number distribution through the rotor is shown in Fig. 5-10.

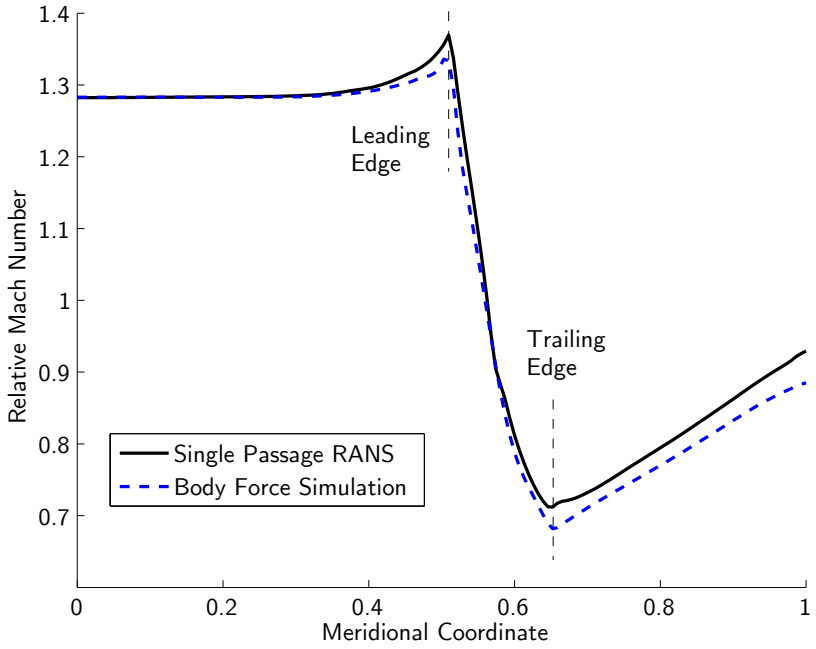

Figure 5-10: Relative Mach number comparison between single passage RANS and body force simulation at midspan.

The spanwise profiles of stage loading coefficient, total-to-total pressure rise coefficient, total-to-static pressure rise coefficient, and polytropic efficiency are shown in Figs. 5-11, 5-12, 5-13, and 5-14, respectively.

The differences between the profiles stem from the prescribed body force distributions. Capturing the end wall distributions using polynomials is challenging and a better fitting procedure or an ability to specify a distribution that can be interpolated by the solver should be able to capture the end wall effects. While the overall turning and losses are in agreement there is a 6% over prediction in total-to-static pressure coefficient. The over prediction of static pressure rise is consistent with

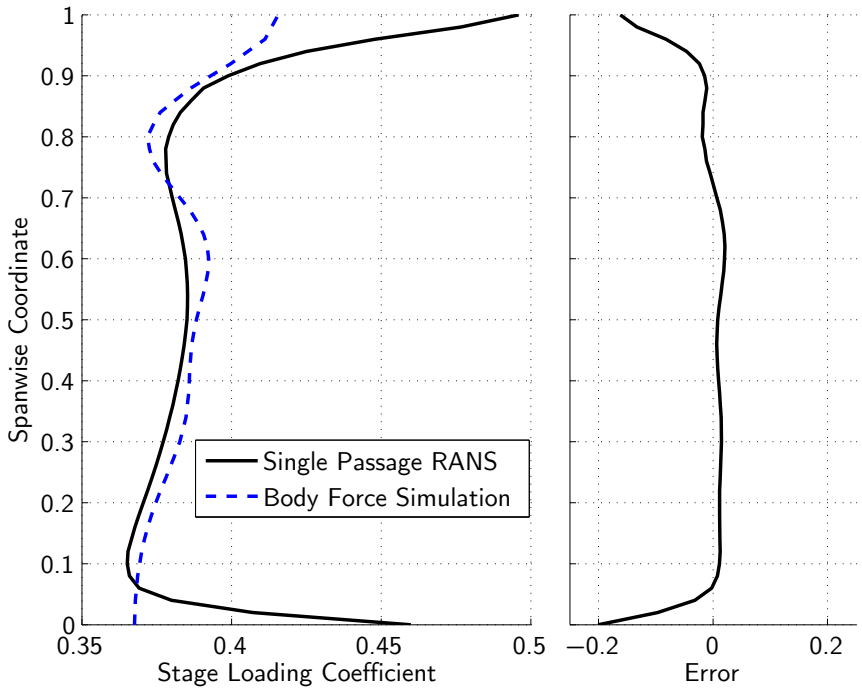

Figure 5-11: Stage loading coefficient comparison between single passage RANS and body force simulation at rotor exit.

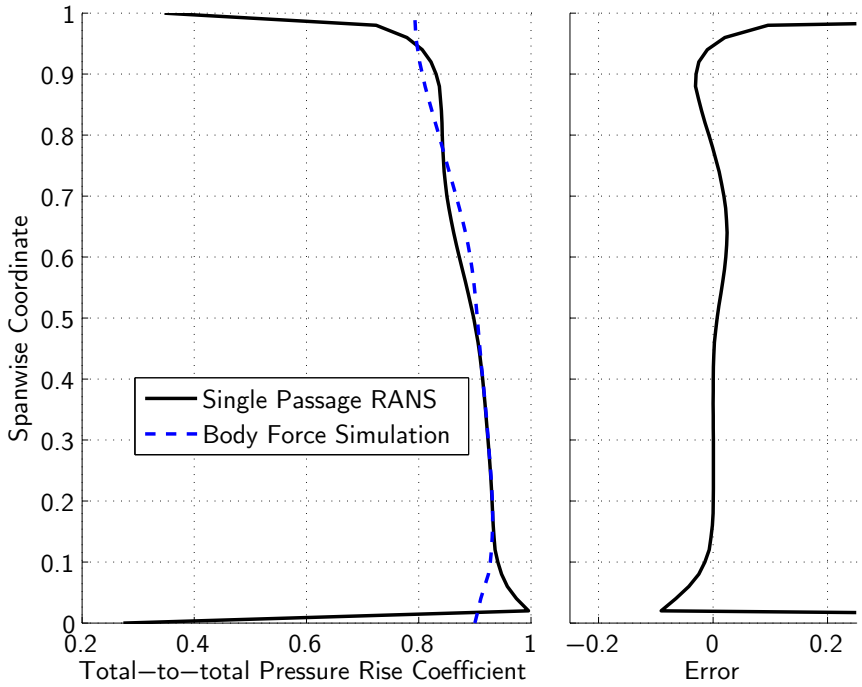

Figure 5-12: Total-to-total pressure rise coefficient comparison between single passage RANS and body force simulation at rotor exit.

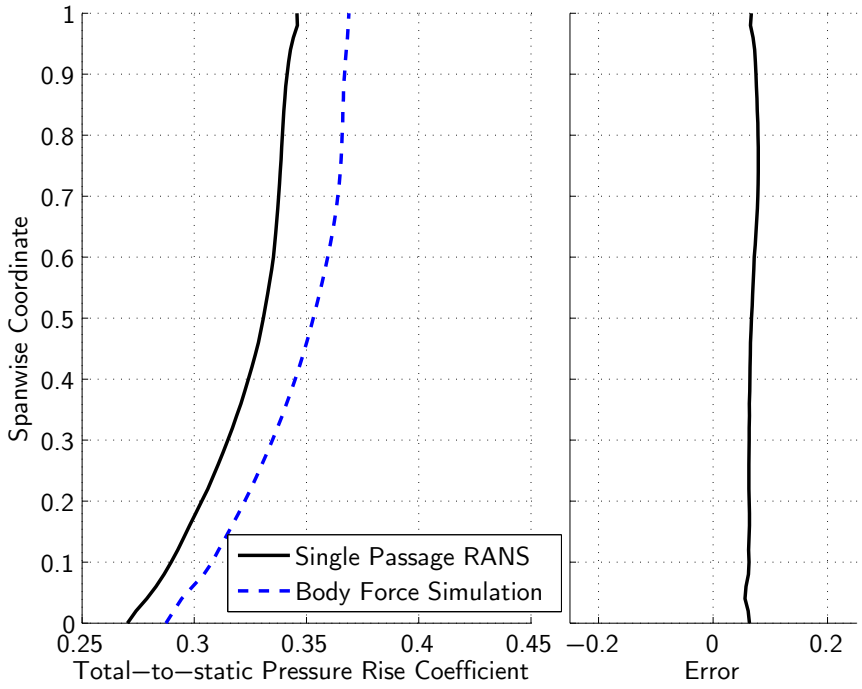

Figure 5-13: Total-to-static pressure rise coefficient comparison between single passage RANS and body force simulation at rotor exit.

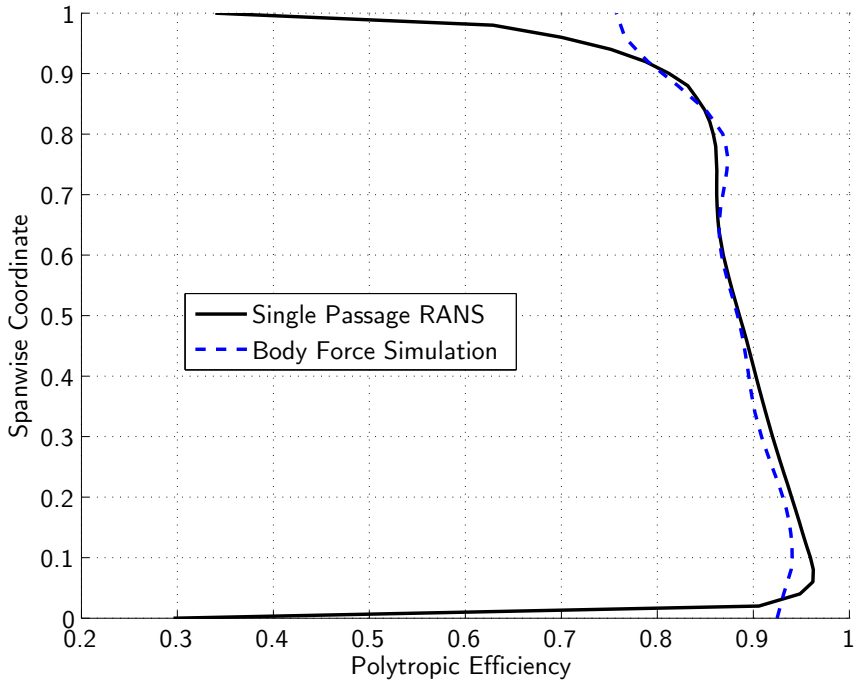

Figure 5-14: Polytropic efficiency comparison between single passage RANS and body force simulation at rotor exit.

the over prediction of the diffusion of relative Mach number and suggests that some flow acceleration effects are not captured. Considering the verification of the blade metal blockage source term model and implementation in the next section, the flow accelerations within the blade passage that are not captured are due to aerodynamic blockage and to upstream influence. This is consistent with the assumptions made for the blade passage model derivation.

5.3 Verification of Blade Metal Blockage Model Implementation

The blade metal blockage model is based only on geometry and requires no empirical inputs. A preliminary verification of the blade metal blockage model was made prior to the validation of the full blade passage model. This verification is performed using two test cases, a two dimensional airfoil in a channel and a three dimensional strut in an annulus. Test case calculations were performed with subsonic and transonic inflows, similar to the conditions experienced in a high pressure ratio centrifugal compressor.

5.3.1 Two-Dimensional Airfoil in a Straight Channel

The airfoil for the two dimensional test case was defined by a symmetric quadratic thickness distribution given by,

$$t(x) = t_0 \left[1 - 4 \left(\frac{x - \left(\frac{x_{le} + x_{te}}{2} \right)}{x_{te} - x_{le}} \right)^2 \right] , \tag{5.3}$$

where t is the blade thickness, and x_{le} and x_{te} are the locations of the airfoil leading and trailing edges respectively. The thickness distribution is derived so the airfoil has a specified thickness, t_0, at the mid chord location and zero thickness at the leading and trailing edges. Figure 5-15 shows the test case geometry where the dimensions

are normalized by the blade chord.

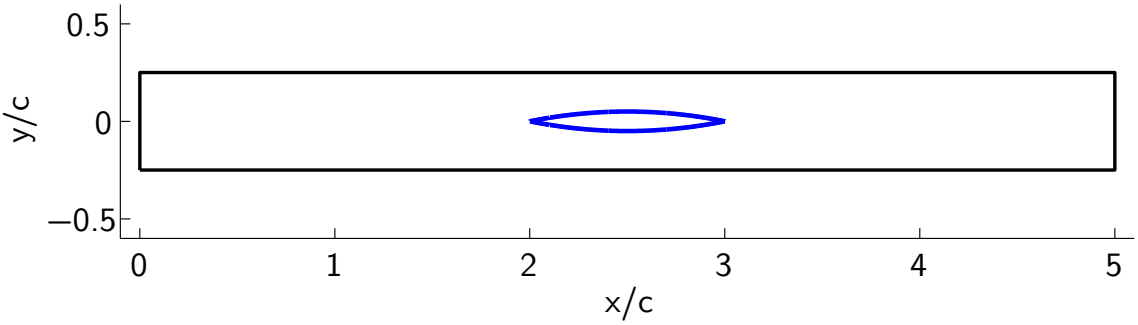

Figure 5-15: Geometry of two dimensional blade metal blockage validation test case.

The simulation of the single airfoil was carried out as an Euler calculation to avoid any boundary layer effects. The symmetric airfoil does not introduce flow turning so that $f_{\text{n,turn}} = 0$ and $f_{\text{p,visc}} = 0$. These conditions isolate the modeling of the blade metal blockage. Given this thickness distribution, the blockage distribution illustrated in Fig. 5-16 was used with the blade metal blockage model in Eqs. 3.24, 3.25, and 3.26 and implemented as an empty channel with source terms in FINE/Open-OpenLabs.

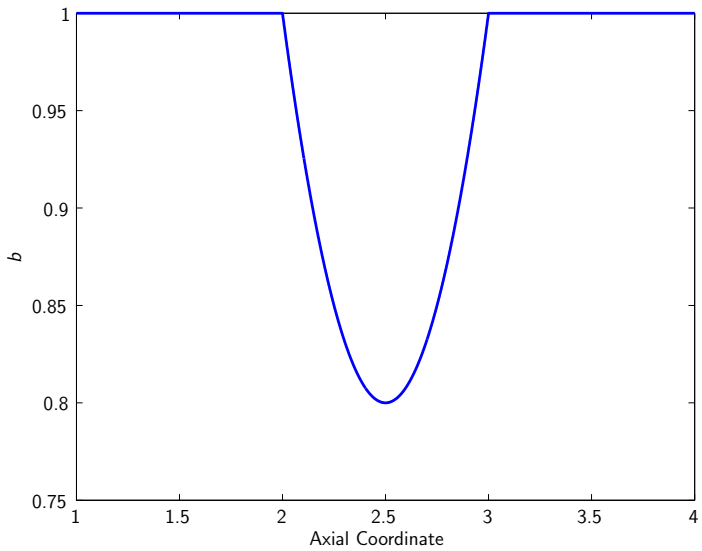

Figure 5-16: Blockage distribution of two dimensional blade metal blockage validation test case.

The mass averaged Mach number and static pressure distributions for the single

airfoil simulation and the corresponding body force simulation with subsonic and transonic inflow conditions are shown in Figs. 5-17 and 5-18. The Mach number distribution in Fig. 5-19 shows good agreement in capturing the location and strength of the shock. The flow displacement due to the blade is captured in both the subsonic and transonic inflow cases.

5.3.2 Three-Dimensional Strut in Annulus

The three dimensional test case for the blockage model is a constant thickness strut within an annulus. The isometric view of the strut geometry and the blockage distribution are shown in Fig. 5-20.

Figure 5-21 shows the Mach number distribution between the pitchwise averaged discrete Euler single passage flow field and the body force flow field for subsonic inflow. Figures 5-22 through 5-24 show the Mach number distributions at spanwise locations near the hub, midspan, and shroud. Similarly, Fig. 5-25 shows the comparison of Mach number distribution and Figs. 5-26 through 5-28 show the axial distributions are various spanwise cuts for the transonic inflow case. The dash-dot lines in all plots indicate the leading and trailing edge of the strut.

The results show agreement in the Mach number and static pressure distributions between the body force simulation and the Euler simulation. The maximum error in pitchwise averaged Mach number is 3.5% at mid chord near the shroud and reduces to 3% near the hub. The discrepancies in the extent of upstream influence of the strut are because the axisymmetric flow field description developed from the body force field does not have a circumferential length scale to create upstream influence [19].

The transonic body force simulations show agreement with the single passage simulations. There is a 7% error in the maximum Mach number in the passage and the location of the shock is in agreement. The error in maximum Mach number can be addressed through grid resolution in the vicinity of the shock. Similar to the subsonic simulations, the upstream influence due to the lack of a circumferential length scale is not captured because of the axisymmetric nature of the flow field.

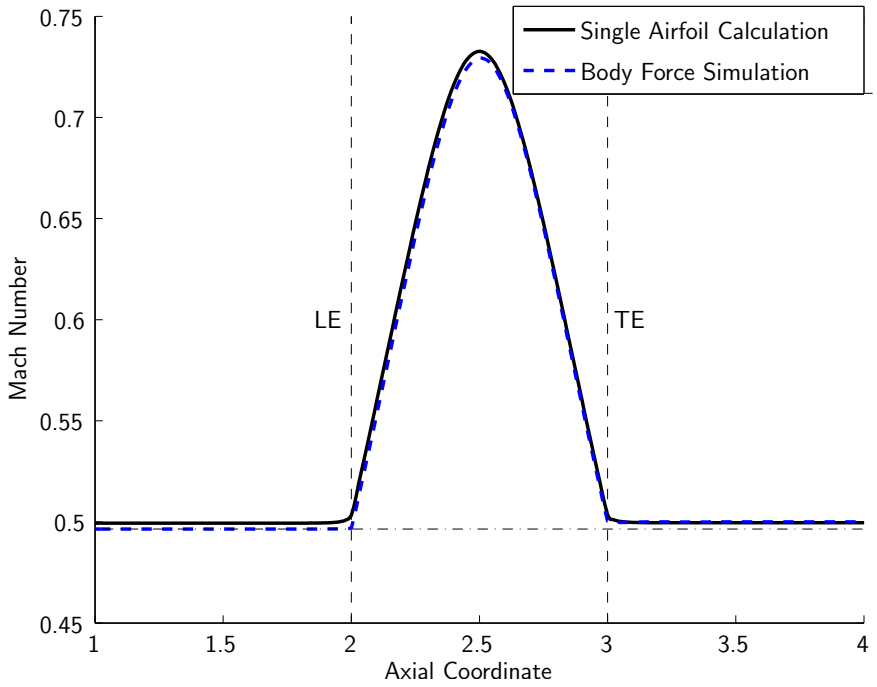

(a) Mach number

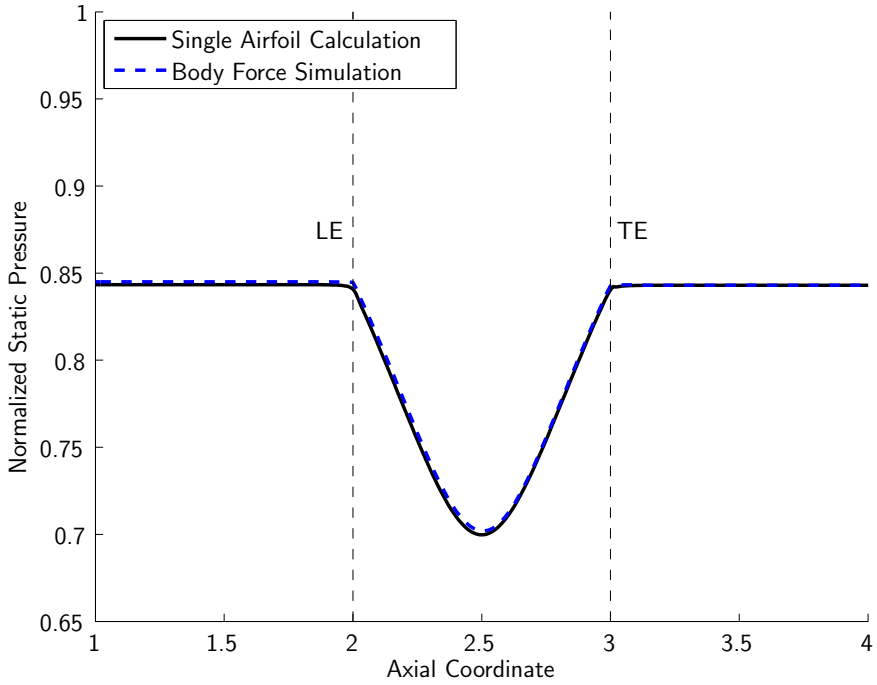

(b) Static pressure non-dimensionalized by inlet total pressure

Figure 5-17: Flow field distributions for mass-averaged discrete blade and body force simulations with subsonic inflow.

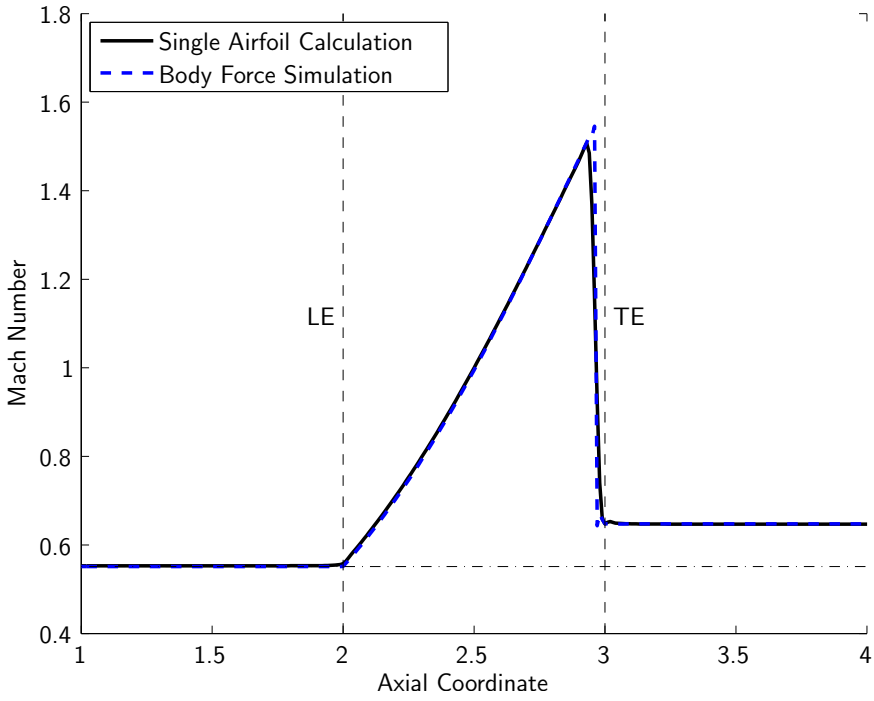

(a) Mach number

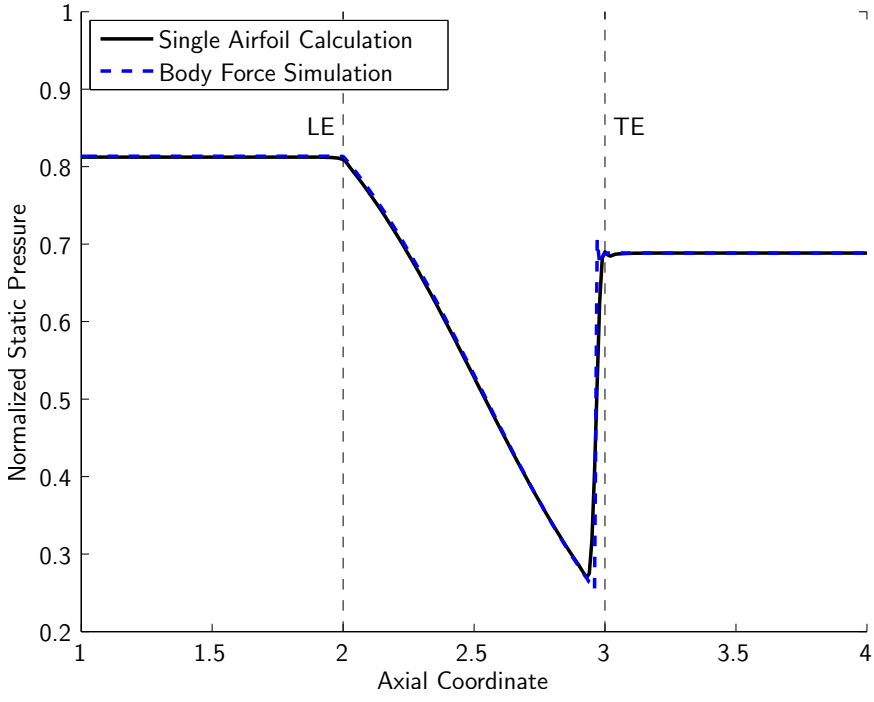

(b) Static pressure non-dimensionalized by inlet total pressure

Figure 5-18: Flow field distributions for mass-averaged discrete blade and body force simulations with transonic inflow.

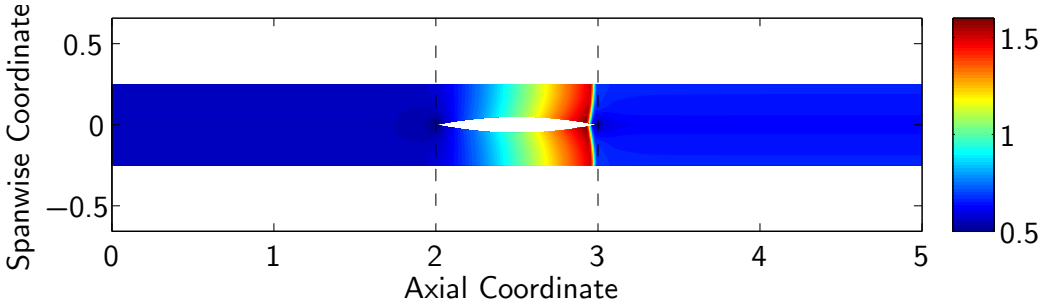

(a) Single airfoil calculation

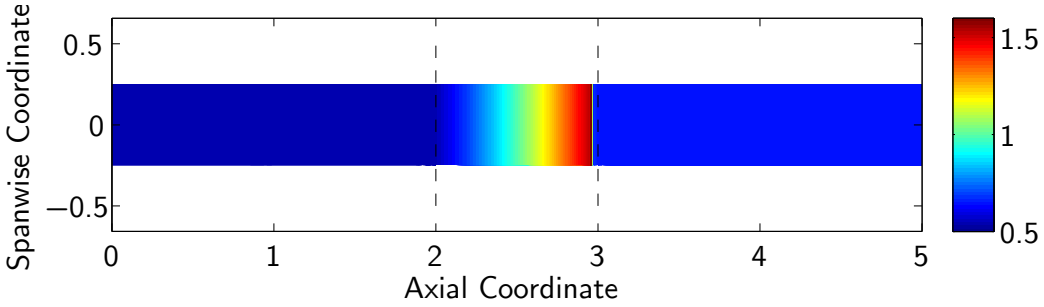

(b) Body force simulation

Figure 5-19: Mach number distribution for transonic inflow.

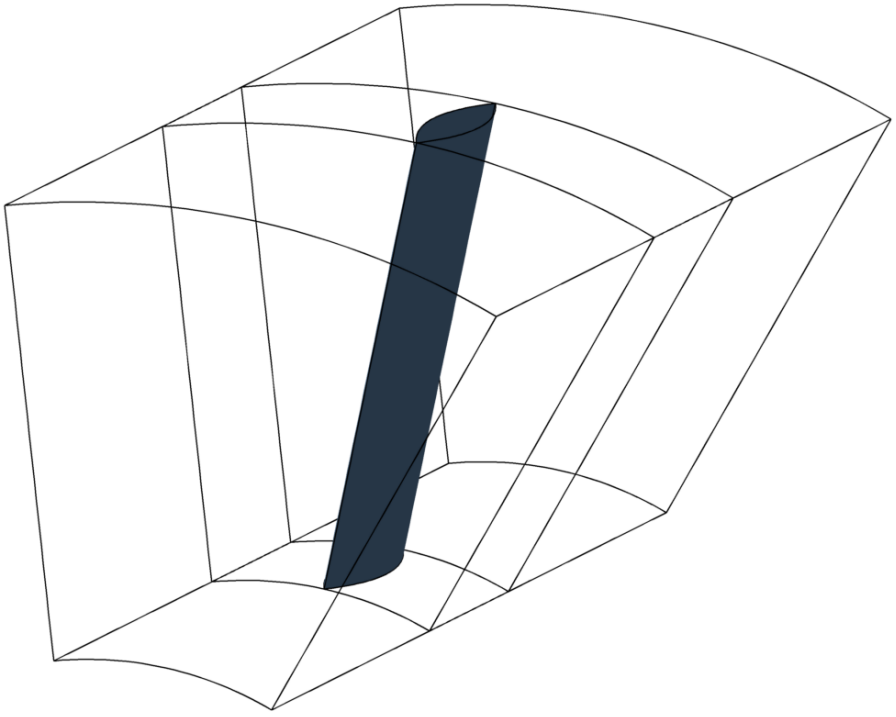

(a) Isometric view of domain

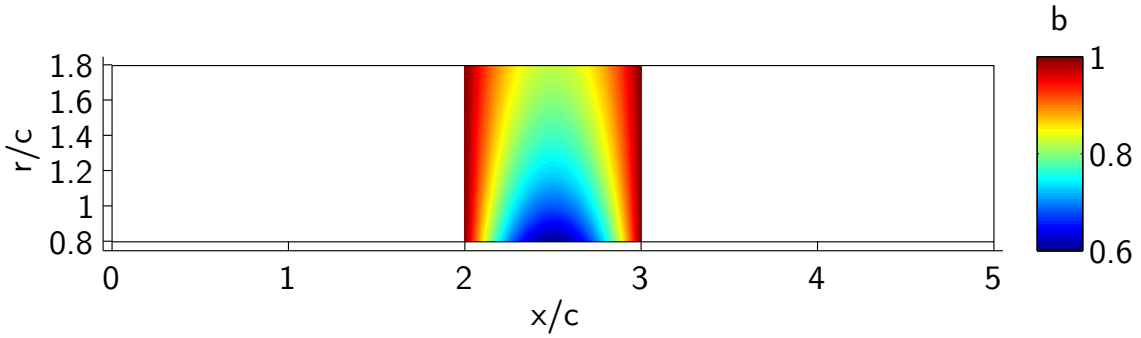

(b) Distribution of b

Figure 5-20: Geometry of three-dimensional blade metal blockage model validation test case.

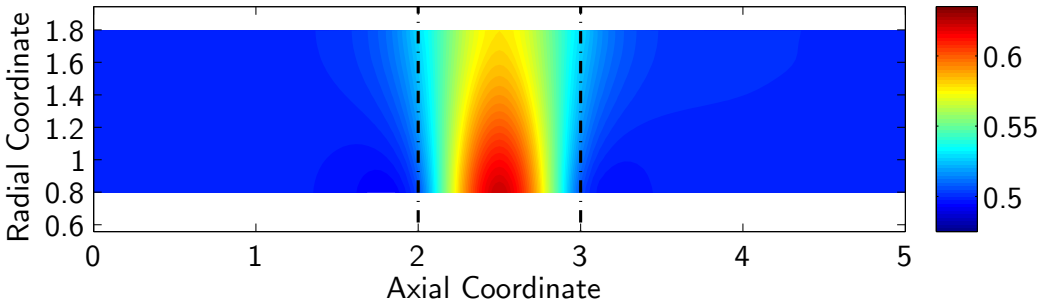

(a) Pitchwise average of single passage Euler simulation

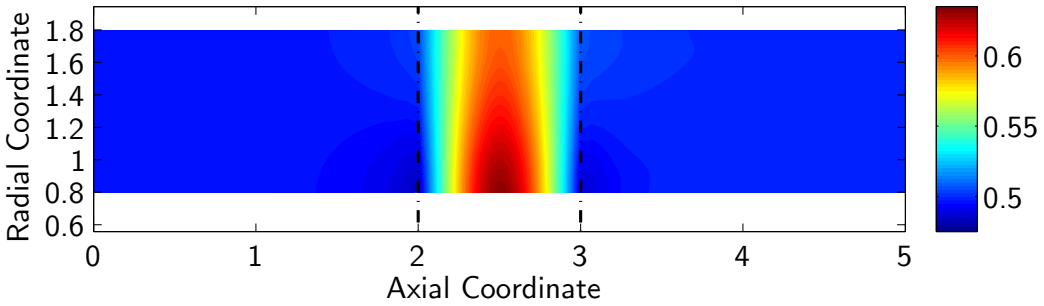

(b) Body force simulation

Figure 5-21: Mach number distribution for subsonic inflow.

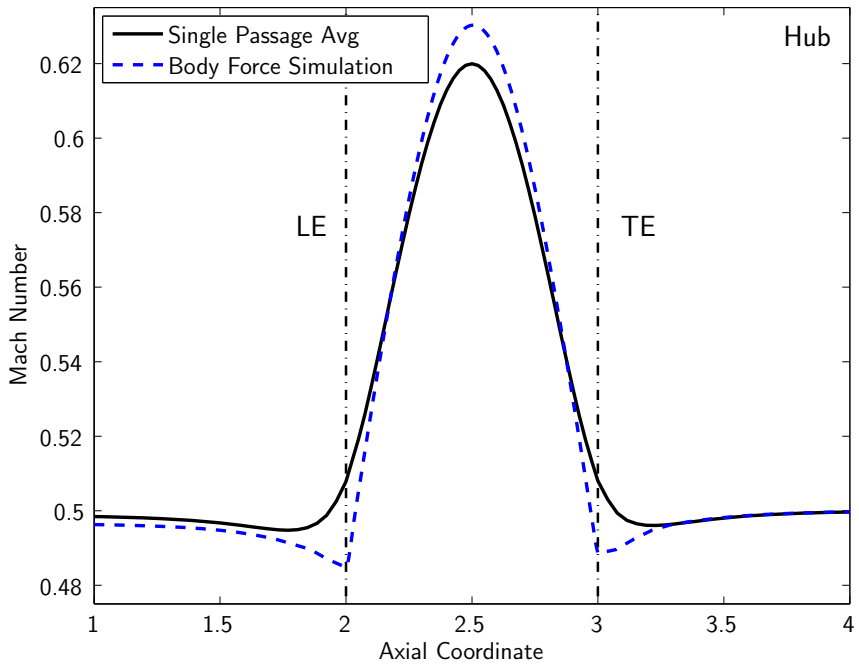

Figure 5-22: Mach number distribution near hub for subsonic inflow.

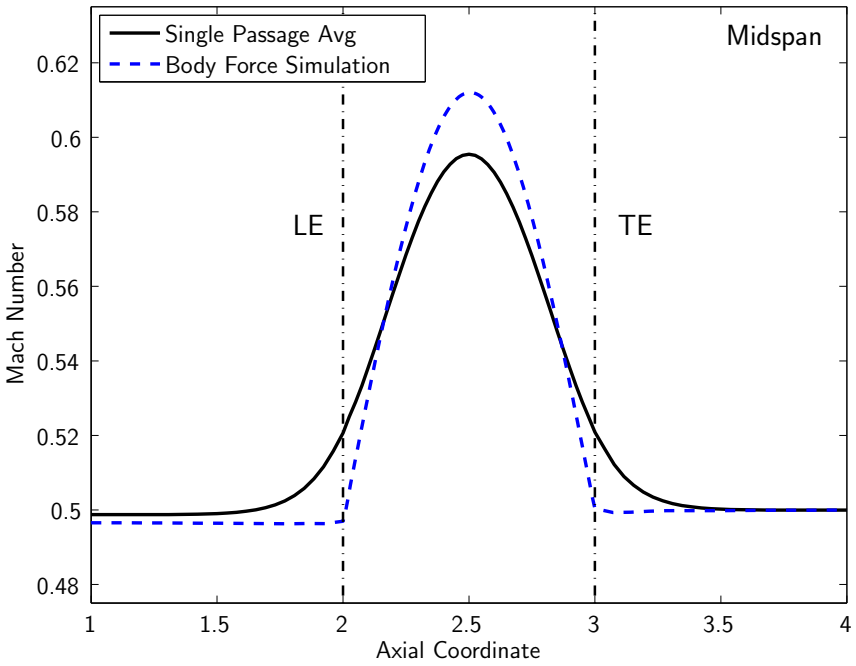

Figure 5-23: Mach number distribution at midspan for subsonic inflow.

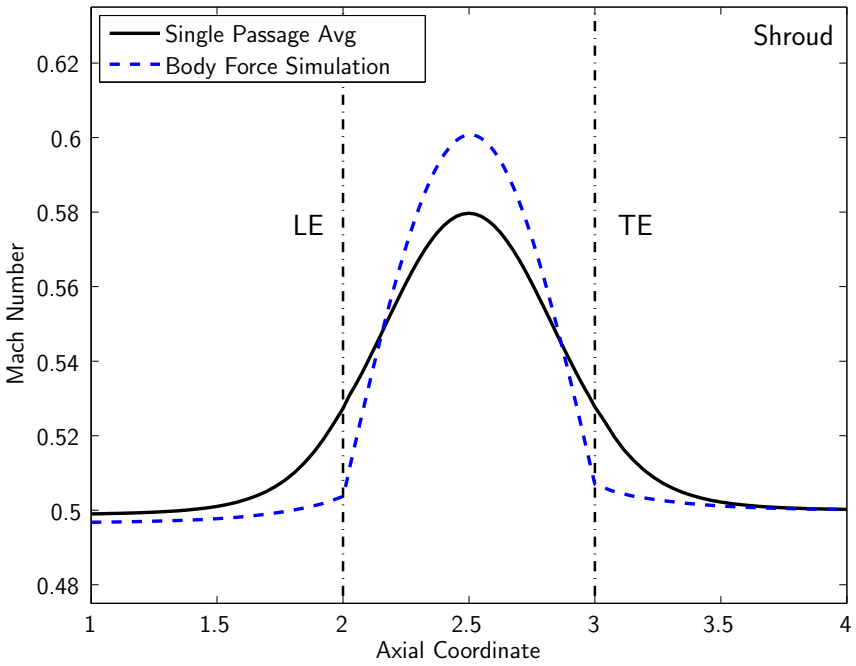

Figure 5-24: Mach number distribution near shroud for subsonic inflow.

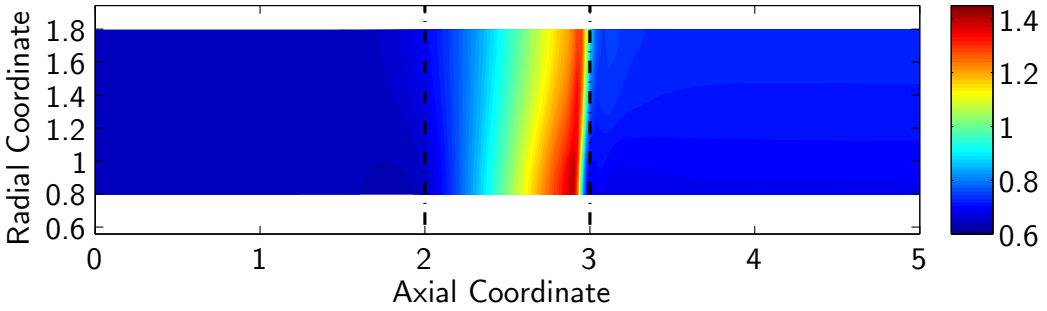

(a) Pitchwise average of single passage Euler simulation

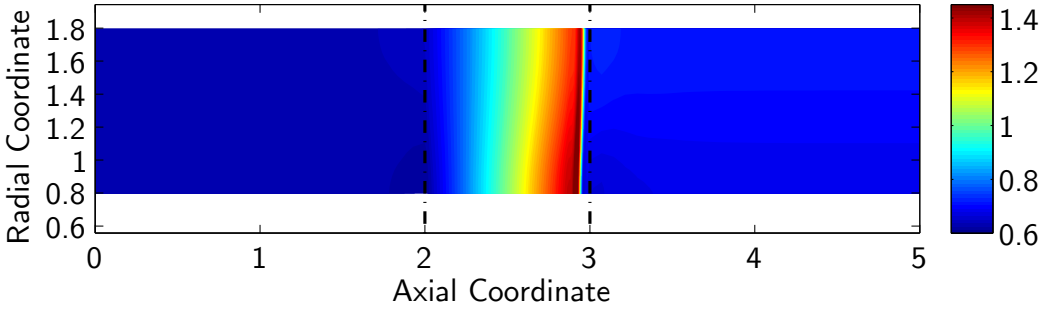

(b) Body force simulation

Figure 5-25: Mach number distribution for transonic inflow.

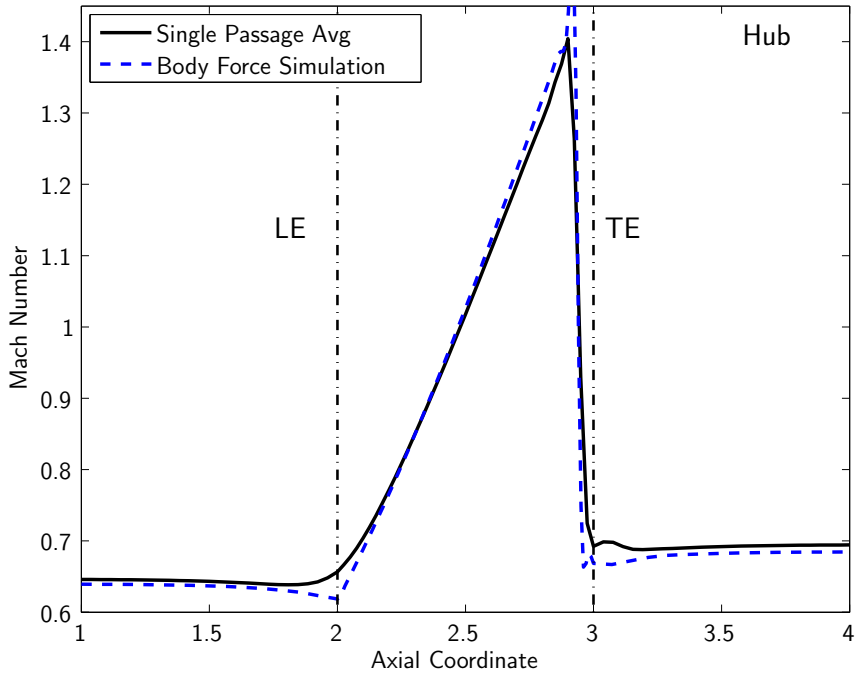

Figure 5-26: Mach number distribution near hub for transonic inflow.

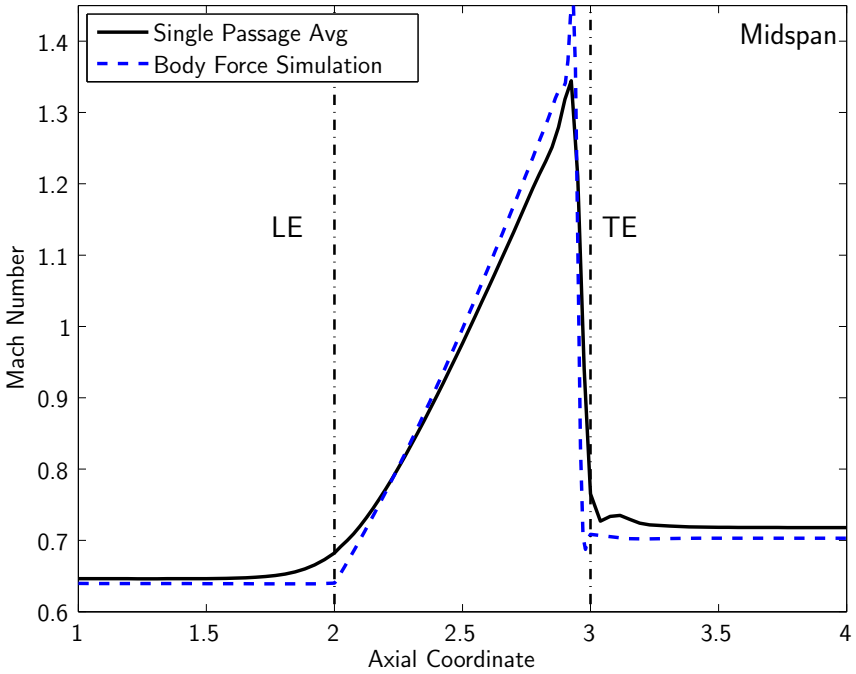

Figure 5-27: Mach number distribution at midspan for transonic inflow.

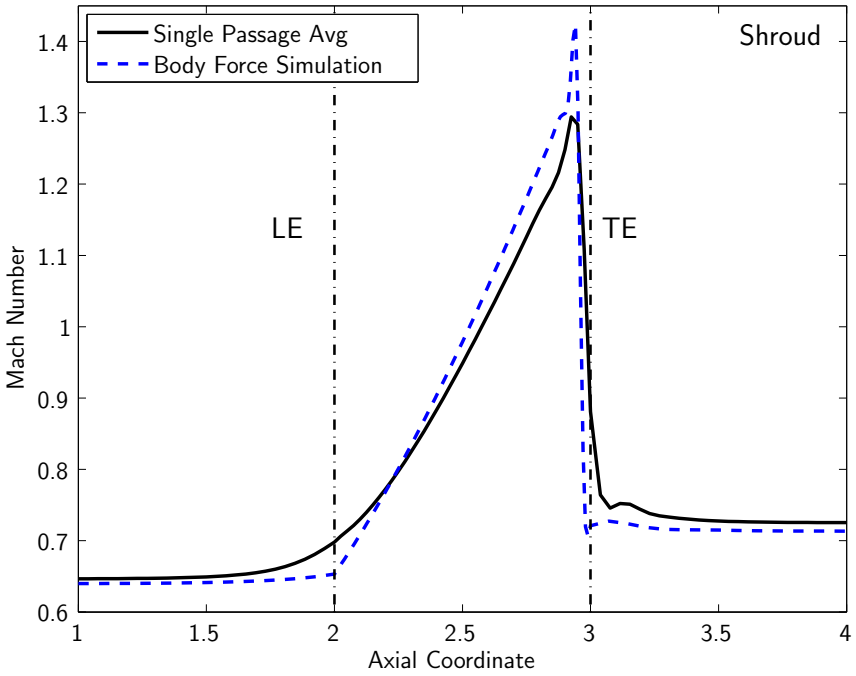

Figure 5-28: Mach number distribution near shroud for transonic inflow.

Chapter 6

Validation of Blade Passage Model for a Radial Impeller

The blade passage model is validated for a transonic radial impeller with prismatic blades. The geometry of the impeller is shown in Fig. 6-1 and summarized in Tab. 6.1.

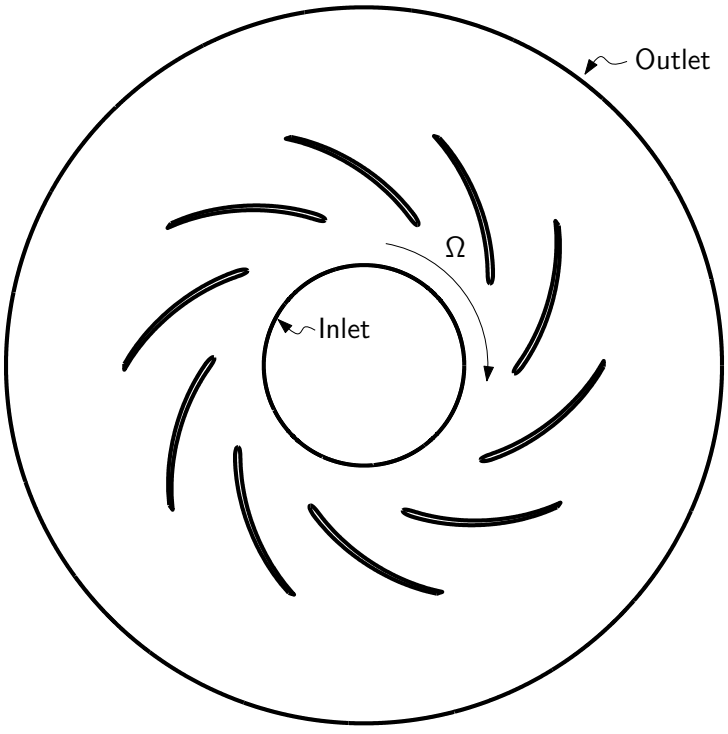

Figure 6-1: Geometry of prismatic radial impeller.

Table 6.1: Radial impeller data.

r_{LE} to r_{TE} Ratio	0.626
Tip Mach Number, M_{u2}	0.792
Design Total Pressure Ratio	1.5
Trailing Edge Backsweep, κ_2	60°
Blade Count, N_B	10
Blade Reynolds Number, Re	$\approx 10^6$

6.1 Computational Setup of Single Passage RANS Simulations - Radial Impeller

FINE/Turbo is used for the single passage RANS simulations of the radial impeller, as noted in Sec. 3.3. The mesh used is shown in Fig. 6-2 and had a node count of approximately 100,000.

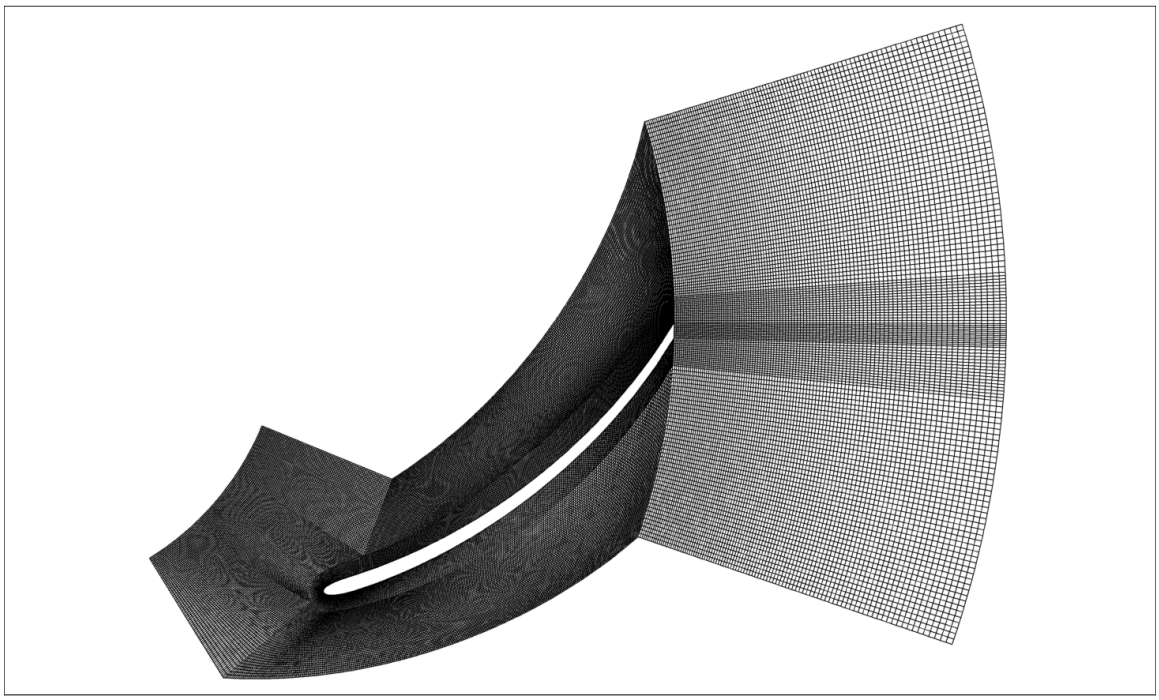

Figure 6-2: Radial impeller single passage RANS mesh.

The single passage RANS calculations are set up as two dimensional where the span is one cell deep. The Spalart-Almaras turbulence model was used and a combi-

nation of exit static pressure and mass flow boundary conditions were used to simulate operating points along the speedline. The mass flow boundary condition was used to obtain convergence of simulations at mass flows below the design mass flow where the exit static pressure boundary condition becomes unstable [20].

6.2 Extracted Body Force Field

The extracted normal force and viscous parallel force for operating points near stall, near peak efficiency, and near choke are shown in Figs. 6-3(a) and 6-3(b), respectively. The abscissa in both figures is the radial distance nond-imensionalized by the impeller tip radius, r_2. The ordinate is the respective body force component, non-dimensionalized by the centrifugal acceleration at the impeller exit radius, $\Omega^2 r_2$.

The normal force distribution exhibits a sharp change near the leading edge, whose magnitude depends on operating condition and is indicative of the changing incidence along the speedline. The magnitude is governed by the flow turning, as shown in Figs. 6-4(a) to 6-4(c), which show the relative Mach number contours and relative streamlines for operating points near stall and near choke, respectively.

At low flow coefficients, the leading edge incidence is higher which results in more flow curvature around the leading edge. The higher curvature at the leading edge increases the magnitude of the normal force due to the lower static pressure value on the suction side of the blade and creates a stronger shock. The normal force loading distribution decreases towards the trailing edge, where the magnitude is similar across operating points. Finally, the value of the normal force goes to near zero at the trailing edge due to the Kutta condition. The sharp drop in force at the trailing edge is due to the blunt trailing edge.

The viscous parallel force distribution, at each operating point, shows a nearly constant value until the blade mid chord where the magnitude starts to decrease. The extraction procedure described in Chap. 4 computes $f_{\mathrm{p,visc}} = T\,(\Delta s/\Delta m)\cos\beta$, where $\Delta s/\Delta m$ is the leading edge to trailing edge entropy gradient and the shape of the distribution of $f_{\mathrm{p,visc}}$ is determined by $\cos\beta$. The overall magnitude of $f_{\mathrm{p,visc}}$ is

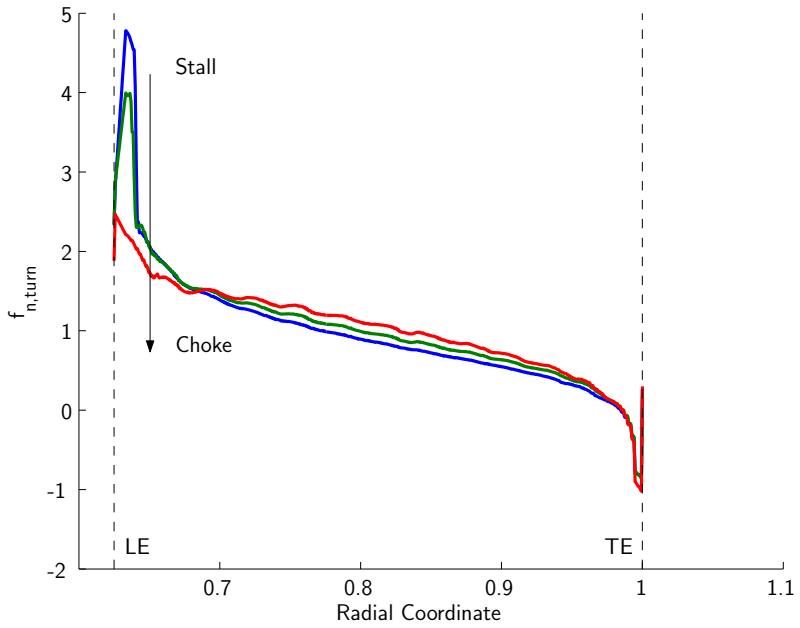

(a) Normal force

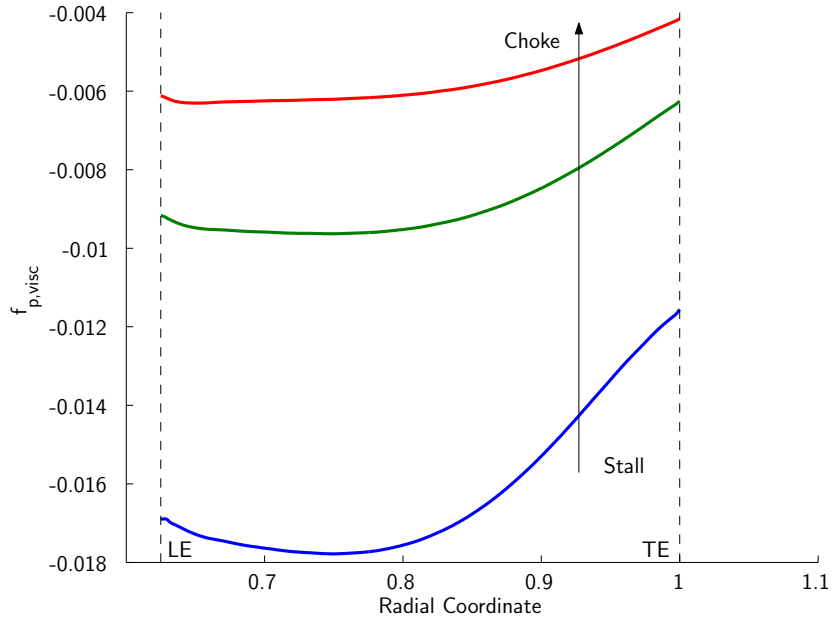

(b) Viscous parallel force

Figure 6-3: Force field extracted from single passage RANS simulations. Forces are non-dimensionalized by centrifugal acceleration at the impeller exit radius.

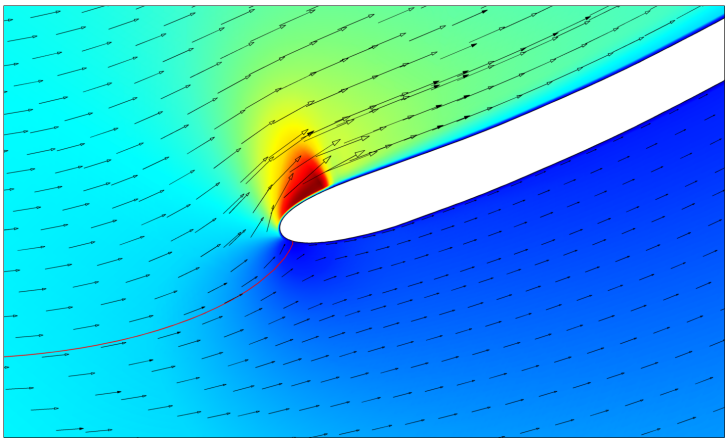

(a) Near stall

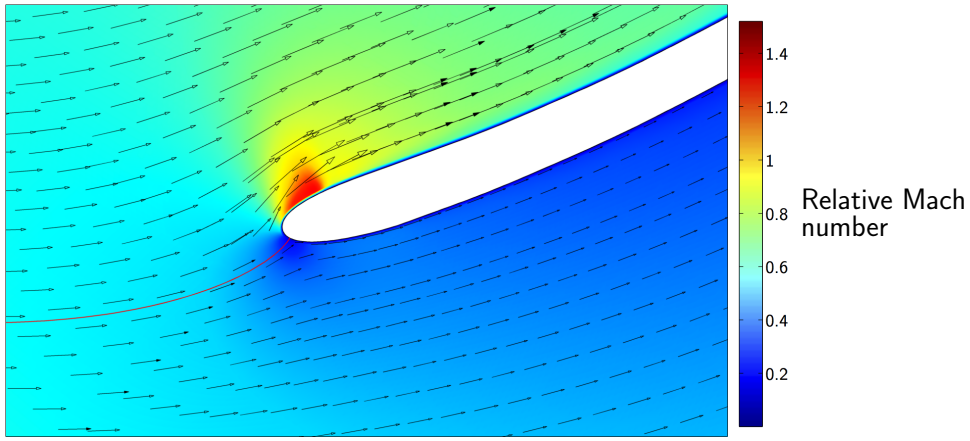

(b) Near design

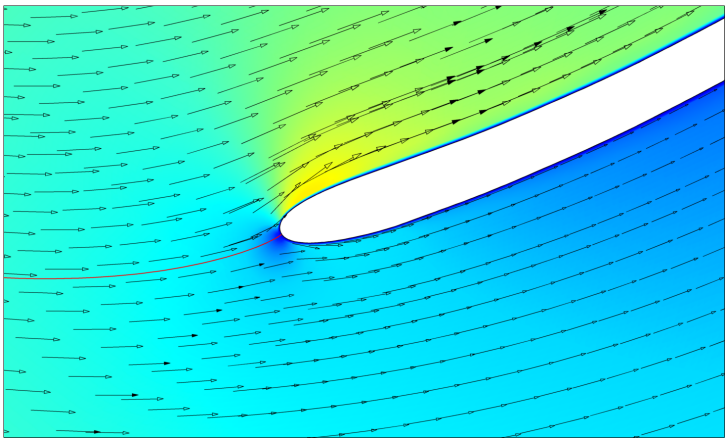

(c) Near choke

Figure 6-4: Relative Mach number contours and relative velocity vectors for radial impeller. The solid red line is the relative stagnation streamline.

influenced by the external Mach number on the blade and the entropy rise through the shock. The entropy rise along the blade is shown in Figs. 6-5(a) to 6-5(c). The boundary layer momentum thickness, which governs the drag on the blade, is set by the leading edge shock strength, which as seen previously, is set by the leading edge incidence and operating condition.

The inputs to the body force model of the radial impeller are computed from single passage RANS simulations. Figures 6-6, 6-7, and 6-8 show the computed D and K_p and extracted b radial distributions, respectively, for operating points near stall, near peak efficiency, and near choke.

The key features of Fig. 6-6 are the sharp change in D at the leading edge and the near 0 value of D for most of the blade. Both of these features represent the change in incidence along the speedline and flow tangency along the blade, respectively. As the compressor moves from choke to stall, the change in D near the leading edge increases which is consistent with the increase in leading edge incidence. The blade metal blockage distribution in Fig. 6-8 shows the rounded leading edge, the constant thickness of the radial blade, and the blunt trailing edge.

6.3 Computational Setup of Body Force Model Simulation - Radial Impeller

The computational setup of the body force model simulation of the radial impeller used FINE/Open-OpenLabs to leverage the ability to model blade metal blockage. A prismatic, one cell deep, 36 degree sector of the flow path annulus was used to generate the body force mesh and is shown in Fig. 6-9. The mesh node count is approximately 9,500, compared to the single passage RANS mesh node count of nearly 100,000. Considering the simulation is periodic in the circumferential direction, the radial node count is 326. The same order of magnitude reduction in computational runtime found for Rotor 37 was also observed for the radial impeller. Similar to the Rotor 37 computational setup, all surfaces were set as Euler slip walls to avoid double

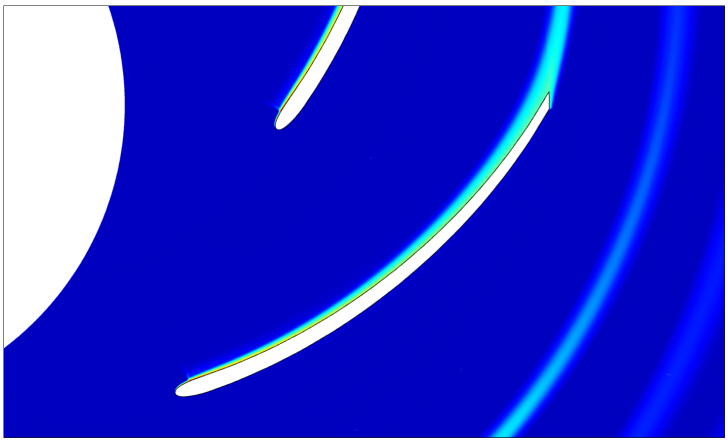

(a) Near stall

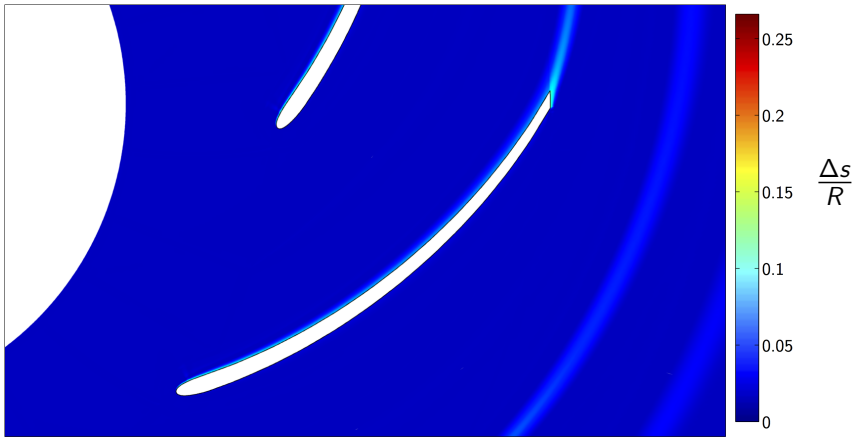

(b) Near design

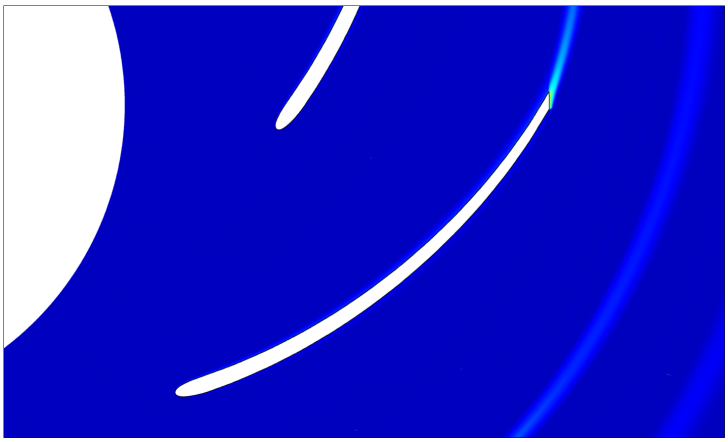

(c) Near choke

Figure 6-5: Radial impeller entropy, $\Delta s/R$.

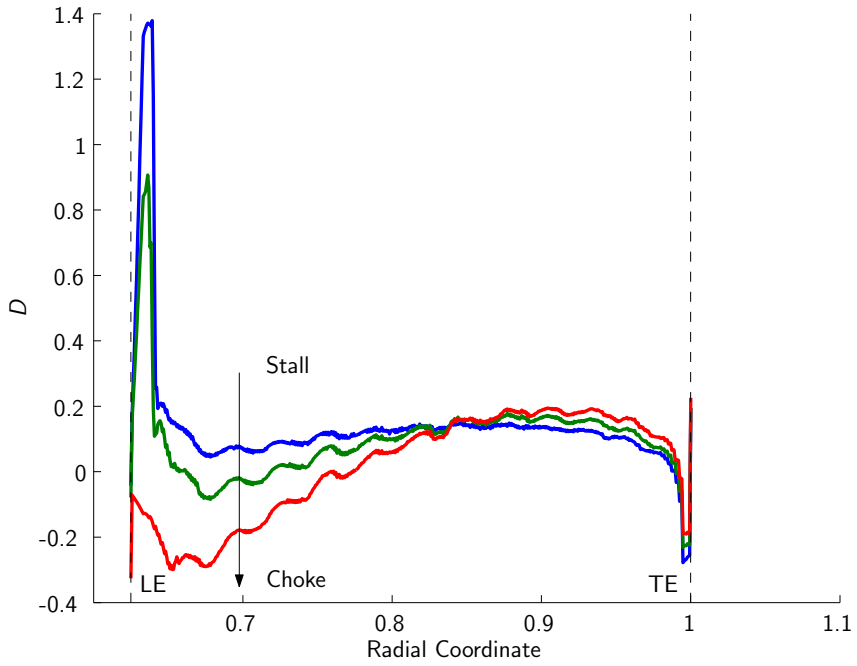

Figure 6-6: Distribution of D for radial impeller.

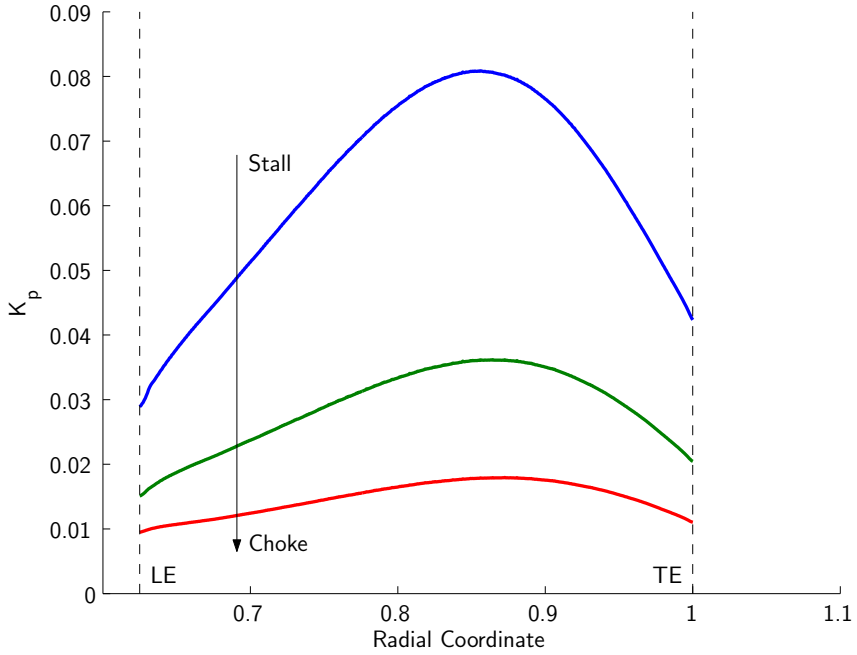

Figure 6-7: Distribution of K_p for radial impeller.

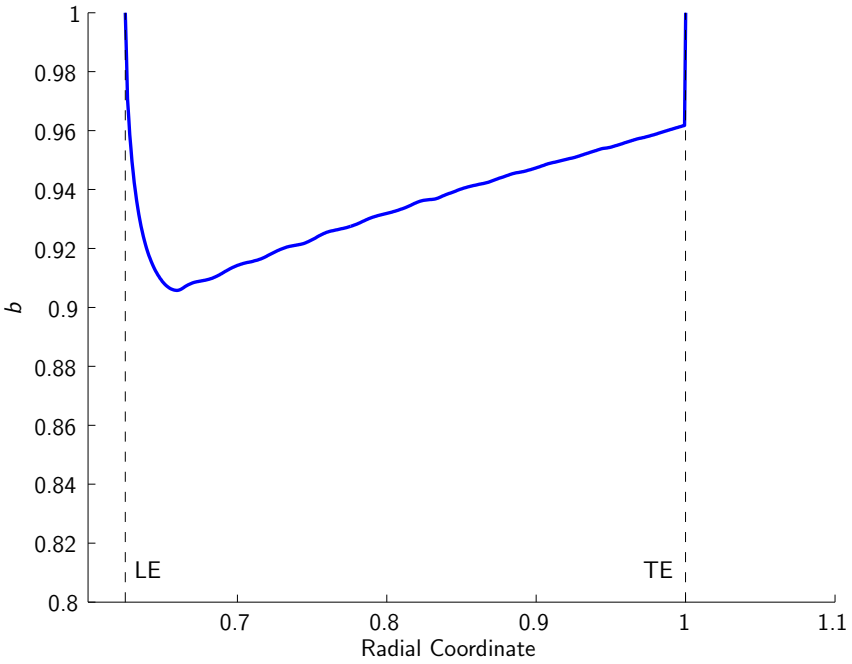

Figure 6-8: Blockage distribution for radial impeller.

bookkeeping endwall entropy rise.

6.4 Polynomial Fitting of Body Force Model Inputs

The unstructured nature of FINE/Open required that the distributions of b, D, and K_p must be represented by polynomial fits. The deviation gradient parameter and viscous parallel force coefficients were represented as functions of radius and upstream inlet flow coefficient, ϕ,

$$D \approx D^* = D^*(r, \phi) \tag{6.1}$$

$$K_p \approx K_p^* = K_p^*(r, \phi) \ . \tag{6.2}$$

Upstream inlet ϕ was used because OpenLabs did not allow a local dependency, such as $D^* = D(r, w)$, to be formulated for individual grid cells. The polynomial fits for

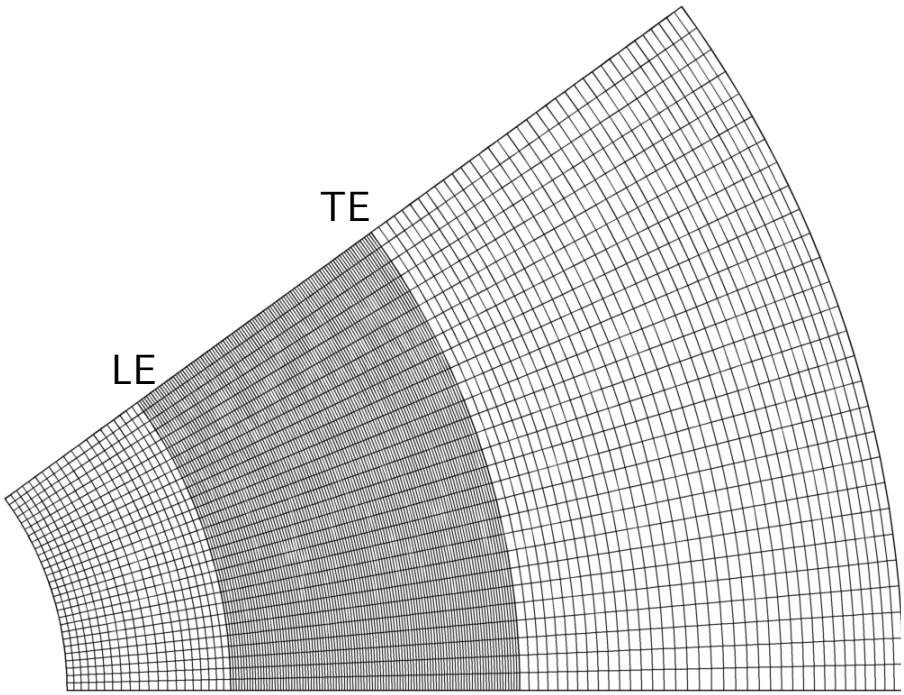

Figure 6-9: Mesh for body force model simulation of a radial impeller.

D and K_p are shown in Figs. 6-10 and 6-11. A piecewise polynomial fit was used to capture the sharp changes in the distributions of D near the leading edge. The location of the cutoff for the piecewise fit was chosen close to the leading edge by inspection.

6.5 Global Performance Comparisons

The overall performance of the compressor is captured by the body force model, as shown by the stage loading coefficient and total-to-static pressure rise coefficient characteristics in Figs. 6-12(a) and 6-12(b), respectively.

There is a 6.75% over prediction in total-to-static pressure rise coefficient and a 5% over prediction in stage loading coefficient near the choke side of the characteristic. The over prediction is due to errors in the polynomial fits for D^* since, due to the impeller's high efficiency and thin blades, the normal force dominates. The

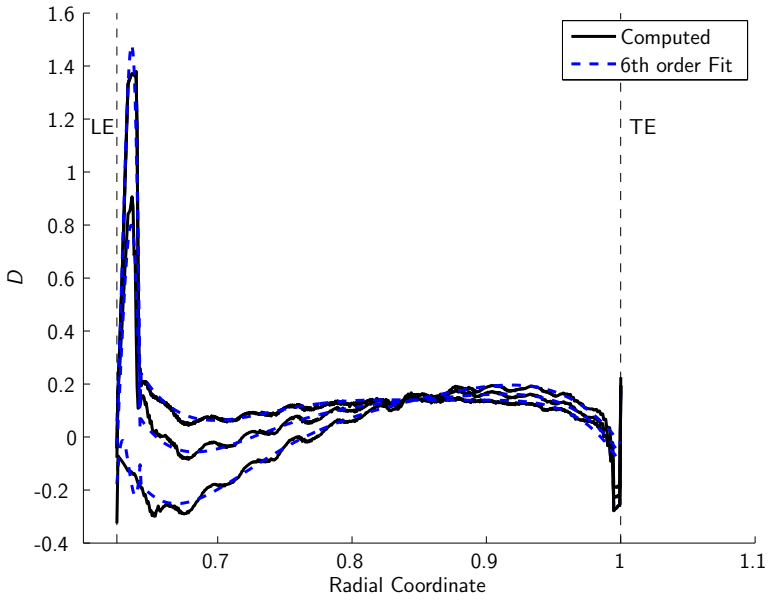

Figure 6-10: Polynomial fits for D^* compared with computed D.

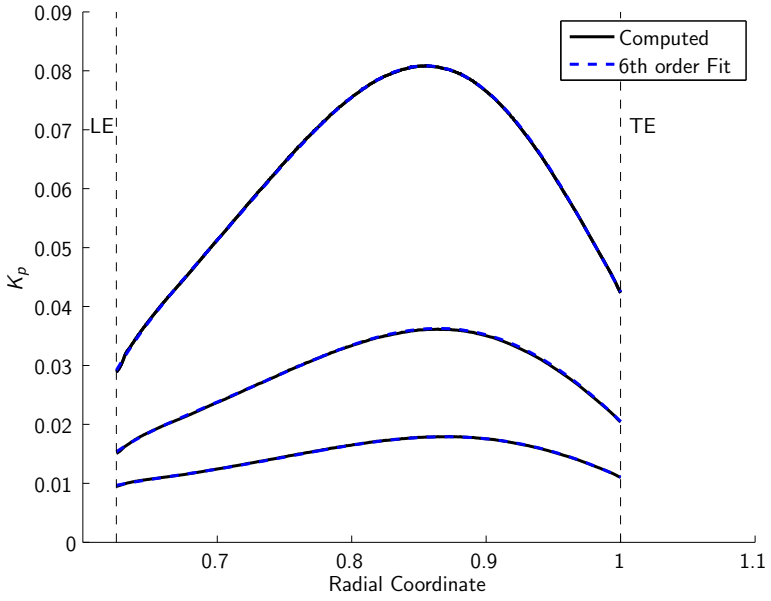

Figure 6-11: Polynomial fits for K_p^* compared with computed K_p.

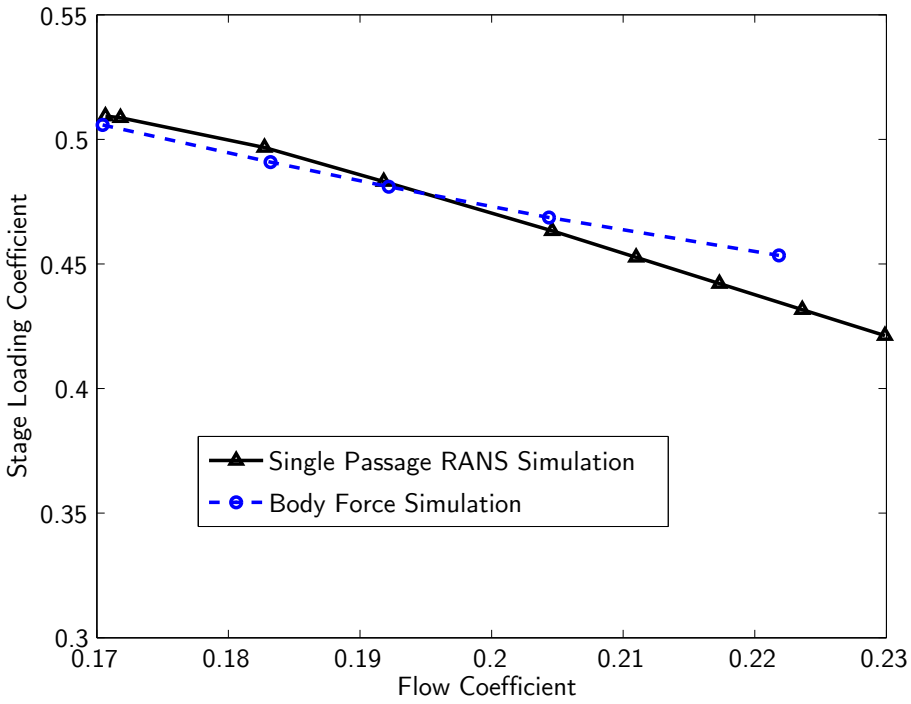

(a) Stage loading coefficient

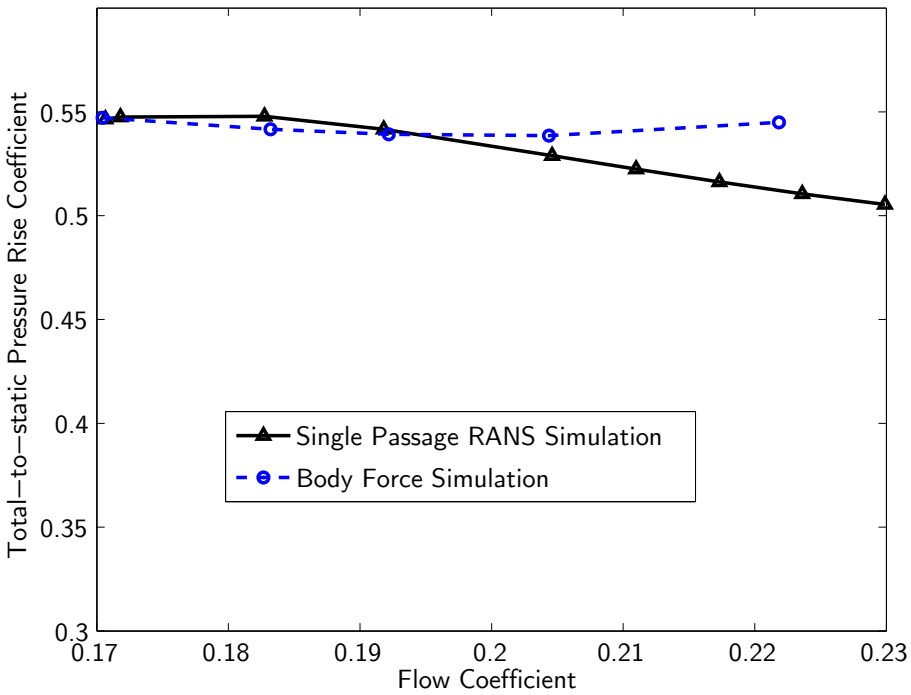

(b) Total-to-static pressure rise coefficient

Figure 6-12: Radial impeller global performance.

discrepancy in the slope of the total-to-static pressure rise coefficient is due to the body force simulation relative flow diffusing more than the relative flow in the single passage RANS simulation near choke. This effect occurs because not all the flow accelerations are captured in the body force model. Both the fitting errors for D^* and the flow acceleration effects are discussed in the next section.

6.6 Flow Field Comparisons

The pitchwise averaged flow field from single passage RANS is compared to the axisymmetric flow field from the body force simulation. The flow field quantities examined are static pressure, absolute total pressure, radial velocity, and relative Mach number. Both pressure quantities are non-dimensionalized by the inlet stagnation pressure and the radial velocity is non-dimensionalized by the impeller trailing edge tip speed. Figures 6-13, 6-14, 6-15, and 6-16 show the static pressure, absolute total pressure, radial velocity, and relative Mach number distributions for an operating point near stall, respectively. Figures 6-17 through 6-20 depict the same quantities for an operating point near peak efficiency and Figs. 6-21 through 6-24 present the same quantities for an operating point near choke. The vertical dashed lines indicate the leading and trailing edge of the blade.

Near stall, the body force model simulation flow field is in good agreement with the pitchwise averaged single passage RANS flow field. However, near choke, the body force model over predicts the flow turning by 5%. The over prediction in total pressure begins at the leading edge and is indicative of excess normal force.

Over Turning due to Polynomial Fitting Errors

Examination of D^* near the leading, presented in Fig. 6-25, shows that near choke, D^* is larger than D. The normal force was computed using D^*, the flow field from the single passage RANS data, and Eq. 3.15 to understand how the modeled normal force is affected by the increase in D^*. This reconstruction is shown in Fig. 6-26 and the relative errors in D^* and the modeled $f_{\mathrm{n,turn}}$ at the leading edge are given in

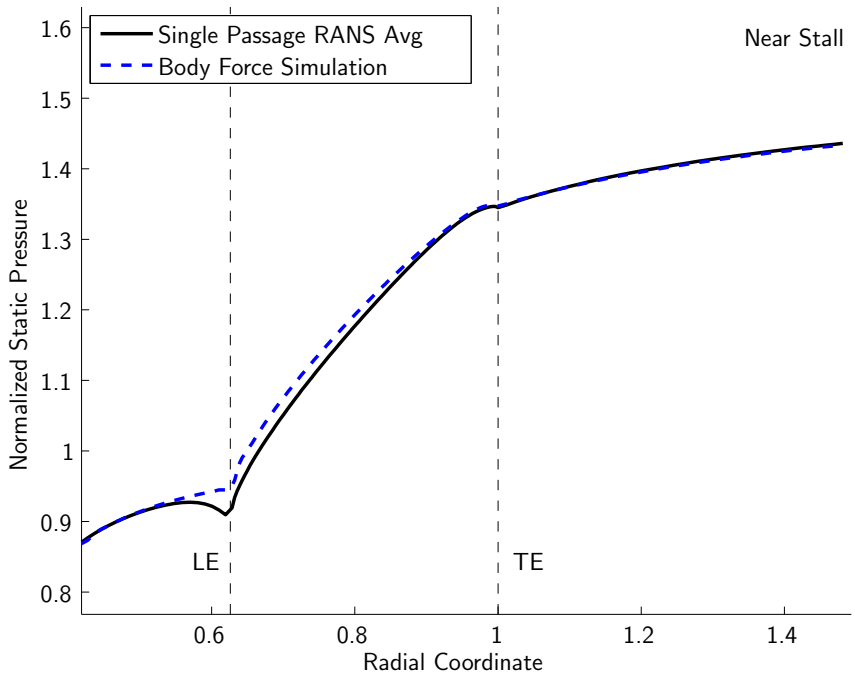

Figure 6-13: Radial impeller static pressure comparison near stall.

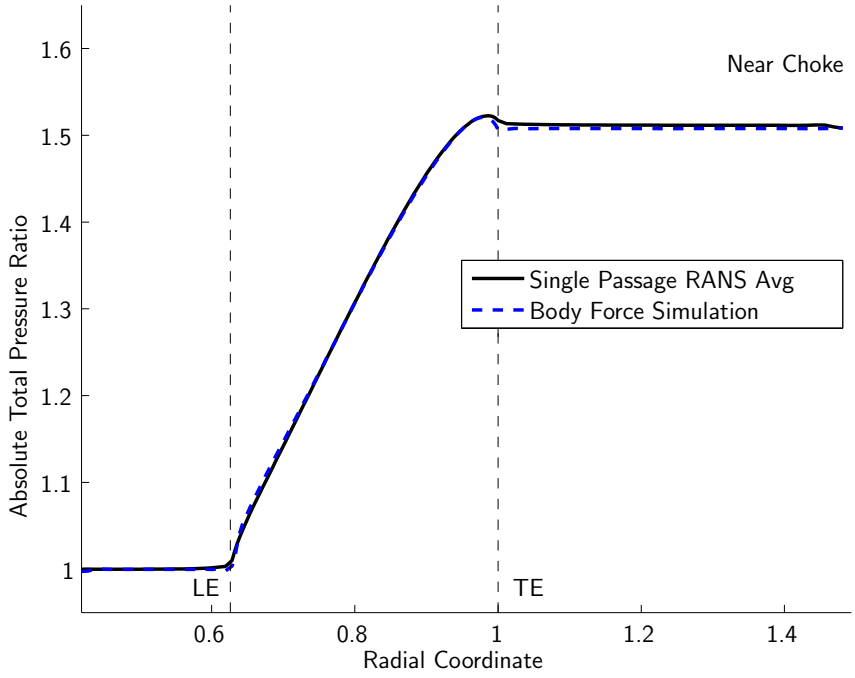

Figure 6-14: Radial impeller absolute total pressure ratio comparison near stall.

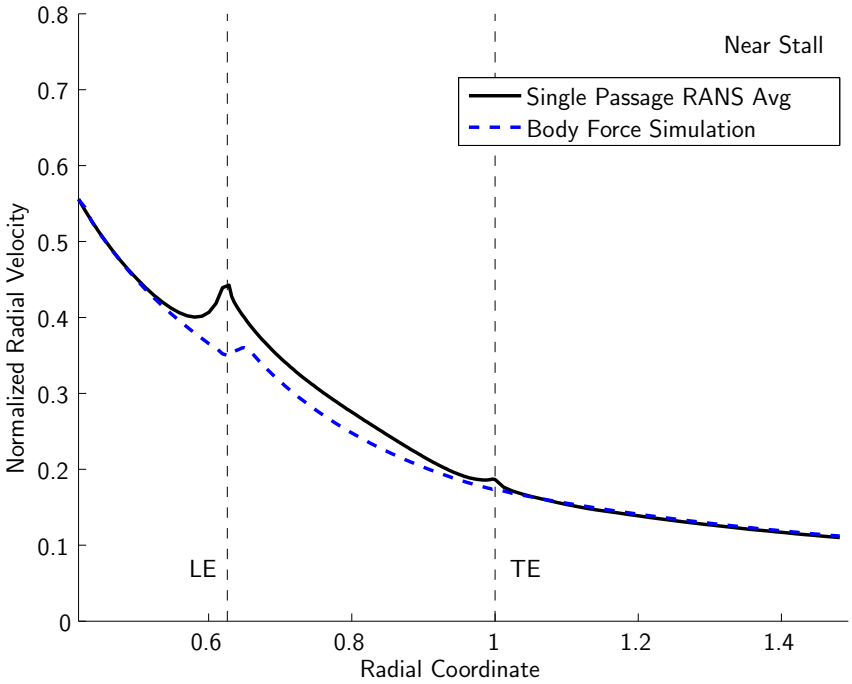

Figure 6-15: Radial impeller radial velocity comparison near stall.

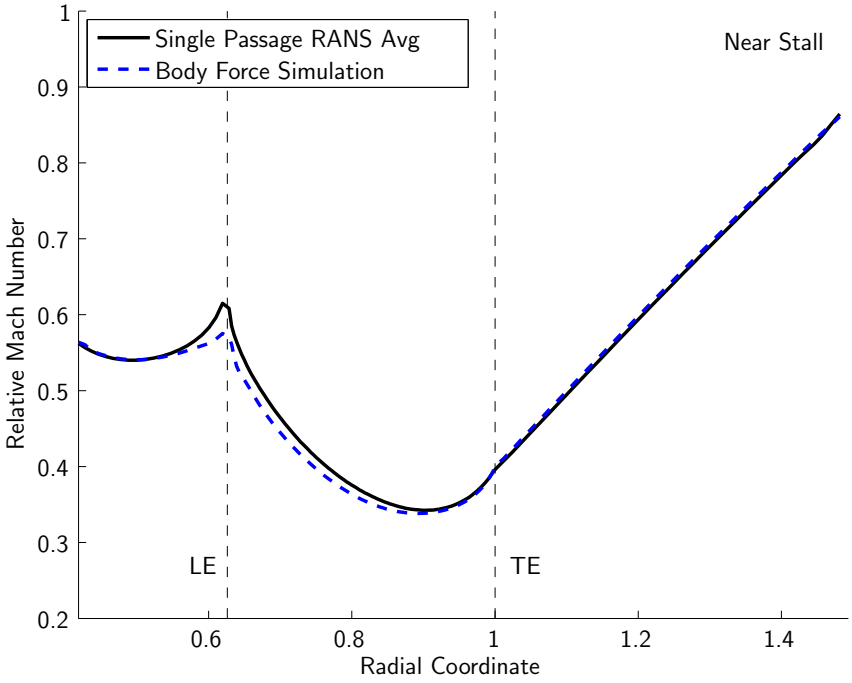

Figure 6-16: Radial impeller relative Mach number comparison near stall.

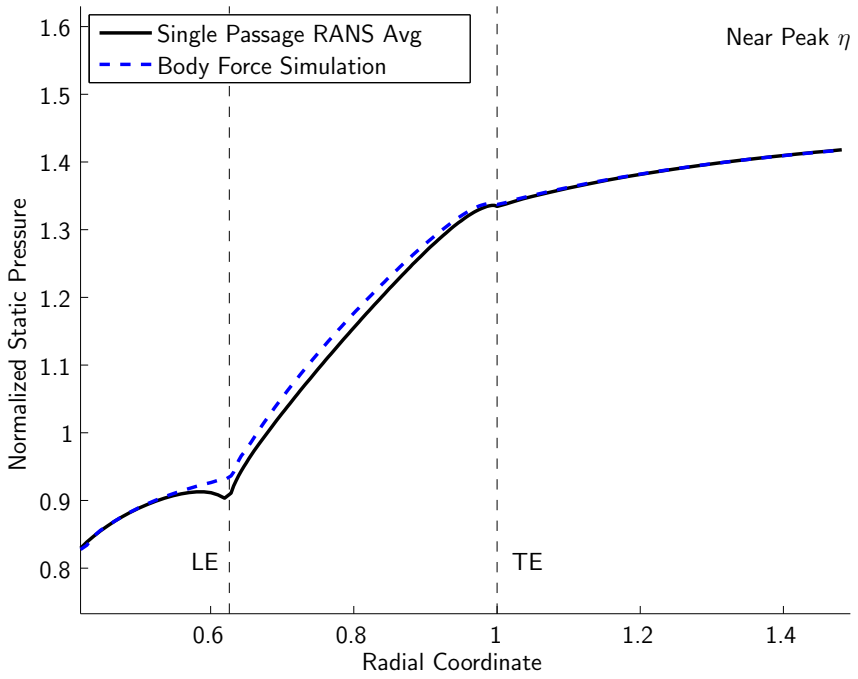

Figure 6-17: Radial impeller static pressure comparison near peak efficiency.

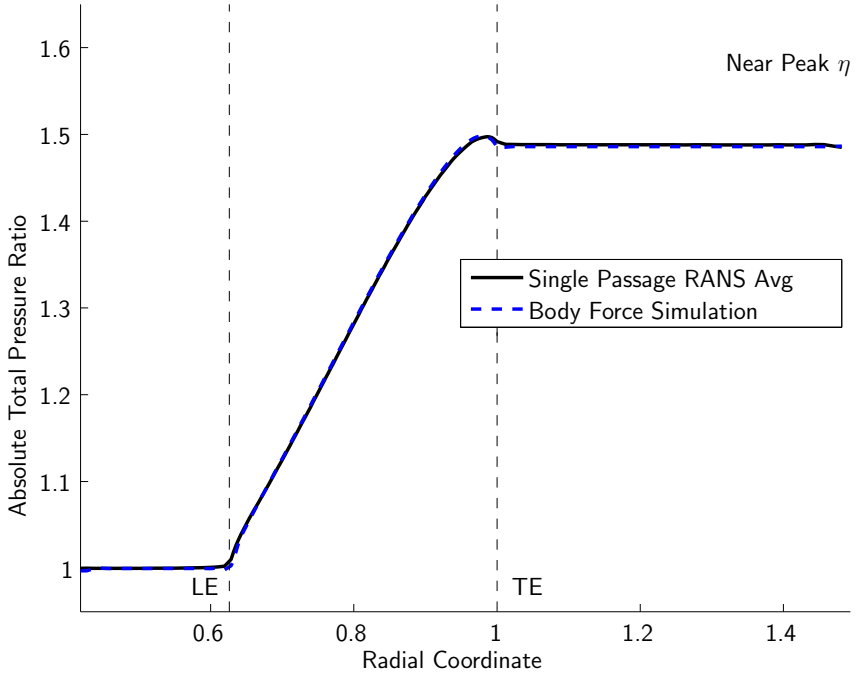

Figure 6-18: Radial impeller absolute total pressure ratio comparison near peak efficiency.

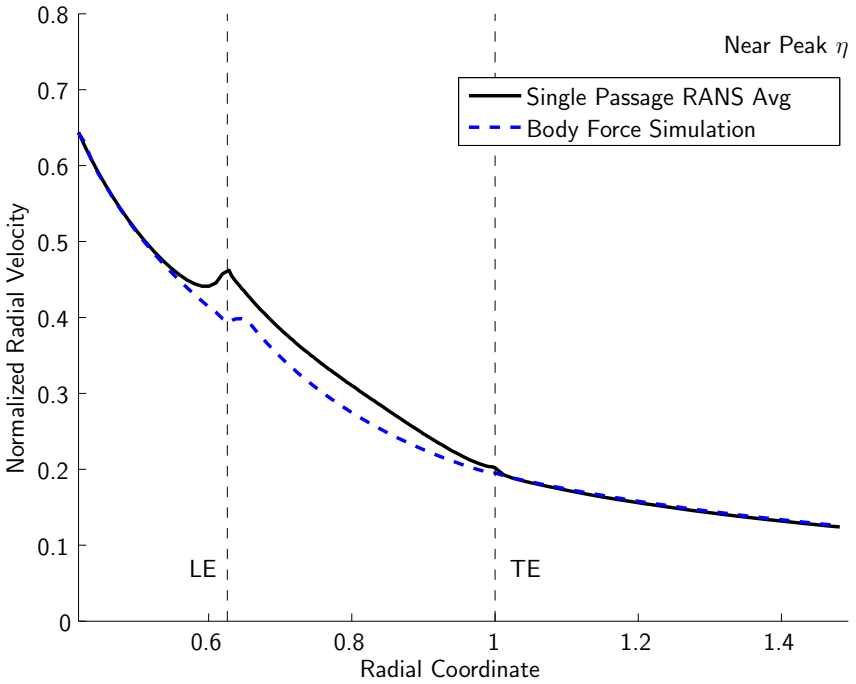

Figure 6-19: Radial impeller radial velocity comparison near peak efficiency.

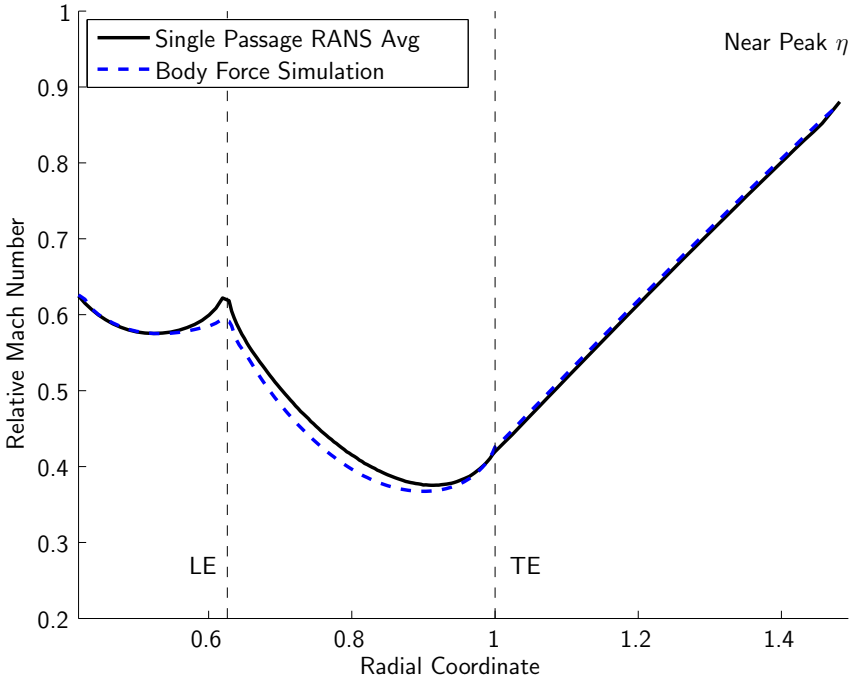

Figure 6-20: Radial impeller relative Mach number comparison near peak efficiency.

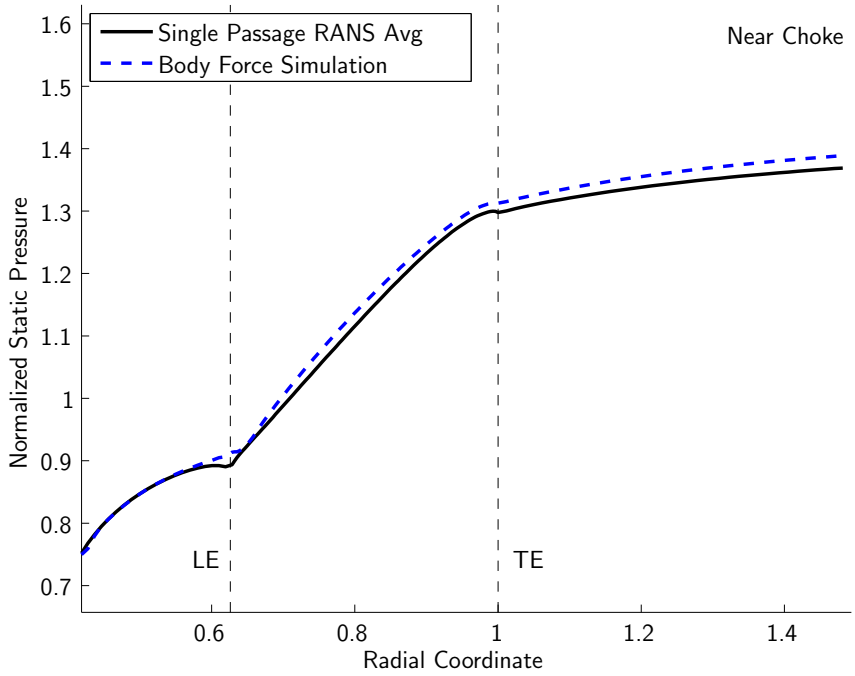

Figure 6-21: Radial impeller static pressure comparison near choke.

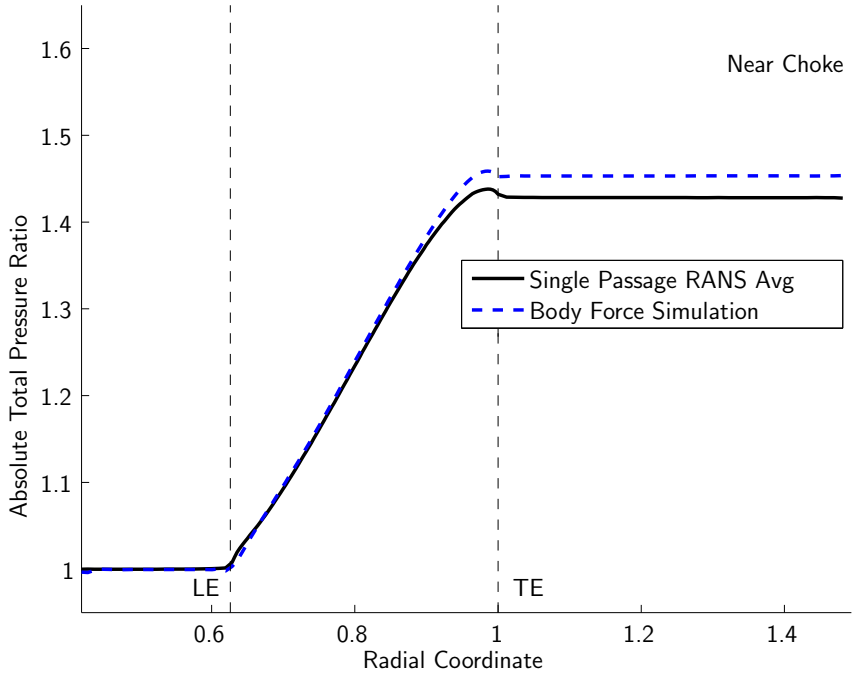

Figure 6-22: Radial impeller absolute total pressure ratio comparison near choke.

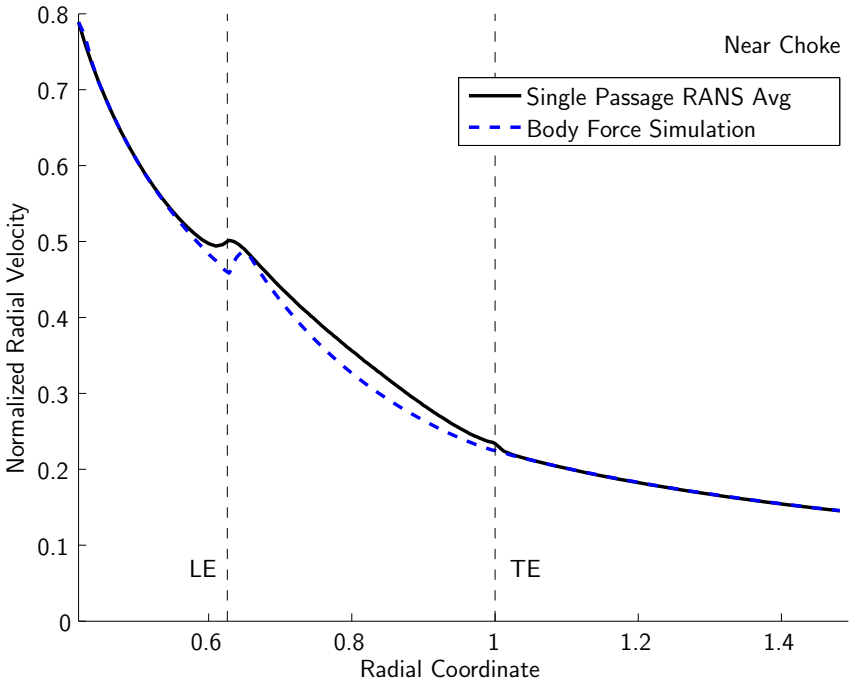

Figure 6-23: Radial impeller radial velocity comparison near choke.

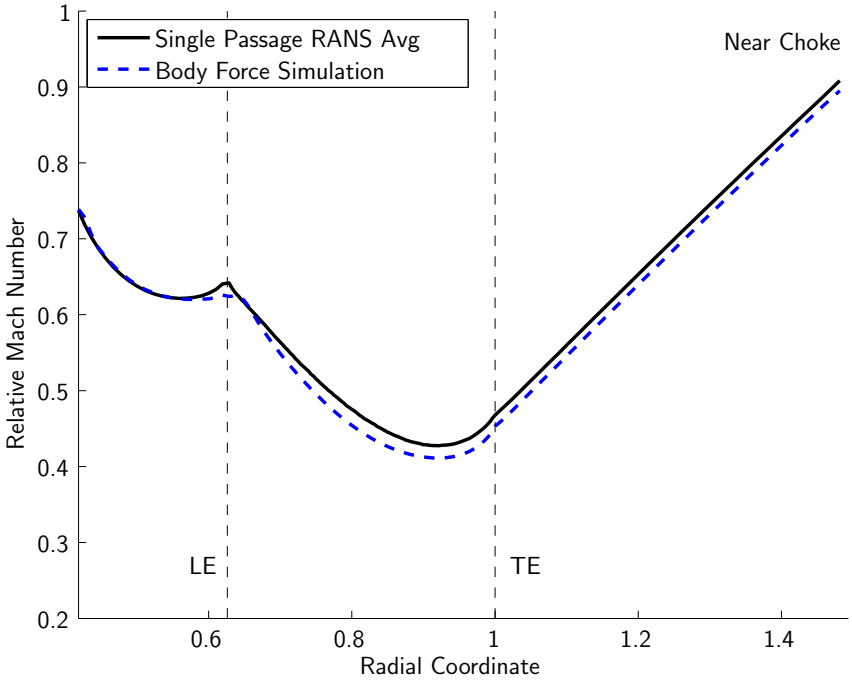

Figure 6-24: Radial impeller relative Mach number comparison near choke.

Fig. 6-27.

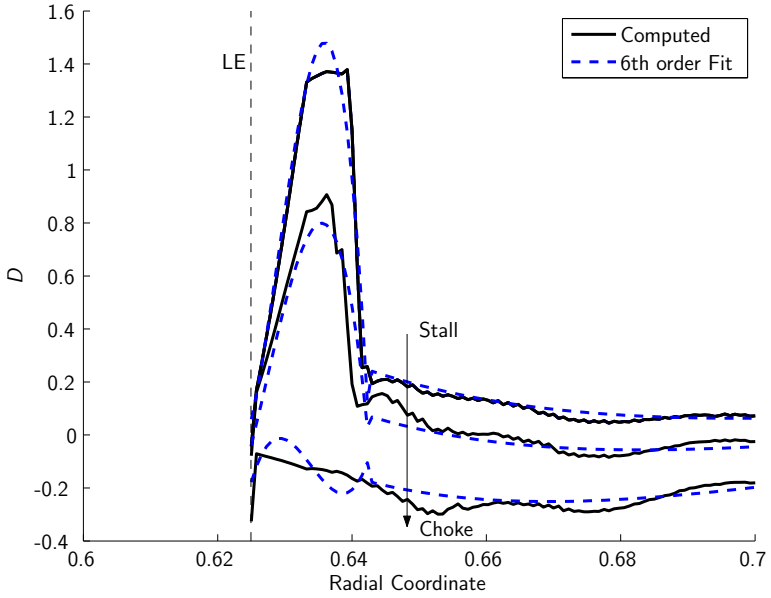

Figure 6-25: Sixth-order LSQ fit for D.

Only the leading edge is examined because this is where the large magnitudes of D occur. The peaks in errors in D^* near the leading edge correspond to peaks in errors for reconstructed $f_{\text{n,turn}}$. The reconstructed $f_{\text{n,turn}}$ is larger than the extracted $f_{\text{n,turn}}$ for most of the leading edge region which confirms that fitting errors in D^* are the cause of the over prediction in turning near choke.

Errors in Blade Passage Acceleration

While the body force simulation flow quantities at the exit of the blade passage are in good agreement with those from the single passage RANS simulations, the static pressure within the blade passage is over predicted and the radial velocity and relative Mach number are under predicted. Table 6.2 quantifies the errors in flow quantities within the blade passage and shows that the flow acceleration within the blade passage is not fully captured due to the lack of upstream influence and the lack of aerodynamic blockage.

Upstream influence in the radial impeller occurs due to the presence of discrete blades. Modeling discrete blade passages with an axisymmetric flow field eliminates

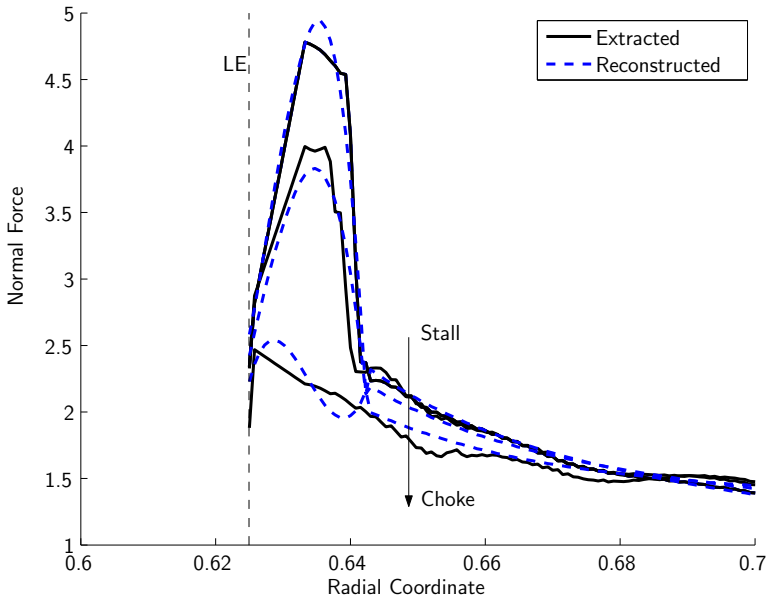

Figure 6-26: Reconstruction of $f_{\mathrm{n,turn}}$ using normal force model based on polynomial fits for D and single passage RANS flow field.

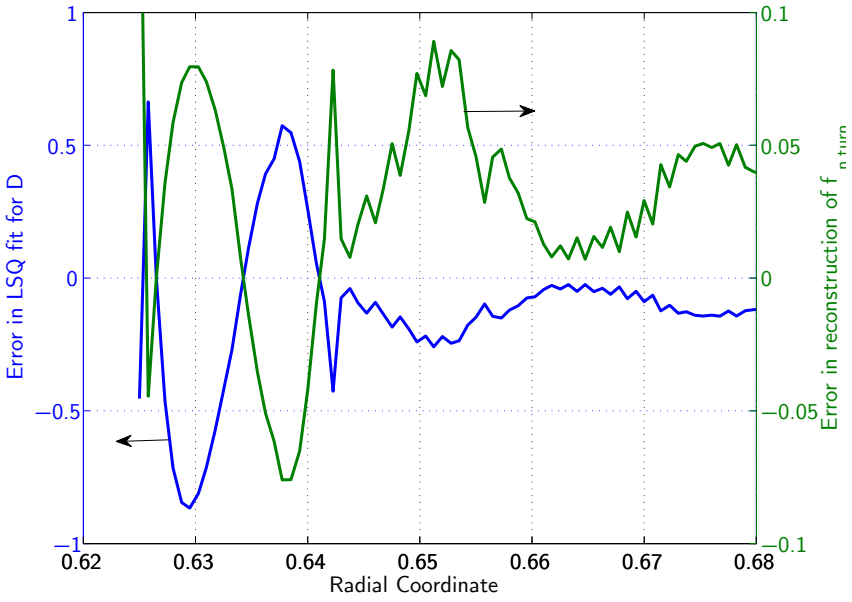

Figure 6-27: Relative error in D^* and reconstructed $f_{\mathrm{n,turn}}$ for leading edge region near choke.

Table 6.2: Errors in body force modeling of radial impeller within blade passage as percentage of single passage RANS simulation

Op Point\Flow Quantity → ↓	p	p_t	u_r	M^{rel}
Nr Stall	+2.14%	+0.34%	-9.31%	-3.7%
Nr Pk η	+1.71%	-0.087%	-7.41%	-3.18%
Nr Choke	+1.88%	+0.36%	-5.17%	-3.5%

this non-uniformity in the pressure field which also removes the upstream influence, as noted in Sec. 5.3. Therefore, the flow field in the body force simulation does not experience a change until the blade leading edge. This effect can be seen by examining the radial velocity near the blade leading edge, shown in Fig. 6-28.

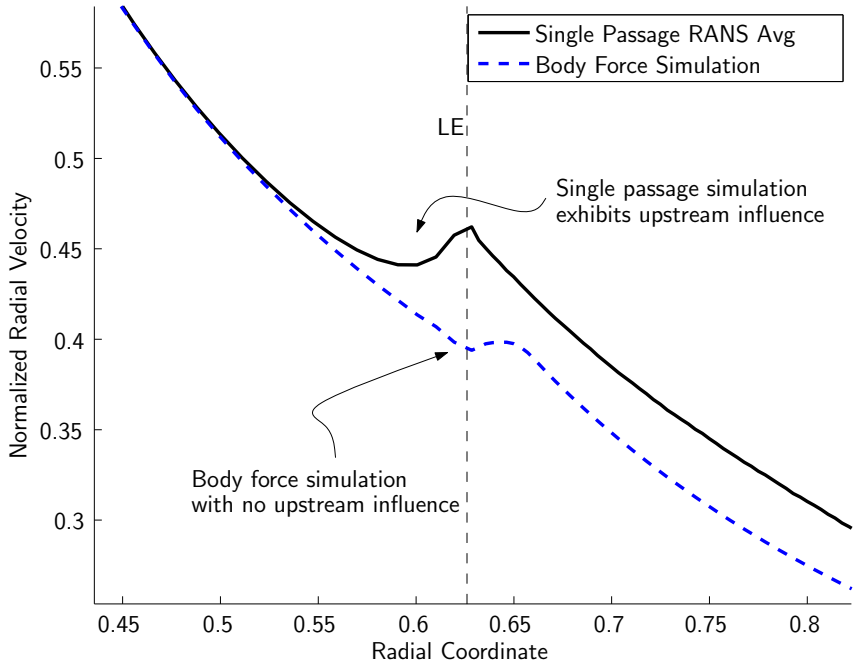

Figure 6-28: Body force model in current form does not capture upstream influence.

The lack of upstream influence results in a lower radial velocity at the blade leading edge. Upstream influence could be modeled by introducing a circumferentially non-uniform source term to mimic the presence of discrete blades. A similar method was employed by Defoe [7] to model the leading edge shocks of an axial fan in order to

compute the noise propagation.

The lack of aerodynamic blockage modeling also results in a lower radial velocity within the blade passage, which is seen at all operating points. While aerodynamic blockage is not presently modeled, it can be accounted for by comparing single passage RANS simulations and body force simulations. The difference between the flow fields is the effect of aerodynamic blockage and could be modeled by introducing a correction, similar to the method discussed in [2].

Chapter 7

Implementation Challenges for Three Dimensional Blade Geometries

While the blade passage model has been validated on a prismatic radial impeller, converged body force simulations for a centrifugal compressor with three dimensional blade geometry could not be obtained. The same implementation was applied for the Rotor 37 test case but converged body force simulations were also not obtained. Considering the past success of similar blade passage models for axial compressors, such as for example, [2], there appears to be an implementation error. A series of diagnostics on a centrifugal compressor with three dimensional blade geometry were performed and are described here to provide record of what steps have been carried out and what potential future work might remain.

7.1 Status of Analytical Blade Passage Model

Before any computational diagnostics were performed, the elements of the blade passage model were validated or compared to similar models to ensure accuracy. A special case of the normal force model when $\varphi = 0$ and $\lambda = 0$, corresponding to a purely axial gas path with no blade lean, reduces Eq. 3.15 consistently to the axial

compressor case demonstrated in the literature. Validation of the normal force model on the prismatic radial impeller in Chap. 6 suggests that the normal force model has been derived correctly. The derivation of the viscous parallel force model is consistent with the form of the model by Gong [14]. The blade metal blockage model was validated in Chap. 5. In summary, Tab. 7.1 presents the current status of validation of the different components and procedures for the blade passage model.

Table 7.1: Current status of blade passage model validation

Model Component (Chap. 3)	Body Force Field Extraction (Chap. 4)	Prescribed Field Implementation (Chap. 5)	Model Validation (Chap. 6)
Normal Force	✓	✓	Purely axial [2] or radial
Viscous Parallel Force	✓	✓	✓
Blade Metal Blockage	✓	✓	✓

Diagnostic checks also indicated that the storing of geometrical and blade passage model input distributions in the source term implementation was performed correctly. Based on the status of validation of the blade passage model and the following diagnostics, it is believed that the implementation error lies in the computation of D for three dimensional blade geometries.

7.2 Computational Setup for Body Force Model Diagnostics

Preliminary body force model simulations showed that the normal force model was the destabilizing component of the implementation. Single passage Euler simulations were carried out in FINE/Turbo in order to isolate the normal force effects from the viscous parallel force effects.

The centrifugal compressor stage used by Spakovszky and Roduner [39] and Benneke [1] was chosen as the diagnostics test case. The salient features of the compressor are given in Tab. 7.2 and more information can be found in [39].

Table 7.2: Centrifugal compressor data.

Number of blades, N_B	9+9/16
Design pressure ratio, PR	≈ 5
Impeller tip Mach number, M_{u_2}	> 1

7.2.1 Computational Setup of Single Passage Euler Simulations - Centrifugal Compressor

For the same geometry, the single passage Euler mesh is much coarser and more uniform than the single passage RANS mesh to avoid numerical dissipation. The Euler mesh for the centrifugal compressor is illustrated in Fig. 7-1 and has a node count of approximately 80,000, an order of magnitude less than the node count for a single passage RANS mesh for the same compressor geometry [1].

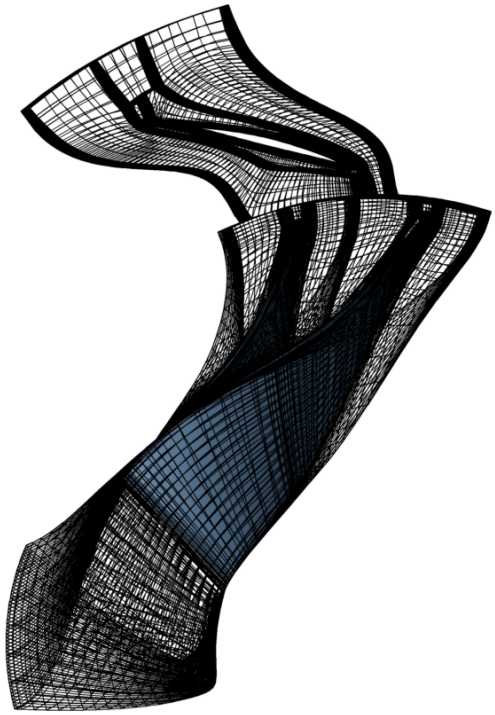

Figure 7-1: Single passage Euler mesh of a centrifugal compressor.

The normal force extracted from an Euler simulation at a mass flow near peak

efficiency of the single passage RANS speedline, using the extraction method described in Chap. 4, was used to compute the distribution of D . The computed D distribution was then used as the input to the normal force model in attempts to reconstruct the axisymmetric flow field from the Euler simulation.

7.2.2 Computational Setup of Body Force Model Simulations - Centrifugal Compressor

As noted previously, the commercial CFD package FINE/Open is unstructured, and as a result any distributions that are input must use a polynomial fit. While polynomial fits in one dimension provide low relative errors, expanding the fit to two dimensions increases the errors. Given these restrictions, it was decided to use FINE/Turbo to diagnose issues with the implementation of the normal force model to eliminate errors associated with the polynomial fits.

The mesh used for the body force simulations is generated in a similar manner to the Rotor 37 mesh since FINE/Turbo can use a mesh directly from IGG. Figure 7-2 shows the body force mesh which has a grid node count of approximately 27,500 and a meridional node count of nearly 3,000, a similar value to the meridional node count of Rotor 37. Euler walls were used to ensure consistency with the single passage Euler simulations. The grid refinement at the leading and trailing edges of the blade row blocks are to ensure blade metal blockage modeling accuracy in FINE/Open. The body force grid generated was used in preliminary diagnostics in both FINE/Turbo and FINE/Open. It was found that since the blade metal blockage model essentially adds mass flow when the blade thickness is increasing and vice versa, there is the possibility of the inlet mass flow not matching the outlet mass flow due to the topology of the distribution of b and the mesh density near the leading and trailing edges.

Scaling of Extracted Normal Force Due to Solver Limitations

The inability of FINE/Turbo to model blade metal blockage leads to an increase in the residence time of fluid particles traveling through the impeller. This effect can be

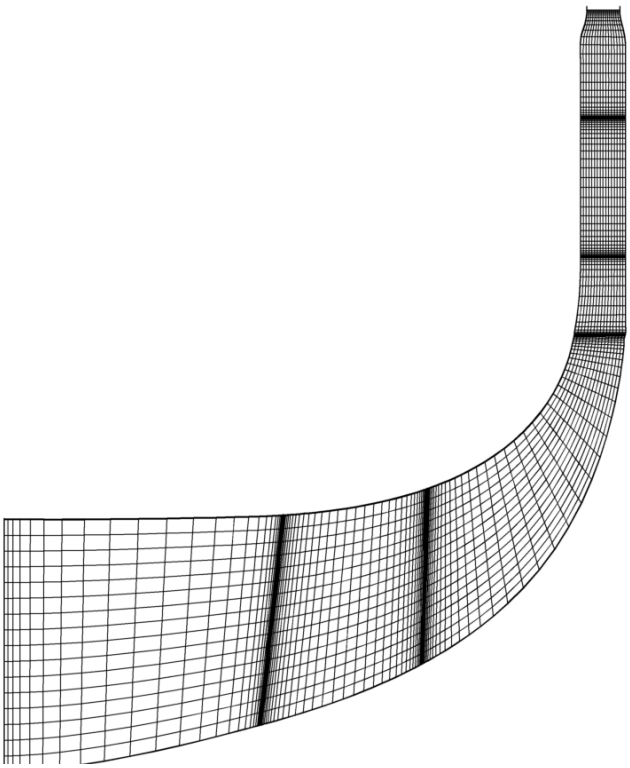

Figure 7-2: Body force mesh of a centrifugal compressor.

seen by examining Eq. 2.9 rearranged as,

$$dh_t = \frac{\Omega r f_\theta}{w_m} dm \ , \tag{7.1}$$

where $\Omega r f_\theta$ is the shaft power, and $\frac{dm}{w_m}$ is the residence time of a fluid particle within the blade row. In a simulation with no blockage, the residence time is larger due to lower values of w_m, which leads to an increased change in stagnation enthalpy. Therefore, given the extracted $f_{\text{n,turn}}$, a scaling is required to correct for the lack of blade metal blockage modeling in FINE/Turbo.

7.3 Prescribed Body Force Field for Impeller-Only Simulations

Preliminary simulations of the centrifugal compressor with a prescribed body force field diverged due to separation at the hub or shroud. The separation was caused by the high swirl at the impeller exit and the lack of aerodynamic blockage modeling in the vaned diffuser. Considering that the Euler turbine equation relates the change of stagnation enthalpy with the change in angular momentum, an increase in h_t yields an increase in ru_θ. For a given radius and operating condition, the increase in u_θ and decrease in w_m, relative to the single passage simulation, produces a larger absolute flow angle α which makes the flow more likely to separate, even in an Euler body force simulation due to numerical dissipation, in the radial components of the compressor.

The relationship between flow separation and blockage can also be seen by considering the flow in a discrete blade passage and the flow in a body force simulation where aerodynamic blockage is not accounted for. The aerodynamic blockage in a discrete blade scenario displaces and accelerates the flow to a greater degree than the acceleration due to only blade metal blockage. The $f_{\mathrm{p,visc}}$ applied in the body force simulation is extracted from the discrete blade passage simulation even though the absolute velocities are different. Consider the one dimensional streamwise momentum equation with body forces in the absolute frame,

$$\frac{du}{u} = \frac{dp}{\rho u^2} + \frac{f_{\mathrm{p,visc}} d\ell}{u^2} \ , \tag{7.2}$$

where $\frac{du}{u}$ is the fractional change in absolute velocity, dp is the differential change in pressure, and $d\ell$ is the differential streamwise length. For the same dp and $f_{\mathrm{p,visc}}$, a lower u will undergo a larger change in u, increasing the chance of separation.

In order to avoid separation in the vaned diffuser during diagnostic tests, the body force simulation was carried out with no source terms in the diffuser. The impeller-only calculation allowed for the isolation of inviscid impeller effects and the results of prescribing a scaled normal force as a source term are shown in Figs. 7-3 to 7-5.

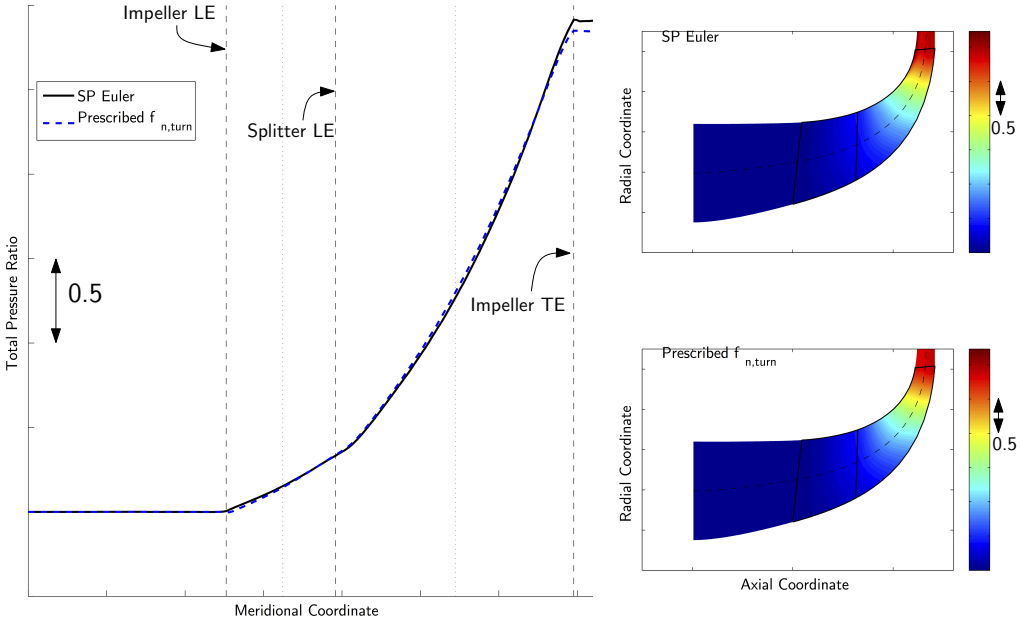

Figure 7-3: Absolute total pressure comparison between impeller-only body force simulation and single passage Euler simulation.

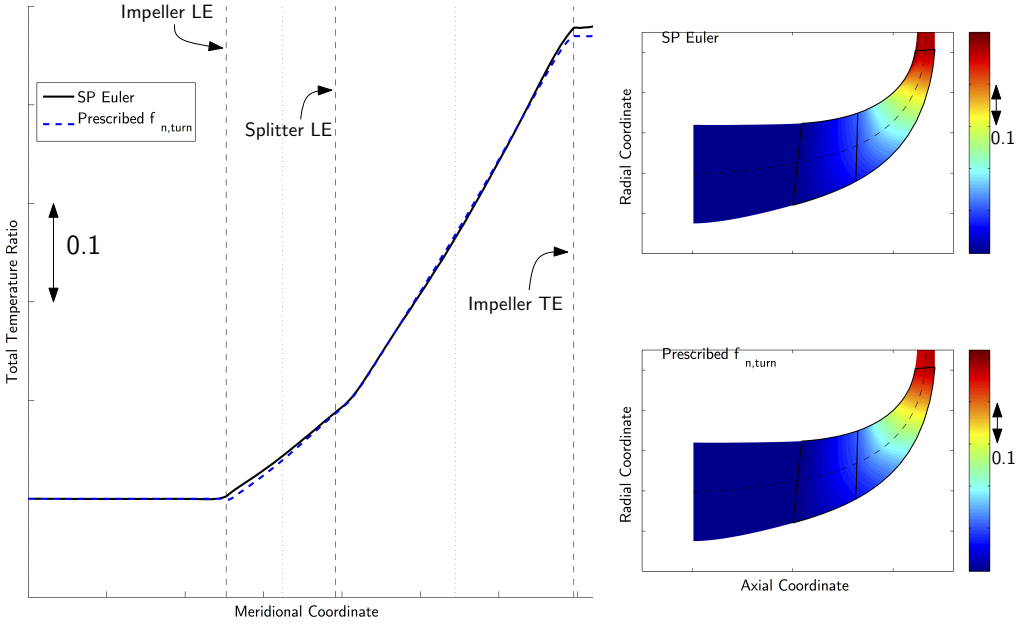

Figure 7-4: Absolute total temperature comparison between impeller-only body force simulation and single passage Euler simulation.

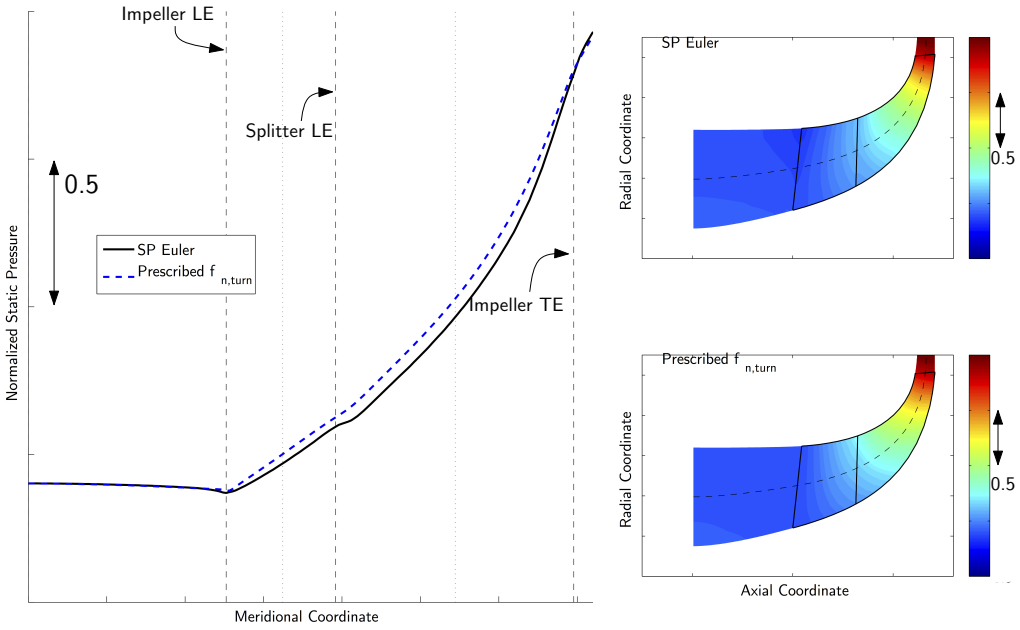

Figure 7-5: Static pressure comparison between impeller-only body force simulation and single passage Euler simulation.

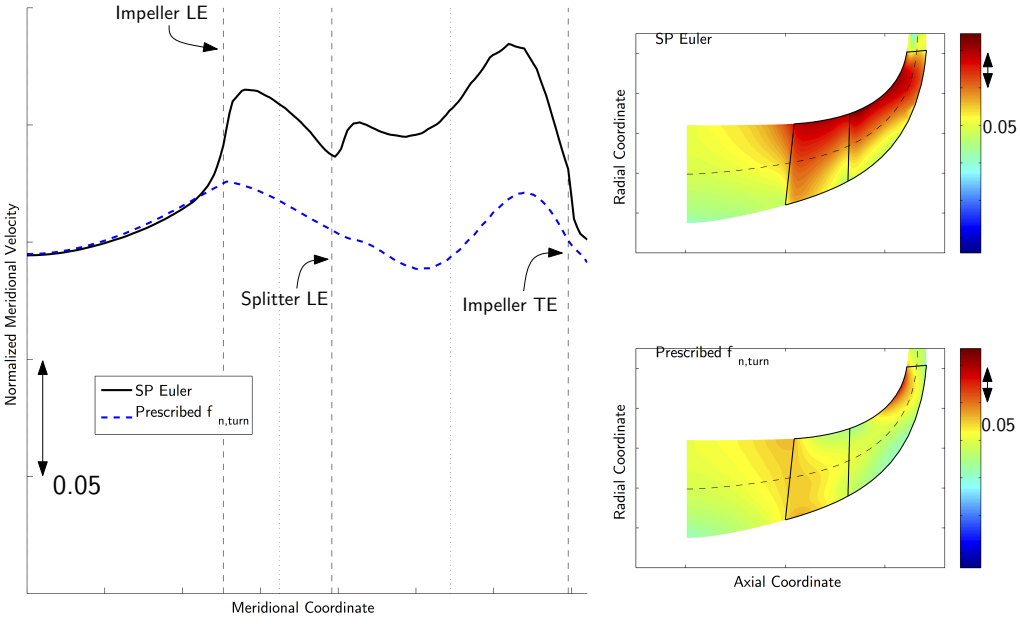

Figure 7-6: Meridional velocity comparison between impeller-only body force simulation and single passage Euler simulation.

The scaling applied to the $f_{\mathrm{n,turn}}$ field was computed by comparing the flow turning in a body force simulation with the extracted $f_{\mathrm{n,turn}}$ (scaling = 1) and to the flow turning in the single passage Euler simulation form which the force field was extracted. The impeller-only body force simulation using a scaled normal force field shows good agreement in total pressure, total temperature, and static pressure rises with the flow field from the single passage Euler simulation. The difference in meridional velocity, shown in Fig. 7-6 is due to the lack of blade metal blockage modeling. Figure 7-7 shows the ratio of the meridional velocity from the body force simulation (with no blockage model) to the meridional velocity from the single passage Euler simulation and the blade metal blockage distribution of the compressor.

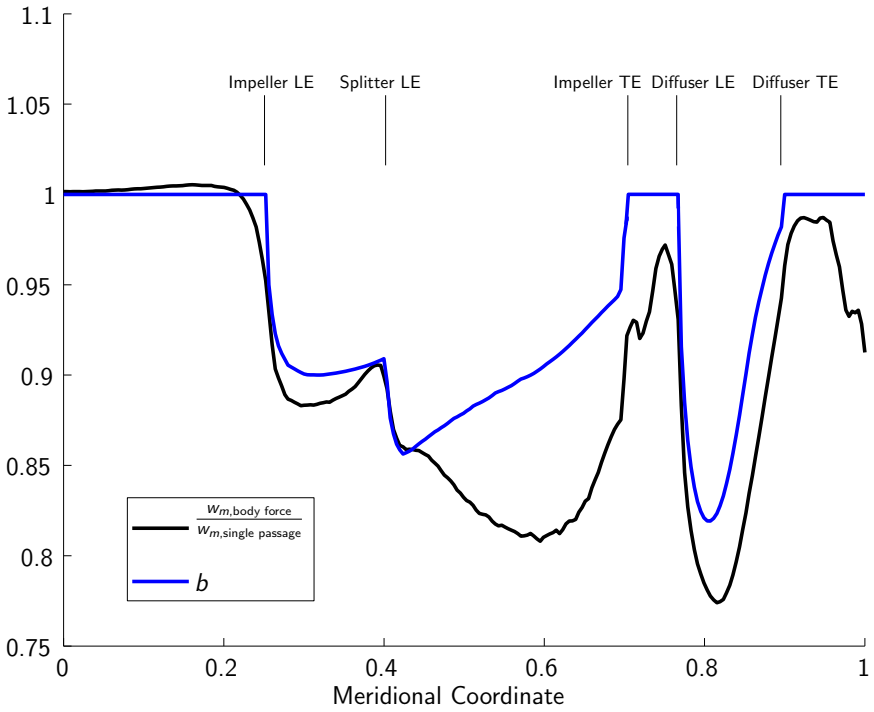

Figure 7-7: Comparison of ratio of single passage Euler simulation w_m to body force simulation w_m and b.

The difference between the two curves is attributed to secondary flow, aerodynamic blockage, and compressibility effects. Even though the single passage simulation is inviscid in nature, there is still numerical dissipation that creates some aerodynamic blockage.

7.4 Dependency of Deviation Gradient Parameter on Relative Velocity

Once the flow turning from the single passage Euler simulation was recreated with the scaled body force field, a preliminary normal force simulation with a prescribed D distribution was executed and found to diverge. The effect of blade metal blockage was incorporated by dividing w_m by b to account for flow displacement,

$$\widetilde{w_m} = \frac{w_{m_{solver}}}{b} \tag{7.3}$$

$$f_{\text{n,turn}} = f_{\text{n,turn}}\left(w(\widetilde{w_m}, w_\theta), D(x,r)\right) \ , \tag{7.4}$$

where $w_{m_{solver}}$ is the meridional velocity computed by the FINE/Turbo solver, with no blade metal blockage.

It was hypothesized that using a prescribed D distribution over constrained the simulation and does not allow the solver to model the flow field appropriately. As the solver iterates, the local flow conditions and the local operating condition change. An example is shown in Figs. 7-8 and 7-9 which present the deviation gradient term $w^2\frac{D}{r_2}$ as a function of w_m and w_θ, respectively. The dashed blue lines are lines of constant value of the alternate relative velocity component, i.e. w_θ for Fig. 7-8 and w_m for Fig. 7-9, while the solid black line is the change in the term along the speedline[1]. The discrepancy between the linearization and extracted data is indicative of a prescribed D distribution over constraining the simulation.

Based on this hypothesis, polynomial fits of D as a function of the local flow field were computed and the coefficient distributions stored in the source term implementation to ensure that the normal force model accurately represents the change in normal force based on a change in the local flow field. The independent variable was chosen to be w. Inspection of D as a function of w, w_m, w_θ, and β showed that $D(w)$ provide the most reliable dependency. Rather than using a two-dimensional polyno-

[1]The meridional velocity used is extracted from the single passage Euler simulation and includes the effect of blade metal blockage.

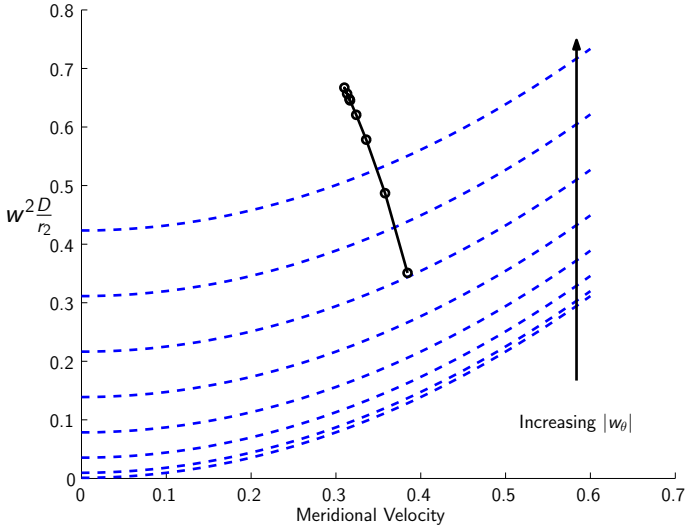

Figure 7-8: Linearization of deviation gradient term near the impeller midspan leading edge as a function of meridional velocity. The dashed blue lines are lines of constant values of relative tangential velocity and the solid black line are data extracted along the speedline.

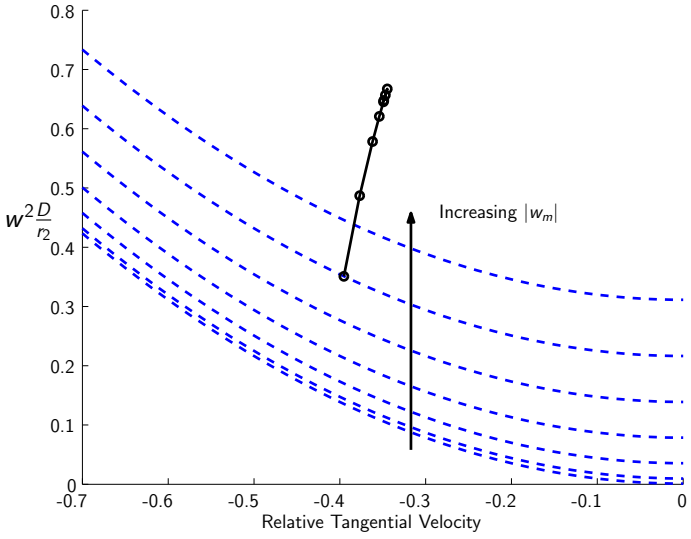

Figure 7-9: Linearization of deviation gradient term near the impeller midspan leading edge as a function of relative tangential velocity. The dashed blue lines are lines of constant values of meridional velocity and the solid black line are data extracted along the speedline.

mial fit as a function of w_m and w_θ, which can introduce larger errors, the options were narrowed to w and β. Due to flow tangency, the range of β over the speedline can be small compared to the range in w. An example of the difference in range for w, nondimensionalized by the impeller tip speed, and β is shown in Fig. 7-10.

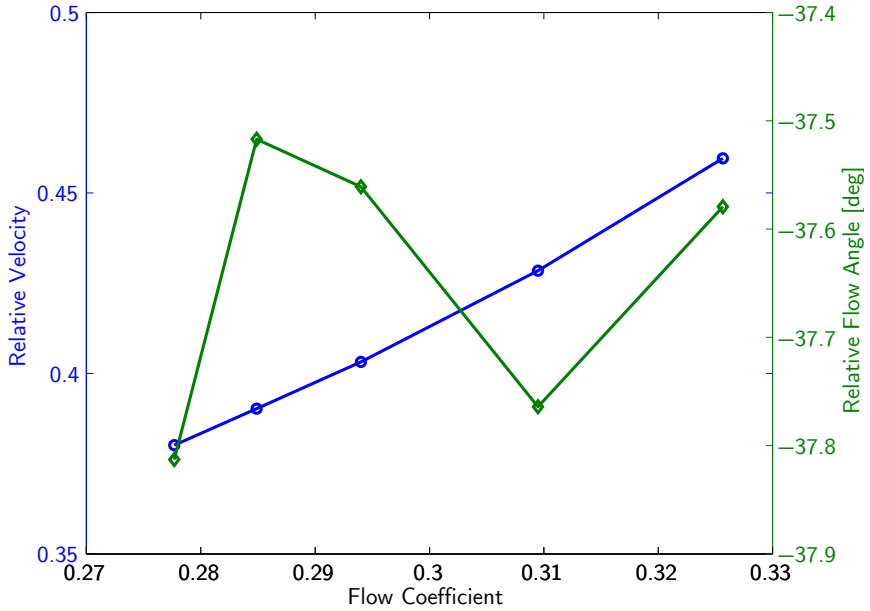

Figure 7-10: Range for w and β as function of ϕ for a point near the splitter leading edge at midspan.

While the range in normalized w is from 0.38 to 0.45, the range in β is less than 0.5 degrees. An example of the fitting procedure is shown in Fig. 7-11. The dashed blue line is the reconstructed D based on the polynomial fit.

The blade metal blockage was addressed by performing the $D(w)$ fits using w data extracted from single passage calculations and modifying the w used in the source term implementation to account for blade metal blockage using Eq. 7.3. However, implementation of the polynomial fits for $D(w)$ also yielded simulations that diverged. Investigation of the iterations prior to divergence suggested an instability based on the gradient of $f_{\mathrm{n,turn}}$ with respect to the local flow field.

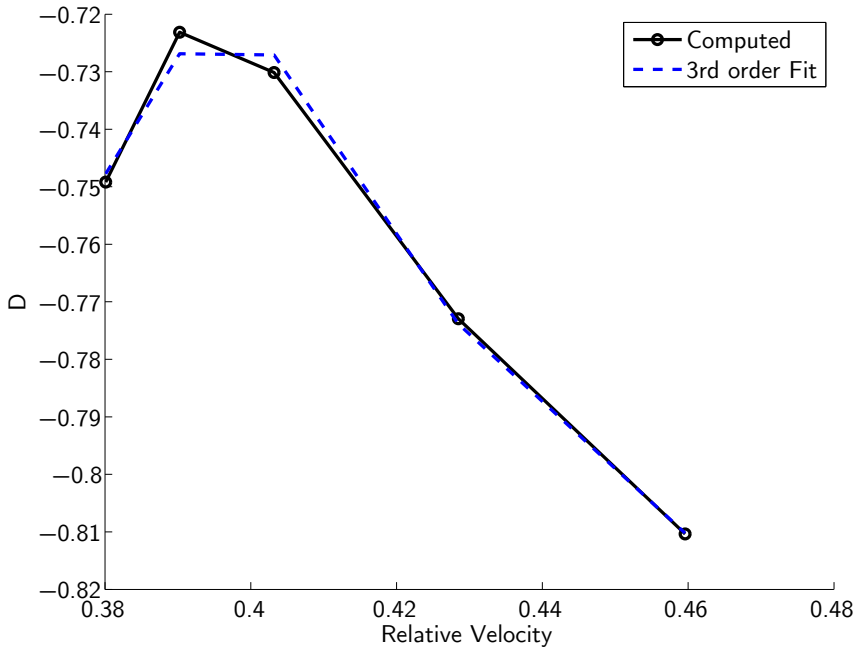

Figure 7-11: Polynomial fit accuracy for $D(w)$ for point near splitter leading edge at midspan.

7.5 Investigation of Normal Force Field Gradient

During the analysis relating D to w, it was noticed that some locations had a slope of $D(w)$ opposite to that of most other locations in the compressor. This suggested a possible instability that had not been addressed. Considering that the static stability, physical or numerical, is associated with the slope of the system output with respect to the system input, the numerical stability of the overall model was investigated by linearizing the normal force model.

Rather than compute the analytical derivatives of Eq. 3.15, a numerical linearization of the normal force model was conducted for each point within the compressor. This linearization was performed by varying w_m and w_θ and recomputing $f_{\text{n,turn}}$ based on Eq. 3.15. An example linearization around a point near the splitter leading edge at midspan is shown in Figs. 7-12 and 7-13 where the dashed blue lines are the numerical linearization of the normal force based on Eq. 3.15 for constant w_θ and w_m, respectively, and the solid black line are the normal force data extracted from the single passage Euler speedline.

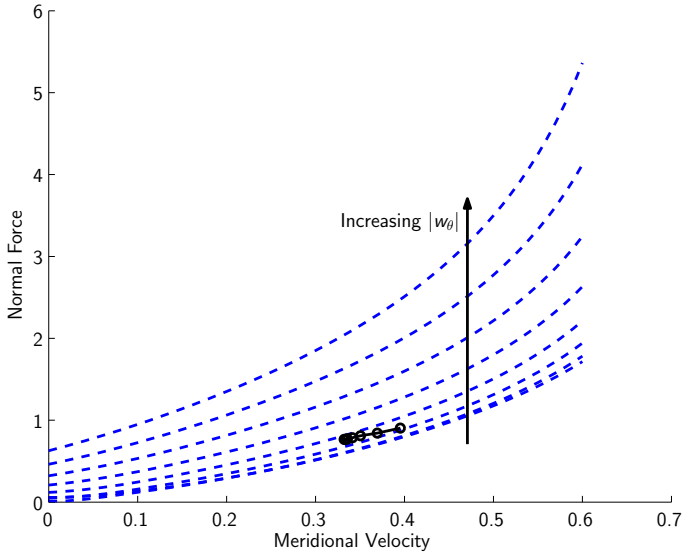

Figure 7-12: Linearization of the normal force near the splitter midspan leading edge as a function of meridional velocity. The dashed blue lines are lines of constant relative tangential velocity and the solid black line are data extracted along the speedline.

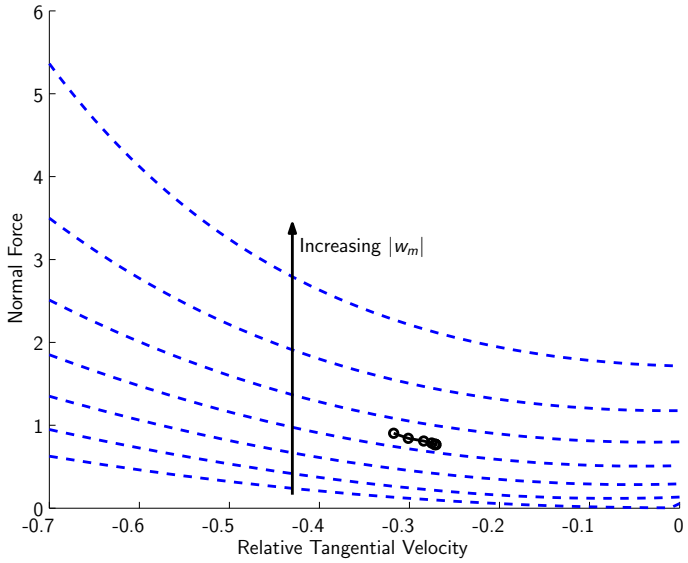

Figure 7-13: Linearization of the normal force near the splitter midspan leading edge as a function of relative tangential velocity. The dashed blue lines are lines of constant meridional velocity and the solid black line are data extracted along the speedline.

The linearization shown can be considered stable using a similar analysis as presented in Sec. 3.2.1. Overall, $f_{\text{n,turn}}$ diffuses the relative flow, i.e., if $f_{\text{n,turn}}$ increases, both $|w_m|$ and $|w_\theta|$ decrease. Inspection of Figs. 7-14 and 7-15 show that an increase in the magnitude of either w_m or w_θ yields an increase in $f_{\text{n,turn}}$, which decreases the magnitudes of w_m and w_θ, leading to numerical stability.

However, there are locations within the compressor where the above relation does not hold. One example is shown in Figs. 7-14 and 7-15 which shows the linearization around a point near the shroud at the trailing of the impeller.

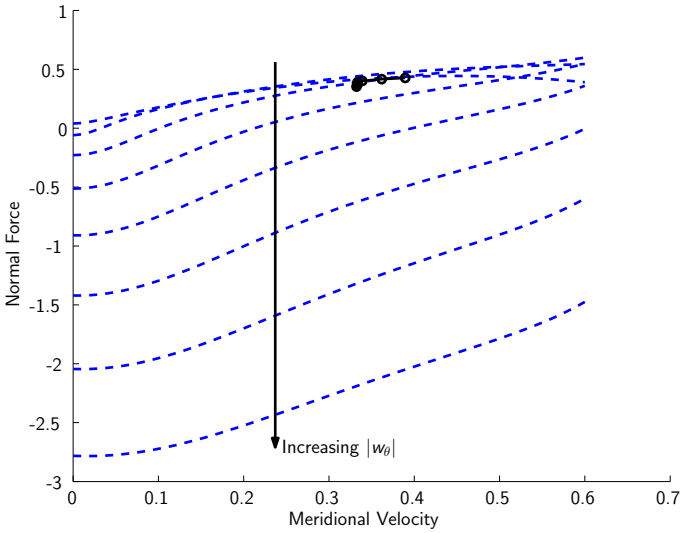

Figure 7-14: Linearization of the normal force near the splitter trailing edge shroud as a function of meridional velocity. The dashed blue lines are isolines of relative tangential velocity and the solid black line are data extracted along the speedline.

This linearization[2] shows an unstable point because an increase in the magnitude of w_θ leads to a decrease in $f_{\text{n,turn}}$ which results in less flow diffusion and an increase in $|w_\theta|$. Based on this observation, it is hypothesized that the current implementation does not fully address the numerical stability of the pitchwise averaged flow field due to a coding error. A proposed numerical flow field sensitivity metric was proposed based on this hypothesis and is presented in Tab. 7.3.

The label of "sensitive" versus "insensitive" is used to differentiate between points

[2]Since w_θ is defined as negative (against the direction of rotation), $\frac{\partial f_{\text{n,turn}}}{\partial |w_\theta|} > 0 \rightarrow \frac{\partial f_{\text{n,turn}}}{\partial w_\theta} < 0$.

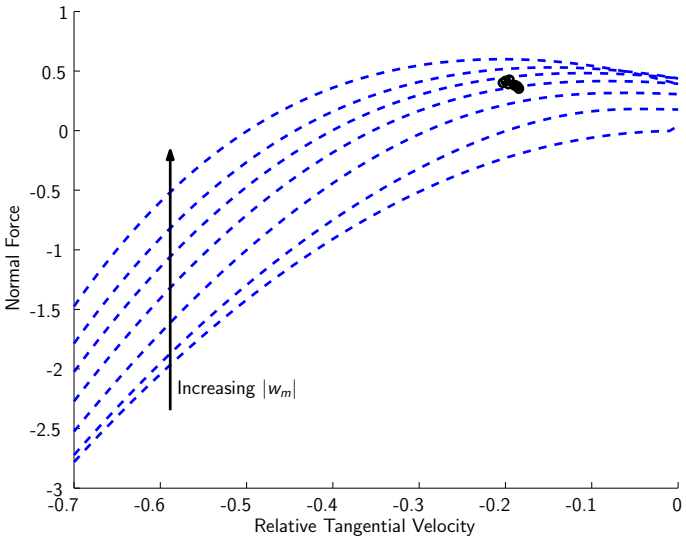

Figure 7-15: Linearization of the normal force near the splitter trailing edge shroud as a function of relative tangential velocity. The dashed blue lines are isolines of meridional velocity and the solid black line are data extracted along the speedline.

Table 7.3: Proposed numerical sensitivity based on $\nabla f_{\text{n,turn}}(w_m, w_\theta)$

$\frac{\partial f_{\text{n,turn}}}{\partial w_m}$	$\frac{\partial f_{\text{n,turn}}}{\partial w_\theta}$	Sensitive/Insensitive?
> 0	> 0	Sensitive
> 0	< 0	Insensitive
< 0	> 0	Sensitive
< 0	< 0	Insensitive

that would be sensitive to a flow field perturbation and may be numerically unstable and those points that are not sensitive to flow field perturbations and might be numerically stable. The map in Fig. 7-16 is generated using the metric in Tab. 7.3 and indicates locations based on the slopes of $\frac{\partial f_{\mathrm{n,turn}}}{\partial w_m}$ and $\frac{\partial f_{\mathrm{n,turn}}}{\partial w_\theta}$ and Figs. 7-17 and 7-18 show the value of $\frac{\partial f_{\mathrm{n,turn}}}{\partial w_m}$ and $\frac{\partial f_{\mathrm{n,turn}}}{\partial w_\theta}$ respectively.

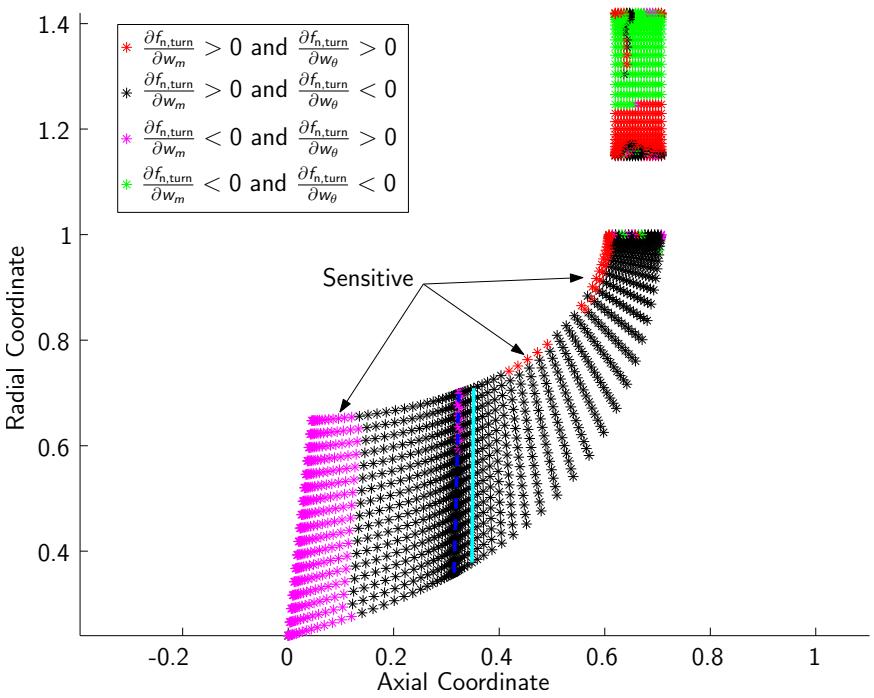

Figure 7-16: Map of sensitive and insensitive points based on $\nabla f_{\mathrm{n,turn}}(w_m, w_\theta)$.

The sign of the slopes are taken around the values of a operating point near peak efficiency. The map suggests the region near the shroud downstream of the splitter leading edge is highly sensitive to numerical instabilities. Even though there is a region of sensitive points at the inducer leading edge, the meridional extent of the sensitive region compared to the insensitive region suggests that the inducer, as a whole, is insensitive. This was confirmed by performing inducer only simulations using the normal force model, which converged to appropriate flow quantities. Evidence suggesting that the gradient of $f_{\mathrm{n,turn}}$ with respect to w_m and w_θ governs the stability of the implementation is presented in the next section.

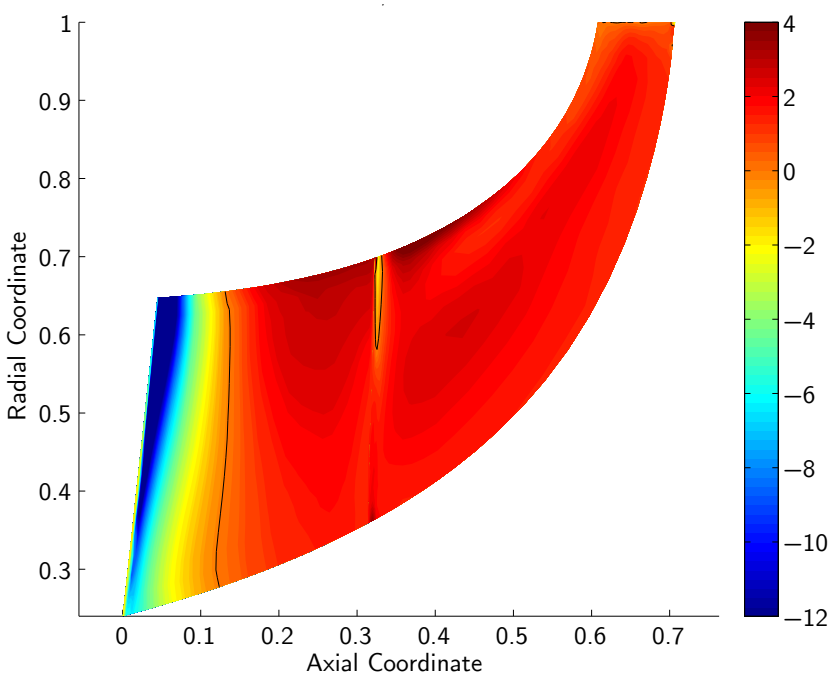

Figure 7-17: Contour plot of $\frac{\partial f_{\text{n,turn}}}{\partial w_m}$. The black isoline is $\frac{\partial f_{\text{n,turn}}}{\partial w_m} = 0$.

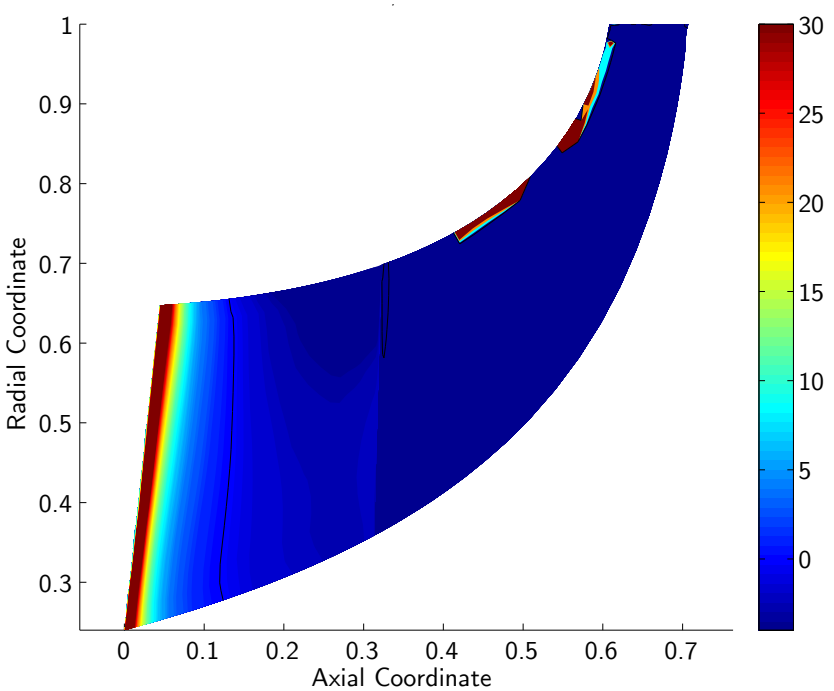

Figure 7-18: Contour plot of $\frac{\partial f_{\text{n,turn}}}{\partial w_\theta}$. The black isoline is $\frac{\partial f_{\text{n,turn}}}{\partial w_\theta} = 0$.

7.6 Instability Caused by Low Meridional Velocity

Examination of the body force model simulation flow field while the solver was iterating suggests a mechanism through which the calculation is numerically unstable, consistent with the proposed $\nabla f_{\mathrm{n,turn}}(w_m, w_\theta)$ metric. This simulation also used the normal force model with a scaling on $f_{\mathrm{n,turn}}$ and a correction to $\widetilde{w_m} = \frac{w_m}{b}$ to account for the lack of blade metal blockage in FINE/Turbo.

The hypothesized mechanism for the numerical instability begins with a small region near the shroud of over predicted normal force. The higher $f_{\mathrm{n,turn}}$ diffuses the relative velocity more so than in the single passage simulation. The meridional velocity drops and a region of low w_m appears. This low w_m flow region convects with the mean flow along the shroud towards the impeller trailing edge. Upstream of the low w_m region, $f_{\mathrm{n,turn}}$ decreases in response to the drop in w_m which in turn causes w_m to increase, balancing the low w_m region. The low w_m region reaches the impeller trailing edge by which point it has grown in magnitude, i.e. the w_m deficit is large compared to the w_m value extracted from a single passage simulation for that location and operating condition. The described mechanism is illustrated in Figs. 7-19(a) to 7-19(e) as contour plots of the relative error in w_m.

The region of low w_m is seen convecting with the background flow towards the trailing edge. As it convects downstream, the low w_m region creates aerodynamic blockage, causing flow closer to midspan and the hub to accelerate. When the low w_m region reaches the trailing edge it has become a reverse flow region that causes the simulation to diverge.

Further investigation showed that when the low w_m region arrives at the trailing edge, the $D(w)$ distribution is positively sloped with respect to w and has a negative value. The negative value of D at the trailing edge is indicative of slip since $D = r_2 \frac{\partial \delta}{\partial \ell} < 0$ implies that β tends away from direction of rotation. An example of the $D(w)$ function for a point at the trailing edge midspan is shown in Fig. 7-20.

In summary, the current implementation does not appear to capture the inherent numerical stability of the pitchwise averaged flow field. This suggests that one of the

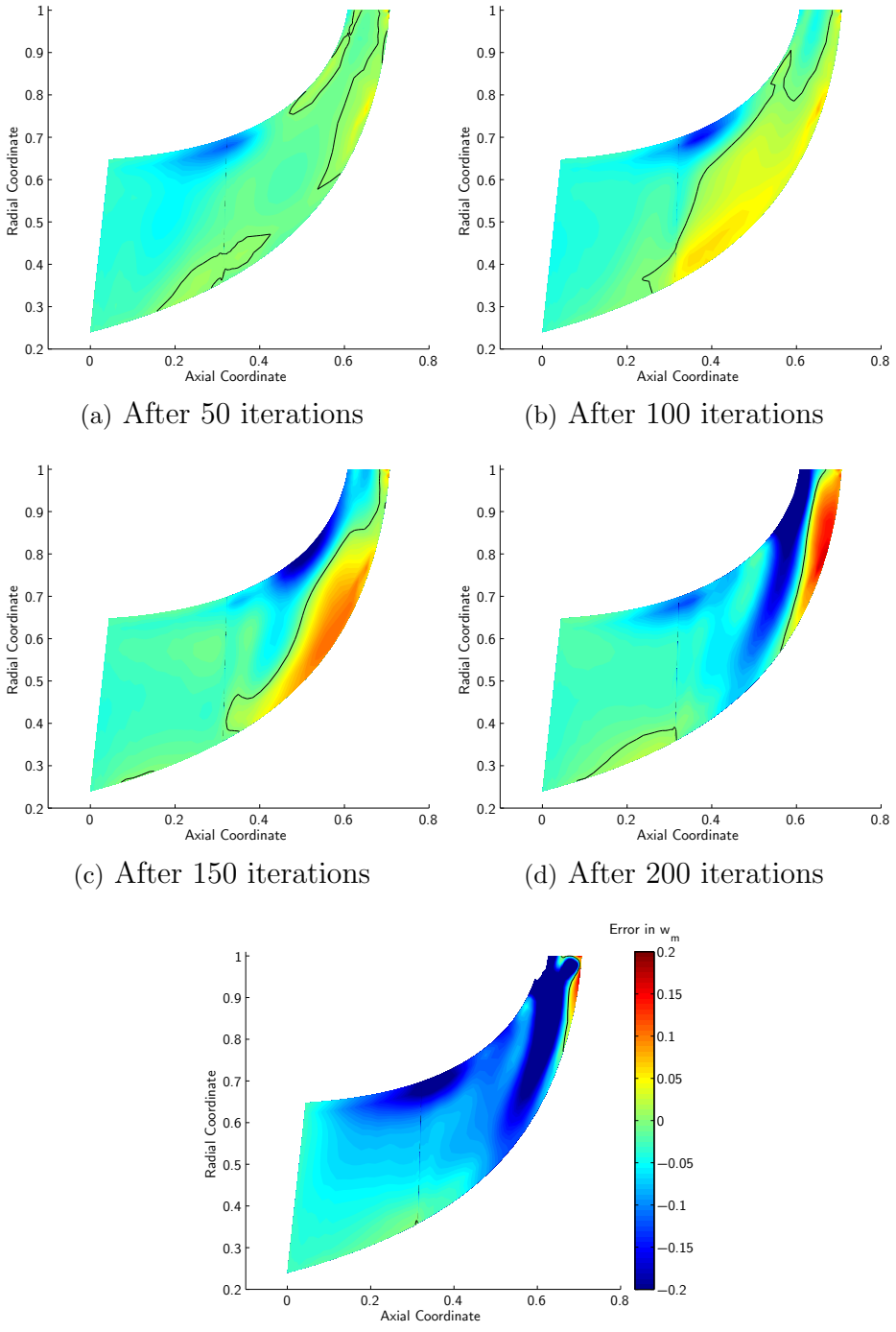

(a) After 50 iterations

(b) After 100 iterations

(c) After 150 iterations

(d) After 200 iterations

(e) After 240 iterations

Figure 7-19: Relative error in w_m at various iterations through simulation. All contours use the scale in Fig. 7-19(e). Black lines are isolines of Error = 0.

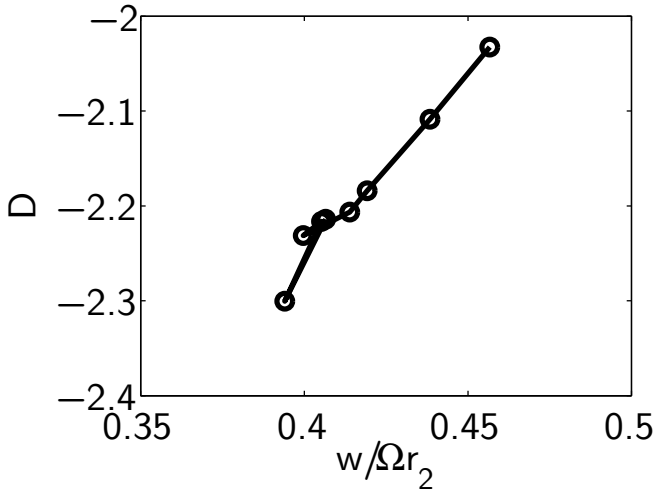

Figure 7-20: .

inputs to the blade passage model might not be calculated correctly.

7.7 Summary of Diagnostics

Time constraints prevented further diagnostics and a summary of what was learned is described here.

- The gradient of $f_{\text{n,turn}}$ with respect to $\mathbf{w}$ may govern numerical stability of the model implementation. The sign of the slope of the normal force is consistent with the illustration of the convection of low w_m region to the impeller trailing edge.

- Numerical divergence occurs due to a low w_m region that convects with the mean flow and causes reverse flow once it reaches the trailing edge. It is hypothesized that the trailing edge slip affects the numerical stability of a low w_m region at the trailing edge. This is related to the lack of stiffness of the "rubber blade passage." Further investigation is required.

Figure 7-21 illustrates the overall body force model implementation. The green check marks indicate the processes that have been validated. The processes upstream of

computing the deviation gradient parameter have been validated through the body force simulation with a prescribed body force field, discussed in Chaps. 4 and 5. The fitting procedure for $D(w)$ and writing the coefficients to file have been validated by reconstruction of D based on the flow field extracted from the single passage Euler simulation. The diagnostics discussed above support the hypothesis that the error is in the computation of D since the current implementation does not capture the static behavior of the flow field.

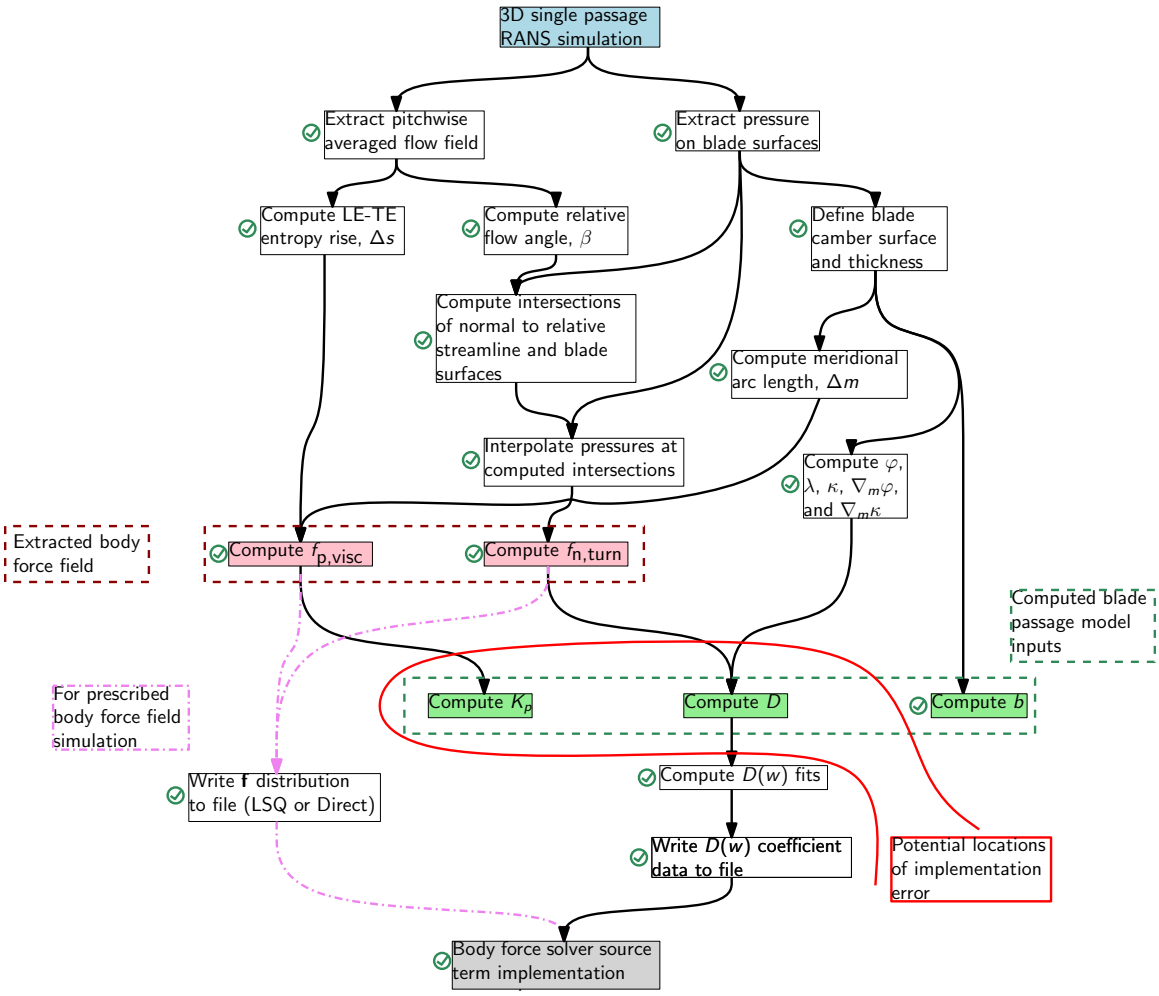

Figure 7-21: Implementation of body force model. Processes with a green check mark have been verified. Implementation error most likely lies within red boundary.

Chapter 8

Summary and Conclusions

Previous work has shown that body force-based methods can capture the response to inlet flow distortions in axial compressors and the onset of instability in both axial and centrifugal compressors, though not in a predictive manner. A blade passage model applicable to centrifugal compressors that addresses the limitations of previous body force-based methods has been derived and validated on a radial impeller with prismatic blades. Numerical convergence problems were encountered when applying the model to compressors with three dimensional blade geometries. Comparison of the present model to other blade passage models for axial compressors indicates the derivation is sound and that there is an error in the implementation. A set of diagnostics has been performed and the possible location of the error has been identified.

8.1 Concluding Remarks

The focus of this work has been the definition and implementation of a new blade passage model that addresses the limitations of previous models and is applicable for centrifugal compressors.

The new blade passage model is comprised of three components that bookkeep the effects of the blade loading, the viscous dissipation in the blade passage, and the blade metal blockage. The inputs for these models were derived from single passage RANS simulations by examination of the forces on each discrete blade rather than a

control volume analysis of the blade passage.

A radial impeller with radial blades was used to validate the blade passage model. The overall compressor performance was found to be within 6.75% in total-to-static pressure rise coefficient and 5% in stage loading coefficient. The reconstructed axisymmetric flow field was found to be within 4% of the pitchwise averaged single passage RANS flow field.

Application of blade passage model to three-dimensional applications uncovered numerical instabilities that have yet to be solved. Some of the diagnostics performed have been discussed and possible avenues for addressing the numerical instability are presented.

8.2 Future Work

The following recommendations are made based on the findings in the current work

1. Unsteady stall inception simulations should be carried out on the radial impeller to demonstrate the modeling of stall inception.

2. The implementation error should be addressed by using a known axial compressor rotor test case where other blade passage models have been successfully demonstrated. It is suggested that the validation of the computation of D be the first step.

3. Differences in the axisymmetric flow field of the radial impeller were found to be due to a lack of modeling of upstream influence and aerodynamic blockage. The following ideas are presented as stepping stones to address these issues:

    - Upstream influence can be modeled by a discrete, non-axisymmetric source term that rotates around the annulus at the same rotation rate as the blade row. An analytical expression for the form of the source term should be derived that does not rely on empiricism, experiments, or trial and error.
    - The aerodynamic blockage due to boundary layer displacement should be modeled. Looking to 3D external flow for guidance, the viscous boundary

layer can be modeled using mass source terms, similar to the blade metal blockage model. However, the external flow case also has a sink of the same strength as the source term downstream of the blade to ensure continuity is not violated. A method of modeling the amount of aerodynamic blockage due to the boundary layer and modeling the blockage without violating continuity should be established.

Appendix A

Definition of Relative Streamline Coordinate System

In order to examine the forces along the relative streamline, the coordinate system needs to be defined in relation to the cylindrical coordinate system. In order to be consistent with the assumption of negligible spanwise flow, the meridional flow path angle, φ, and the blade lean angle, λ, are used to define an axisymmetric stream surface in which the two-dimensional relative streamline blade passage model is developed.

- (r, θ, x): Cylindrical coordinate system where r is the radial direction, θ is the circumferential direction (positive in direction of rotation), and x is the axial direction. Shown in Figure A-1.

- (s, θ, m): Coordinate system aligned with local mean radius flow path. The (s, θ, m)-coordinate system is the (r, θ, x)-coordinate system rotated by angle φ around the θ-axis. m is the meridional direction, θ is the circumferential direction, and s is normal to the $m - \theta$ plane in the spanwise direction both shown in Figs. A-1 and A-2(a).

- (k, h, m): The (k, h, m)-coordinate system is the (s, θ, m)-coordinate system rotated by angle λ around the m-axis where λ is the lean angle of the blade at

that location. h is the direction normal to the blade in the θ direction and k is the direction parallel to the blade surface in the s direction. The $\lambda = 0$ case occurs when the blades are strictly radial.

- (k, n, ℓ): Local flow coordinate system aligned with local flow velocity vector. The (k, n, ℓ)-coordinate system is the (k, h, m)-coordinate system rotated by angle β around the s-axis where β is the angle between the in-$(h - m)$-plane velocity vector and the local meridional direction in the plane normal to the blade lean. ℓ is the direction aligned with the local flow velocity vector (parallel), n is direction normal to the local flow velocity in the $h-m$ plane, and k is normal to both the $h - m$ plane and the $\ell - n$ plane in the spanwise direction. Shown in Figure A-2(b).

Transformation matrices are employed using φ, λ, and β to switch between the cylindrical and relative flow coordinate systems.

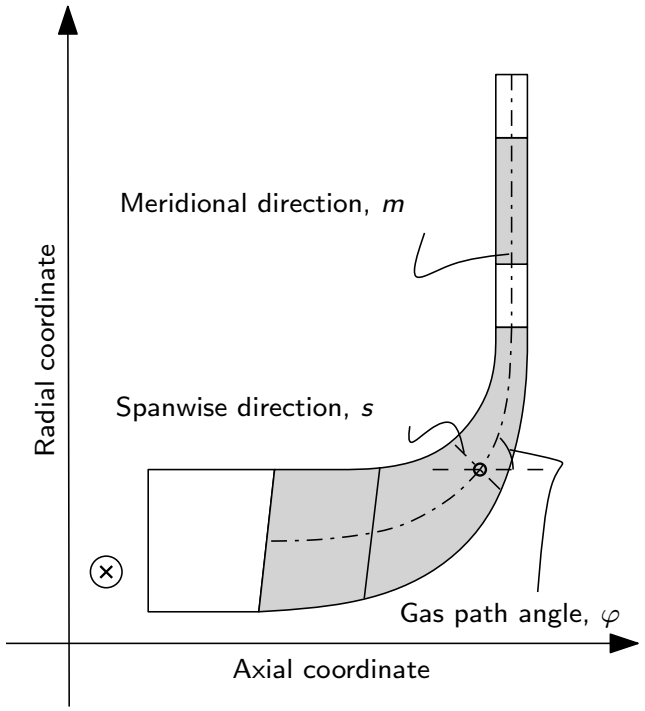

Figure A-1: Meridional coordinate system definition.

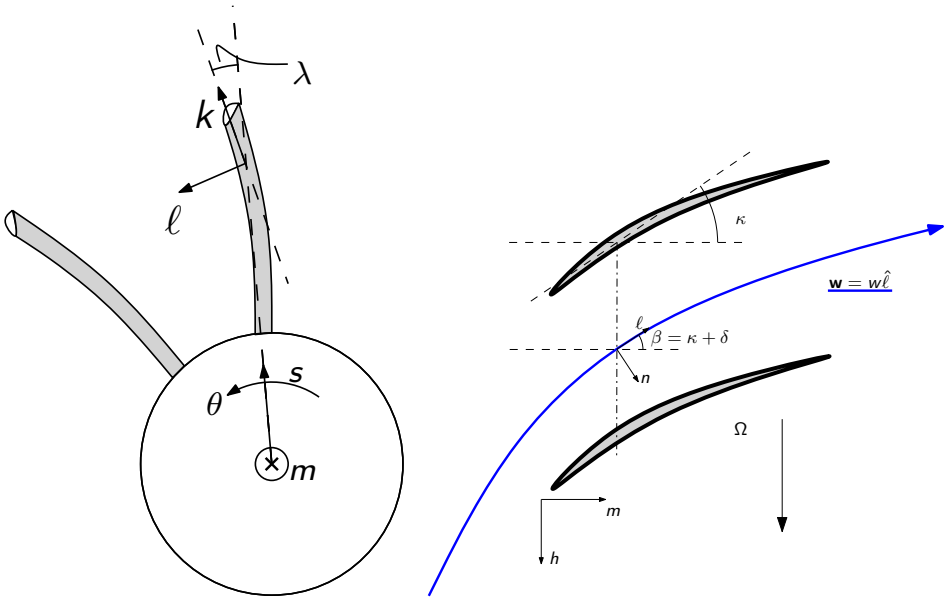

(a) Blade lean coordinate system (b) Blade stagger coordinate system

Figure A-2: Blade lean and blade stagger coordinate systems.

Appendix B

Influence Coefficient Analysis for Static Pressure Changes

The influence coefficients for static pressure changes in compressible flow in the rotating frame with body forces normal and parallel to the relative streamline are derived.

B.1 Governing Equations

The non-dimensionalized change in quantities in the governing equations are given for the two-dimensional meridional fluid element shown.

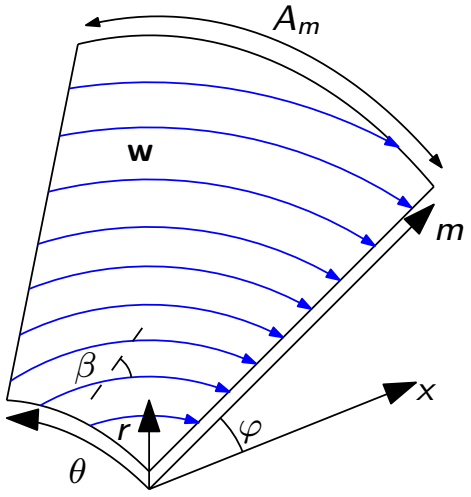

Figure B-1: Fluid element used for influence coefficient analysis.

There are six unknowns, $\frac{dp}{p}$, $\frac{d\rho}{\rho}$, $\frac{du_m}{u_m}$, $\frac{dw_\theta}{w_\theta}$, $\frac{dT}{T}$, and $\frac{dA_m}{A_m}$, and six equations, given below,

Equation of State.

$$\frac{dp}{p}\left[1\right] = \frac{d\rho}{\rho}\left[1\right] + \frac{dT}{T}\left[1\right] \tag{B.1}$$

Definition of Relative Velocity.

$$\frac{dw}{w}\left[1\right] = \frac{du_m}{u_m}\left[\cos^2\beta\right] + \frac{dw_\theta}{w_\theta}\left[\sin^2\beta\right] \tag{B.2}$$

Meridional Area. Since the body force model assumes a curved two dimensional stream surface, the change in area of the fluid element is proportional to the change in radius via,

$$\frac{dA_m}{A_m} = \frac{dr}{r} \tag{B.3}$$

Continuity.

$$\frac{du_m}{u_m}\left[1\right] = \frac{dr}{r}\left[-1\right] + \frac{d\rho}{\rho}\left[-1\right] \tag{B.4}$$

Meridional Momentum.

$$\frac{dp}{p}\left[1\right] = \frac{\rho f_{\mathrm{n,turn}} dm}{p}\left[-\sin\beta\right] + \frac{\rho f_{\mathrm{p,visc}} dm}{p}\left[\cos\beta\right] + \frac{dr}{r}\left[\gamma\left(M_{rel,\theta} + M_\Omega\right)^2\right] + \frac{du_m}{u_m}\left[-\gamma M_m^2\right] \tag{B.5}$$

Angular Momentum.

$$\frac{dw_\theta}{w_\theta}\left[1\right] = \frac{\rho f_{\mathrm{n,turn}} dm}{p}\left[\frac{1}{\gamma M_{rel}^2 \sin\beta}\right] + \frac{f_{\mathrm{p,visc}} dm}{p}\left[\frac{1}{\gamma M_{rel}^2 \cos\beta}\right] + \frac{dr}{r}\left[-1 - 2\frac{M_\Omega}{M_{rel,\theta}}\right] \tag{B.6}$$

Energy/Conservation of Rothalpy.

$$\frac{dT}{T}\left[1\right] = \frac{dr}{r}\left[\left(\gamma-1\right)M_{\Omega}^{2}\right] + \frac{dw}{w}\left[-\left(\gamma-1\right)M_{rel}^{2}\right] \tag{B.7}$$

B.2 Influence Coefficients for Static Pressure Changes

First, Eq. B.4 is substituted into Eq. B.5,

$$\begin{aligned}\frac{dp}{p} &= \frac{\rho f_{\mathrm{n,turn}} dm}{p}\left[-\sin\beta\right] + \frac{\rho f_{\mathrm{p,visc}} dm}{p}\left[\cos\beta\right] + \frac{dr}{r}\left[\gamma\left(M_{rel,\theta}+M_{\Omega}\right)^{2}\right] \\ &\quad + \left(\frac{dr}{r}\left[-1\right] + \frac{d\rho}{\rho}\left[-1\right]\right)\left[-\gamma M_{m}^{2}\right] \qquad \text{(B.8)} \\ \frac{dp}{p} &= \frac{\rho f_{\mathrm{n,turn}} dm}{p}\left[-\sin\beta\right] + \frac{\rho f_{\mathrm{p,visc}} dm}{p}\left[\cos\beta\right] + \frac{dr}{r}\left[\gamma M^{2}\right] + \frac{d\rho}{\rho}\left[\gamma M_{m}^{2}\right] \ . \qquad \text{(B.9)}\end{aligned}$$

Then, Eq. B.1 is substituted in,

$$\frac{dp}{p} = \frac{\rho f_{\mathrm{n,turn}} dm}{p}\left[-\sin\beta\right] + \frac{\rho f_{\mathrm{p,visc}} dm}{p}\left[\cos\beta\right] + \frac{dr}{r}\left[\gamma M^{2}\right] + \left(\frac{dp}{p}\left[1\right] + \frac{dT}{T}\left[-1\right]\right)\left[\gamma M_{m}^{2}\right] \tag{B.10}$$

$$\frac{dp}{p}\left[1-\gamma M_{m}^{2}\right] = \frac{\rho f_{\mathrm{n,turn}} dm}{p}\left[-\sin\beta\right] + \frac{\rho f_{\mathrm{p,visc}} dm}{p}\left[\cos\beta\right] + \frac{dr}{r}\left[\gamma M^{2}\right] + \frac{dT}{T}\left[-\gamma M_{m}^{2}\right] \ . \tag{B.11}$$

Next, Eq. B.7 is introduced,

$$\begin{aligned}\frac{dp}{p}\left[1-\gamma M_{m}^{2}\right] &= \frac{\rho f_{\mathrm{n,turn}} dm}{p}\left[-\sin\beta\right] + \frac{\rho f_{\mathrm{p,visc}} dm}{p}\left[\cos\beta\right] + \frac{dr}{r}\left[\gamma M^{2}\right] \\ &\quad + \left(\frac{dw}{w}\left[-\left(\gamma-1\right)M_{rel}^{2}\right] + \frac{dr}{r}\left[\left(\gamma-1\right)M_{\Omega}^{2}\right]\right)\left[-\gamma M_{m}^{2}\right] \qquad \text{(B.12)} \\ \frac{dp}{p}\left[1-\gamma M_{m}^{2}\right] &= \frac{\rho f_{\mathrm{n,turn}} dm}{p}\left[-\sin\beta\right] + \frac{\rho f_{\mathrm{p,visc}} dm}{p}\left[\cos\beta\right] \\ &\quad + \frac{dr}{r}\left[\gamma M^{2} - \gamma M_{m}^{2}\left(\gamma-1\right)M_{\Omega}^{2}\right] + \frac{dw}{w}\left[\gamma M_{m}^{2}\left(\gamma-1\right)M_{rel}^{2}\right] \ . \qquad \text{(B.13)}\end{aligned}$$

Then, Eq. B.2 is substituted,

$$\begin{aligned}\frac{dp}{p}\left[1-\gamma M_m^2\right] &= \frac{\rho f_{\mathrm{n,turn}} dm}{p}\left[-\sin\beta\right] + \frac{\rho f_{\mathrm{p,visc}} dm}{p}\left[\cos\beta\right] \\ &+ \frac{dr}{r}\left[\gamma M^2 - \gamma M_m^2\left(\gamma-1\right) M_\Omega^2\right] \\ &+ \left(\frac{du_m}{u_m}\left[\cos^2\beta\right] + \frac{dw_\theta}{w_\theta}\left[\sin^2\beta\right]\right)\left[\gamma M_m^2\left(\gamma-1\right) M_{rel}^2\right] \qquad \text{(B.14)} \\ \frac{dp}{p}\left[1-\gamma M_m^2\right] &= \frac{\rho f_{\mathrm{n,turn}} dm}{p}\left[-\sin\beta\right] + \frac{\rho f_{\mathrm{p,visc}} dm}{p}\left[\cos\beta\right] \\ &+ \frac{dr}{r}\left[\gamma M^2 - \gamma M_m^2\left(\gamma-1\right) M_\Omega^2\right] \\ &+ \frac{du_m}{u_m}\left[\gamma M_m^2\left(\gamma-1\right) M_m^2\right] + \frac{dw_\theta}{w_\theta}\left[\gamma M_m^2\left(\gamma-1\right) M_{rel,\theta}^2\right] \ . \qquad \text{(B.15)}\end{aligned}$$

Equation B.5 is used again to obtain,

$$\begin{aligned}\frac{dp}{p}\left[1-\gamma M_m^2\right] &= \frac{\rho f_{\mathrm{n,turn}} dm}{p}\left[-\sin\beta\right] + \frac{\rho f_{\mathrm{p,visc}} dm}{p}\left[\cos\beta\right] \\ &+ \frac{dr}{r}\left[\gamma M^2 - \gamma M_m^2\left(\gamma-1\right) M_\Omega^2\right] + \frac{dw_\theta}{w_\theta}\left[\gamma M_m^2\left(\gamma-1\right) M_{rel,\theta}^2\right] \\ &+ \left(\frac{\rho f_{\mathrm{n,turn}} dm}{p}\left[-\sin\beta\right] + \frac{\rho f_{\mathrm{p,visc}} dm}{p}\left[\cos\beta\right] + \frac{dr}{r}\left[\gamma\left(M_{rel,\theta}+M_\Omega\right)^2\right] + \frac{dp}{p}\left[-1\right]\right)\left[\left(\gamma-1\right) M_m^2\right] \qquad \text{(B.16)} \\ \frac{dp}{p}\left[1-M_m^2\right] &= \frac{\rho f_{\mathrm{n,turn}} dm}{p}\left[-\sin\beta\left(1+\left(\gamma-1\right) M_m^2\right)\right] + \frac{\rho f_{\mathrm{p,visc}} dm}{p}\left[\cos\beta\left(1+\left(\gamma-1\right) M_m^2\right)\right] \\ &+ \frac{dr}{r}\left[\gamma M^2 - \gamma M_m^2\left(\gamma-1\right) M_\Omega^2 + \gamma\left(M_{rel,\theta}+M_\Omega\right)^2\left(\gamma-1\right) M_m^2\right] + \frac{dw_\theta}{w_\theta}\left[\gamma M_m^2\left(\gamma-1\right) M_{rel,\theta}^2\right] \ . \qquad \text{(B.17)}\end{aligned}$$

Finally, Eq. B.6 is introduced,

$$\begin{aligned}\frac{dp}{p}\left[1-M_m^2\right] &= \frac{\rho f_{\mathrm{n,turn}} dm}{p}\left[-\sin\beta\left(1+\left(\gamma-1\right) M_m^2\right)\right] + \frac{\rho f_{\mathrm{p,visc}} dm}{p}\left[\cos\beta\left(1+\left(\gamma-1\right) M_m^2\right)\right] \\ &+ \frac{dr}{r}\left[\gamma M^2 - \gamma M_m^2\left(\gamma-1\right) M_\Omega^2 + \gamma\left(M_{rel,\theta}+M_\Omega\right)^2\left(\gamma-1\right) M_m^2\right] \\ &+ \left\{\left(\frac{\rho f_{\mathrm{n,turn}} dm}{p}\left[\frac{1}{\gamma M_{rel}^2\sin\beta}\right] + \frac{f_{\mathrm{p,visc}} dm}{p}\left[\frac{1}{\gamma M_{rel}^2\cos\beta}\right] + \frac{dr}{r}\left[-1-2\frac{M_\Omega}{M_{rel,\theta}}\right]\right)\right. \\ &\left.\times\left[\gamma M_m^2\left(\gamma-1\right) M_{rel,\theta}^2\right]\right\} \ . \qquad \text{(B.18)}\end{aligned}$$

Simplifying the above result yields,

$$\frac{dp}{p} = \frac{\rho f_{\mathrm{n,turn}} dm}{p}\left[-\frac{\sin\beta\left(1+\sin^2\lambda\left(\gamma-1\right)M_m^2\right)}{1-M_m^2}\right] + \frac{\rho f_{\mathrm{p,visc}} dm}{p}\left[\frac{\cos\beta\left(1+\left(\gamma-1\right)M_{rel}^2\left(1-\sin^2\lambda\sin^2\beta\right)\right)}{1-M_m^2}\right] + \frac{dr}{r}\left[\frac{\gamma M^2}{1-M_m^2}\right] \ . \tag{B.19}$$

Expressions for meridional and normal-to-blade pressure gradients are obtained by dividing through by dm and dh respectively, where $\frac{dr}{dm} = \sin\varphi$ and $\frac{dr}{dh} = -\sin\lambda\cos\varphi$,

$$\frac{1}{\rho}\frac{\partial p}{\partial m} = f_{\mathrm{n,turn}}\left[-\frac{\sin\beta\left(1+\sin^2\lambda\left(\gamma-1\right)M_m^2\right)}{1-M_m^2}\right] + f_{\mathrm{p,visc}}\left[\frac{\cos\beta\left(1+\left(\gamma-1\right)M_{rel}^2\left(1-\sin^2\lambda\sin^2\beta\right)\right)}{1-M_m^2}\right] + \frac{u^2}{r}\left[\frac{\sin\varphi}{1-M_m^2}\right] \tag{B.20}$$

$$\frac{1}{\rho}\frac{\partial p}{\partial h} = \frac{u^2}{r}\left[\frac{-\sin\lambda\cos\varphi}{1-M_m^2}\right] \ . \tag{B.21}$$

Bibliography

[1] B. Benneke. A Methodology for Centrifugal Compressor Stability Prediction. Masters thesis, Massachusetts Institute of Technology, September 2009.

[2] M. L. Brand. An improved blade passage model for estimating off-design axial compressor performance. Masters thesis, Massachusetts Institute of Technology, 2013.

[3] M. L. Brand and A. P. Kottapalli. The Dependence of Spike-Type Stall Inception on Blade-Tip Leakage Flow in Axial Compressors. Technical report, Massachusetts Institute of Technology, Cambridge, MA, 2011.

[4] T. R. Camp and I. J. Day. A Study of Spike and Modal Stall Phenomena in a Low- Speed Axial Compressor. Journal of Turbomachinery, 120(Jul.):393–401, 1998.

[5] R. V. Chima. A Three-Dimensional Unsteady CFD Model of Compressor Stability. In ASME Turbo Expo 2006, Power for Land, Sea, and Air, pages 1–12, Barcelona, Spain, 2006. ASME.

[6] N. A. Cumpsty. Compressor Aerodynamics. Krieger Publishing Company, 2004.

[7] J. J. Defoe. Inlet Swirl Distortion Effects on the Generation and Propagation of Fan Rotor Shock Noise. Doctoral thesis, Massachusetts Institute of Technology, September 2011.

[8] J. J. Defoe and Z. S. Spakovszky. Shock Propagation and MPT Noise From a Transonic Rotor in Nonuniform Flow. Journal of Turbomachinery, 135(1):011016, October 2013.

[9] J. D. Denton. Some Limitations of Turbomachinery CFD. In Proceedings of ASME Turbo Expo 2010: Power for Land, Sea and Air, June 2010.

[10] M. Drela. 16.110 flight vehicle aerodynamics class notes. Massachusetts Institute of Technology Unified Engineering Lecture Notes, 2010.

[11] M. Drela. A Users Guide to MTFLOW 2.01. Technical report, Massachusetts Institute of Technology, Cambridge, MA, 2010.

[12] H. W. Emmons, C. E. Pearson, and H. P. Grant. Compressor Surge and Stall Propogation. Transactions of the ASME, May:455–469, 1955.

[13] J. N. Everitt and Z. S. Spakovszky. An Investigation of Stall Inception in Centrifugal Compressor Vaned Diffusers. Journal of Turbomachinery, 135(1), Jan. 2013.

[14] Y. Gong. A Computational Model for Rotating Stall and Inlet Distortions in Multistage Compressors. Doctoral thesis, Massachusetts Institute of Technology, Feb. 1999.

[15] E. M. Greitzer. Surge and rotating stall in axial flow compressors part i: Theoretical compression system model. Journal of Engineering for Power, 98(April):190–198, 1976.

[16] E. M. Greitzer. Surge and rotating stall in axial flow compressors part ii: Experimental results and comparison. Journal of Engineering for Power, 98(April):199–212, 1976.

[17] E. M. Greitzer. The Stability of Pumping Systems. Journal of Fluids Engineering, 103:193–242, June 1981.

[18] E. M. Greitzer, Z. S. Spakovszky, and I. A. Waitz. 16.unified: Thermodynamics and propulsion, 2006.

[19] E. M. Greitzer, C. S. Tan, and M. B. Graf. Internal Flow: Concepts and Applications. Cambridge University Press, 2004.

[20] R. A. Hill IV. Simulation of Spike Stall Inception in a Radial Vaned Diffuser. Masters thesis, Massachusetts Institute of Technology, 2007.

[21] R. Hunziker and G. Gyarmathy. The Operational Stability of a Centrifugal Compressor and its Dependence on the Characteristics of the Subcomponents. Journal of Turbomachinery, 116(April):250–259, April 1994.

[22] J. Kerner. An Assessment of Body Force Representations for Compressor Stall Simulation. Masters thesis, Massachusetts Institute of Technology, Feb. 2010.

[23] G. Kiwada. Development of a Body Force Description for Compressor Stability Assessment. Masters thesis, Massachusetts Institute of Technology, Feb. 2008.

[24] J. P. Longley. A Review of Nonsteady Flow Models for Compressor Stability. Journal of Turbomachinery, 116:202–215, April 1994.

[25] F. E. Marble. Three-Dimensional Flow in Turbomachine. In W. R. Hawthorne, editor, Aerodynamics of Turbines and Compressors, X of High Speed Aerodynamics, pages 83–166. Princeton University Press, 1964.

[26] N. M. McDougall, N. A. Cumpsty, and T. P. Hynes. Stall Inception in Axial Compressors. Transactions of the ASME, 112(January 1990):116–123, 1990.

[27] T. Möller and B. Trumbore. Fast, Minimum Storage Ray-Triangle Intersection. Journal of Graphics Tools, 2(1):21–28, 1997.

[28] F. K. Moore and E. M. Greitzer. A Theory of Post-Stall Transients in Multistage Axial Compression Systems. Technical Report Mar., NASA Lewis Research Center, 1985.

[29] Fine/turbo user manual version 8.8.2. Technical report, Numeca Int., 2011.

[30] J. D. Paduano. Analysis of Compression System Dynamics. Technical report, Massachusetts Institute of Technology, 2001.

[31] A. Peters. Ultra-Short Nacelles for Low Fan Pressure Ratio Propulsors. Doctoral thesis, Massachusetts Institute of Technology, 2013.

[32] A. Plas. Performance of a boundary layer ingesting propulsion system. Masters thesis, Massachusetts Institute of Technology, 2006.

[33] G. Pullan, A. M. Young, I. J. Day, E. M. Greitzer, and Z. S. Spakovszky. Origins and Structure of Spike-Type Rotating Stall. In Proceedings of ASME Turbo Expo 2012, Copenhagen, Denmark, 2012.

[34] L. Reid and R. D. Moore. Design and overall performance of four highly-loaded, high speed inlet stages for an advanced high-pressure ratio core compressor. Technical report, NASA TP 1337, 1978.

[35] A. Röber. Simulation of Instability Onset in Advanced Centrifugal Compressors. Diploma thesis, Technische Universität Dresden, May 2011.

[36] D. J. L. Smith and H. Merryweather. The Use of Analytic Surfaces for the Design of Centrifugal Impellers by Computer Graphics. International Journal for Numerical Methods in Engineering, 7(April):137–154, 1973.

[37] Z. S. Spakovszky. Applications of Axial and Radial Compressor Dynamic System Modeling. Doctoral thesis, Massachusetts Institute of Technology, 2001.

[38] Z. S. Spakovszky. Backward Traveling Rotating Stall Waves in Centrifugal Compressors. Journal of Turbomachinery, 126(1):1, 2004.

[39] Z. S. Spakovszky and C. H. Roduner. Spike and Modal Stall Inception in an Advanced Turbocharger Centrifugal Compressor. Journal of Turbomachinery, 131(3):031012, 2009.

[40] A. H. Stenning. Rotating Stall and Surge. Journal of Fluids Engineering, 102(Mar.):14–20, 1980.

[41] Abb turbocharging. www.abb.com/product/us/9AAX132908.aspx, 2008.

[42] H. D. Vo, C. S. Tan, and E. M. Greitzer. Criteria for Spike Initiated Rotating Stall. Journal of Turbomachinery, 130(1):011023, 2008.